SIMULATION AND CHARACTERIZATION OF CATHODE REACTIONS IN SOLID OXIDE FUEL CELLS

A Dissertation
Presented to
The Academic Faculty

by

Robert E. Williams Jr.

In Partial Fulfillment
of the Requirements for the Degree
Doctor of Philosophy in the
School of Materials Science and Engineering

Georgia Institute of Technology
August 2007

SIMULATION AND CHARACTERIZATION OF CATHODE REACTIONS IN SOLID OXIDE FUEL CELLS

Approved by:

Dr. Meilin Liu, Advisor
School of Materials Science and Engineering
Georgia Institute of Technology

Dr. Comas Haynes
Georgia Tech Research Institute
Georgia Institute of Technology

Dr. Rosario Gerhardt
School of Materials Science and Engineering
Georgia Institute of Technology

Dr. Mo Li
School of Materials Science and Engineering
Georgia Institute of Technology

Dr. Paul H. Wine
School of Chemistry and Biochemistry
Georgia Institute of Technology

Date Approved: June 25, 2007

ACKNOWLEDGEMENTS

These acknowledgements must inevitably begin with those from whom I have drawn all my strength to finish this endurance race, my family. First and foremost, my mother, Cynthia, who has instilled in me the work ethic I need to get this far and who has proudly supported me throughout my academic career. My brother, Michael, my uncles, my grandparents and my cousins have all been there to provide unending support for me. Finally, my new family. I'd like to thank my wife, Melissa, and son Michael, who have given me a reason to forgo a lifelong career as a student and actually begin my adult life.

I would also like to thank the GEM Consortium, the National Science Foundation, the Department of Energy, and the Georgia Tech FACES program, all of who have provided the financial support I needed to complete this journey. Additionally, none of this work would have made it to completion without the help and support from the members our research group in the Solid State Ionics lab. And I can't forget my friends. Without you guys, this nearly six year journey might only have taken four but would have been nowhere near as fun.

Finally, I would like to thank my advisor Dr. Meilin Liu for his seemingly infinite wisdom and guidance throughout. You were always there to provide focus when needed and immensely accommodating of whatever trials and roadblocks have arisen over the years.

All of you have had a huge and life-long impact on me, and I truly feel blessed to have had you in my life. Thank you.

TABLE OF CONTENTS

LIST OF TABLES

LIST OF FIGURES

LIST OF SYMBOLS AND ABREVIATIONS

Roman Symbols

A	State-space state matrix
ad	Surface adsorption site
B	Grain size of electrolyte material in the electrode
B	State-space input matrix
B_0	Permeability
C	State-space output matrix
$C_i(0,t)$	Concentration of species i at the electrode surface at time t
C_i^*	Bulk concentration of species i
C_{dl}	Double layer capacitance
d	Pore diameter
D	State-space feed through matrix
D	Diffusion coefficient (cm^2/s)
E	Cell voltage (V)
E_a	Activation energy
EDX	Energy dispersive x-ray
EIS	Electrochemical impedance spectroscopy
e'	Electron
F	Faraday constant (96485 C/mol)
GDC	Gadolinium doped ceria
H(s)	Transfer function
I	Identity matrix
i	Current density (A/cm^2)
i_0	Exchange current density (A/cm^2)
J	Total flux
J_i	Flux of species i
j	Imaginary number (equal to $\sqrt{-1}$)
K	Equilibrium constant
k_i	Forward rate constant for reaction step *i*
$k_{\bar{i}}$	Reverse rate constant for reaction step *i*
$\langle L_A \rangle$	Average line length per unit area
LSM	Strontium doped lanthanum manganate
LTI	Linear time invariant
l_i	Thickness of component i
M	Molecular mass (g/equivalent)
MIEC	Mixed ionic electronic conductor
n	Number of electrons transferred for the reaction
n_i	Concentration of species i
O_O^X	Oxygen occupying an oxygen site
$\langle P_L \rangle$	Average number of intersections per line length

p	Pressure (atm)
p^0	Inlet pressure (atm)
R	Universal gas constant (8.314 J/mol/K)
R_{ct}	Charge transfer resistance (Ω)
$\overline{R}_{ct}$	Area specific charge transfer resistance (Ω·cm^2)
R_e	Electroylte resistance (Ω)
$\overline{R}_e$	Area specific electrolyte resistance (Ω·cm^2)
R_P	Polarization resistance (Ω)
$\overline{R}_P$	Area specific polarization resistance (Ω·cm^2)
r	Particle radius or electrons transferred during rate limiting step
S	Surface area of the porous solid (m^2/kg)
s	Laplace variable
$SOFC$	Solid oxide fuel cell
T	Temperature (K unless otherwise noted)
TPB	Triple phase boundary
$\overline{U}$	Velocity of the gas molecule (m/s)
$V_O^{\bullet\bullet}$	Oxygen vacancy
x_i	Mole fraction of component i
Y	Complex admittance function
YSZ	Yttria stabilized zirconia
Z	Complex impedance function

Greek Letters

α	Real charge transfer coefficient
β_t	Apparent charge transfer coefficient/symmetry coefficient
ε	Porosity
Γ	Total number of surface adsorption sites
γ_a	Number of electrons transferred after the rate limiting step
γ_b	Number of electrons transferred before the rate limiting step
μ	Viscosity or average particle size
η	Applied overpotential
η_{act}	Activation polarization
η_{Con}	Concentration polarization
η_{Ohm}	Ohmic polarization
ν	Number of iterations of the rate limiting step
θ_i	Fractional coverage of adsorbed intermediate *i*
$\dot{\theta}_i$	Time derivative of the fractional coverage of adsorbed intermediate *i*
ρ_{Bulk}	Bulk density of the solid particle (kg/m^3)
σ_{AB}	Collision diameter (Å)
σ_{CV}	Entropy production in control volume
σ_i	Conductivity of component I (S/cm) or standard deviation
σ_c	Overlap parameter for percolation simulation

τ	Tortuosity
Ω_{AB}	Collision integral, based on the Lennard-Jones potential
ω	Frequency

Subscripts and Superscripts

A	Species A
a	Anodic
ad	Adsorbed species
ads	Adsorbtion
B	Species B
C	Cathodic
ct	Charge transfer
cv	Control volume
des	Desorption
e	Electrolyte
eq	Equilibrium
F	Faradaic
Im	Imaginary portion of complex term
K	Knudsen diffusion
°	Reference state
(eff)	Effective property
Re	Real portion of complex term

SUMMARY

In this study, we have developed a dense $La_{0.85}Sr_{0.15}MnO_{3-\delta}$ (LSM) – $Ce_{0.9}Gd_{0.1}O_{1.95}$ (GDC) composite electrode system for studying the surface modification of cathodes. The LSM and GDC grains in the composite were well defined and distinguished using energy dispersive x-ray (EDX) analysis. The specific three-phase boundary (TPB) length per unit electrode surface area was systematically controlled by adjusting the LSM to GDC volume ratio of the composite from 40% up to 70%. The TPB length for each tested sample was determined through stereological techniques and used to correlate the cell performance and degradation with the specific TPB length per unit surface area.

An overlapping spheres percolation model was developed to estimate the activity of the TPB lines on the surface of the dense composite electrodes developed. The model suggested that the majority of the TPB lines would be active and the length of those lines maximized if the volume percent of the electrolyte material was kept in the range of 47 – 57%. Additionally, other insights into the processing conditions to maximize the amount of active TPB length were garnered from both the stereology calculations and the percolation simulations.

Steady-state current voltage measurements as well as electrochemical impedance measurements on numerous samples under various environmental conditions were completed. The apparent activation energy for the reduction reaction was found to lie somewhere between 31 kJ/mol and 41 kJ/mol depending upon the experimental conditions. The exchange current density was found to vary with the partial pressure of oxygen differently over two separate regions. At relatively low partial pressures, i_0 had an

approximately $p_{O_2}^{0.17}$ dependence and at relatively high partial pressures, i_0 had an approximately $p_{O_2}^{0.35}$ dependence. This led to the conclusion that a change in the rate limiting step occurs over this range.

A method for deriving the electrochemical properties from proposed reaction mechanisms was also presented. State-space modeling was used as it is a robust approach to addressing these particular types of problems due to its relative ease of implementation and ability to efficiently handle large systems of differential algebraic equations. This method combined theoretical development with experimental results obtained previously to predict the electrochemical performance data. The simulations agreed well the experimental data and allowed for testing of operating conditions not easily reproducible in the lab (e.g. precise control and differentiation of low oxygen partial pressures).

CHAPTER 1

INTRODUCTION

Continued world economic growth is directly dependent upon the availability of affordable and renewable sources of energy. Though fossil fuels have sustained this growth throughout the last century, perpetual reliance on an energy source that is both limited in supply and highly harmful to the environment (in its extraction and utilization) is not a viable option. The potential economic and environmental payoffs have led to an explosion of research into alternative forms of energy generation and conversion. New technologies such as nuclear energy, wind energy, solar energy and fuel cells have all been shown to have promise as a possible future replacement for fossil fuels that provide most of its benefits and few of its harmful drawbacks.

Solid-state energy conversion devices such as solid oxide fuel cells (SOFC) are poised to become vital technologies in the coming years [1, 2]. This promise has garnered a tremendous amount of research into SOFCs, particularly in optimizing cell components, such as the electrode, and the kinetic processes occurring there. Though a large amount of kinetic data has been collected, wide discrepancies over its interpretation exist in the literature[3-28]. Even in well-studied simplified systems containing only a noble metal cathode and electrolyte, where electrochemical reactions can occur only at the gas-electrode-electrolyte interface, or three phase boundary (TPB), little consensus exists as to the mechanism of oxygen reduction and incorporation. This process can consist of several elementary steps including but not limited to: adsorption/desorption onto the

cathode, diffusion of oxide species, and electrochemical and chemical reactions occurring at interfaces. When the noble metal electrode is replaced by a mixed ionic electronic conductor (MIEC) the system becomes further complicated as, theoretically, the entire surface of the MIEC becomes electrochemically active. Agreement on the reaction mechanism on the anode when exposed to a hydrocarbon fuel is even worse.

Previous studies have shown that a large portion of energy losses occurring in SOFCs happen at the electrode interfaces[29]; thus, optimization of the electrode through greater understanding of processes occurring there has the potential to eliminate a major obstacle in SOFC development. Development of advanced models to simulate these processes provides a cost-effective and rapid method for electrode optimization. Such models would allow for quick screening of new materials for electrodes as well as provide important insight into current materials. Also, with knowledge of the reaction mechanism occurring, the materials could be fabricated to provide a dramatically improved environment that further facilitates that mechanism [2, 3, 8, 12, 16, 19, 25-27, 30-38].

Analysis of reaction mechanisms has been approached from a number of directions. It is a generally agreed upon notion that reduction/oxidation reactions do not occur in a single step, but rather in a sequence of elementary steps. Initial endeavors were limited to steady-state analysis, such as current-voltage measurements, but they can only give so much information and rarely give insight to the reaction rate constants for elementary steps. For this reason, more dynamic measurements are needed. Overwhelmingly, electrochemical impedance spectroscopy (EIS) has been the tool of choice. EIS is a small signal perturbation analysis that gives information about the dynamic frequency response of the system. It also allows for separation of bulk properties

from those occurring at interfaces. Though EIS is a powerful tool, mathematical interpretation of the data can quickly become very complex. Due to this, many researchers have employed an equivalent circuit analysis approach to explain the experimental data [5-8, 10, 12, 13, 16-18, 20, 25, 26, 29, 31, 32, 39-50].

In this research, reaction mechanisms occurring at the electrodes in SOFCs will be delineated through a variety of methods including mathematical analysis and EIS with equivalent circuit analysis. Successful description of the reaction mechanisms will allow for electrode optimization and give needed insight into the actual processes occurring at the interfaces.

Impact

It is hoped that the general methodology developed during this research will provide a framework to identifying and testing reaction mechanisms in various systems. Specific to fuel cells, this would help to achieve a rational design of electrodes by garnering a much better understanding of how kinetic properties are affected by experimental conditions. This will lead to fast optimization for new electrode systems. In addition, the proposed research will also give a prediction of the theoretical performance expected from a particular system. This will allow for a baseline comparison with experiment and help determine early on whether or not there are faults or other previously unknown occurrences going on in the system. Knowing the theoretical performance of a system can be invaluable for screening new materials as possible electrode candidates and it is hoped this research will help expedite the process.

CHAPTER 2

BACKGROUND

Solid Oxide Fuel Cells

Solid oxide fuel cells (SOFCs) are all solid state electrochemical devices which convert chemical energy directly into electrical energy. Because of this direct conversion, SOFCs have the potential for much higher system efficiencies than traditional energy generation technologies which first convert chemical energy to heat then to mechanical energy and finally to electricity. Additionally, SOFCs operate at a sufficiently high temperature that facilitates the use of byproduct heat in other areas of the system (such as fuel reforming) to further improve the efficiency of the system. During operation, an oxidant, typically air or oxygen, is reduced at the cathode while a fuel source, typically hydrogen or hydrocarbons, is oxidized at the anode. This is shown schematically in Figure 2-1.

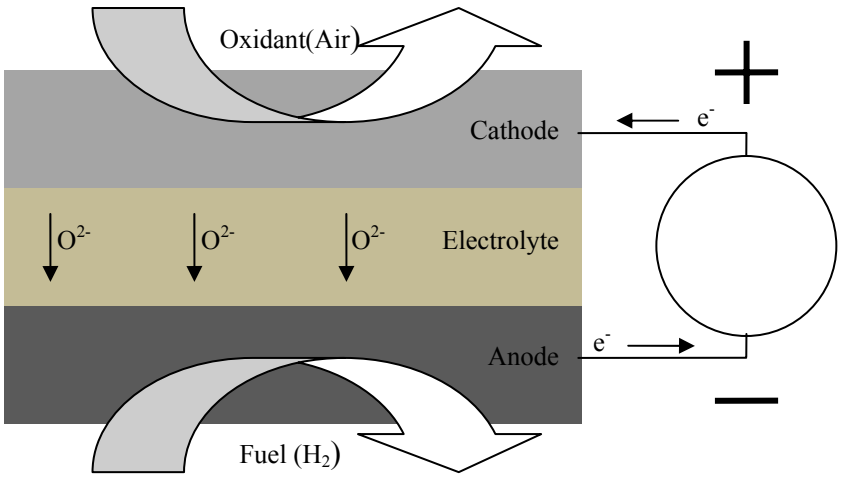

Figure 2-1. Schematic of a solid oxide fuel cell (SOFC)

Current generation SOFCs typically make use of a mixed ionic electronic conducting ceramic (MIEC) as cathode, yttria-stabilized zirconia (YSZ) electrolyte and nickel YSZ cermet for the anode. Due to the low conductivity of YSZ at lower temperatures as well as increased interfacial resistances between the electrodes and electrolyte, SOFCs typically operate in the range of 800-1000°C. At these temperatures, however, expensive interconnect materials are required and degradation of SOFC components is hastened. These factors have driven researchers to find new ways to reduce the operating temperature of SOFCs.

Xia and Liu showed that these interfacial resistances become a significant source of losses in the fuel cell at lower temperatures and the dominating source as the temperature is continuously lowered[29]. The brute force method to tackle this problem has historically been to discover new materials with higher conductivities at lower temperatures or redesigning the microstructure of existing materials to obtain performance gains. These are often slow and tedious approaches with little direction. Also, the optimal microstructure for one material is not necessary the same for the next. The problems arise from a general lack of understanding the mechanisms by which the electrochemical processes are occurring. This step is often overlooked, when in fact it should direct the development of the microstructure so as to minimize losses from the reduction/oxidation reaction. Therefore, garnering a better understanding of the underlying electrochemical processes occurring can lead to a directed and faster optimization of SOFC components.

The various components for SOFCs have very specific requirements which rule out most traditional materials. Some specific requirements include: stability,

conductivity, porosity and thermal expansion. These component specific requirements as well as traditional material choices will now be discussed.

Electrolyte

The function of the electrolyte in a SOFC is to be a medium for ionic conduction between the cathode and the anode. The ions under consideration for the SOFCs used in this study are oxygen anions. Because the electrolyte is in contact with both the cathode and anode environments it must be stable under both highly oxidizing and highly reducing environments. The following requirements for sufficient electrolyte performance were detailed by Minh and Takahashi[51]:

Stability

The electrolyte must be chemically, morphologically, and dimensionally stable in both the oxidizing atmosphere on the cathode side as well as the reducing atmosphere on the anode side. Disruptive phase transformations, including ones that lead to changes in molar volume or ionic conductivity, during temperature cycling can have detrimental effects on SOFC performance.

Conductivity

The electrolyte material should possess adequate ionic conductivity and negligible electronic conductivity at the SOFC operating conditions. The ionic conductivity should be as large as possible to minimize ohmic losses in the cell. The electronic conductivity

should be as small as possible to prevent parasitic currents from flowing from the anode to the cathode. The conductivity should also remain fairly invariant with time.

Porosity

Gas leakage through the electrolyte is highly damaging to the SOFC performance and thus the electrolyte should be as fully dense as feasible. If pores are present, they should be isolated and non-connecting. Additionally, the electrolyte should be impervious to both oxidant and fuel gases at all temperatures in the range between room temperature and operating temperature.

Thermal expansion

The thermal expansion of the electrolyte should match that of the adjacent cell components as closely as possible. Large differences in thermal expansion coefficients can lead to delamination, cracking and loss of performance. The thermal expansion coefficient should remain stable and fairly insensitive to changes in oxygen partial pressures in the both the fuel and oxidant gas streams.

Current material choices

By far, the most widely chosen material for electrolytes to date have been the stabilized zirconias, with yttria being the most common. YSZ exhibits no phase transformations over typical fuel cell operating temperature ranges and has sufficient conductivity of 0.12 $S \cdot cm^{-1}$ at 1000°C[52] that remains fairly stable with time and partial pressure of oxygen changes. Of note, YSZ will react with LSM at temperatures above

1100°C to form an insulating $La_2Zr_2O_7$ phase [13, 34, 46, 53] so care must be taken in choosing the processing conditions.

Doped ceria has also gained traction of late as a viable electrolyte material[54]. The principle dopant used is Gd_2O_3, though many other suitable dopants have been experimented with[1]. At a dopant level of 20% ($Ce_{0.8}Gd_{0.2}O_{1.95}$) GDC has a conductivity much higher than YSZ at a value of 8.3 $S \cdot cm^{-1}$ at 800°C[55]. GDC has not been shown to react negatively with LSM, but does exhibit some electrical conductivity under reducing atmospheres. Raising the dopant levels or changing the rare earth dopant have been shown to reduce electronic transference number[1, 55].

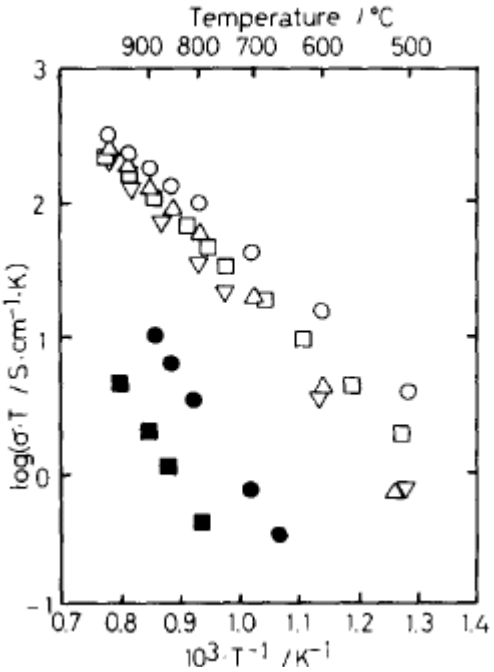

Figure 2-2. Arrhenius plots of ionic conductivities of various doped CeO_2 compounds. YSZ is shown for comparison. (○) $(CeO_2)_{0.8}(SmO_{1.5})_{0.2}$; (△) $(CeO_2)_{0.8}(GdO_{1.5})_{0.2}$; (▽) $(CeO_2)_{0.8}(YO_{1.5})_{0.2}$; (□) $(CeO_2)_{0.8}(CaO)_{0.2}$; (■)CeO_2;(●) $(ZrO_2)_{0.85}(YO_{1.5})_{1.5}$. Reproduced from Eguchi *et al* [1].

Cathode

The main function of the cathode is to provide a medium for the electrochemical reduction of oxygen. The cathode material must have sufficient catalytic activity towards oxygen reduction under the SOFC operating conditions. The following requirements for sufficient cathode performance were detailed by Minh and Takahashi[51]:

Stability

The cathode material must be chemically, morphologically, and dimensionally stable in the oxidant environment. The above must also maintain true for temperatures ranging from room temperature to the fabrication temperature (typically much higher than the operating temperature). No significant microstructure changes with time can be tolerated. The cathode is typically functionally graded and significant grain growth, for example, can be detrimental to its high performance through the reduction in TPB length.

Conductivity

To minimize ohmic resistance the cathode must possess sufficient electronic conductivity at the operating conditions. In effort to extend the TPB away from just the electrode/electrolyte interface, MIEC, which exhibit both electronic and ionic conduction, have been employed. These materials can potentially extend the TPB over the entire surface of the cathode. In practice, this extension is much more limited as the conduction of oxygen anions through the cathode material is a highly resistive process feasible only for conduction over short distances [56].

Porosity

The cathode must possess a level of porosity sufficient for rapid gas transport of oxygen to and water away from the active reaction sites, such as the TPBs. The upper limits on porosity are dictated by structural/mechanical and electrical transport concerns while the lower limits are dictated by mass transport concerns. Novel electrode structures currently employ a graded microstructure wherein the material contains large pores close to the gas stream for maximum mass transport into the electrode structure and smaller pores nearer the electrolyte interface for maximum number of active reaction sites. The bulk of the material provides a level of porosity need to insure structural integrity of the electrode (see Figure 2-3).

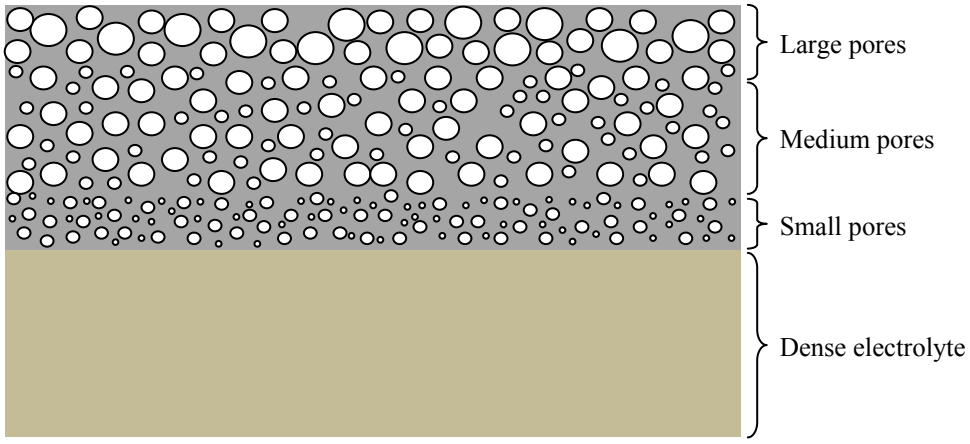

Figure 2-3. Schematic of a functionally graded cathode. Pore size is represented by the radius of the circles. Larger pores are nearer the gas interface to maximize mass transport. Medium sized pores exist in the bulk for structural/mechanical strength considerations. Smaller pores exist near the electrolyte interface to maximize the number of active reaction sites.

Thermal expansion

The thermal expansion of the cathode should match that of the adjacent cell components, such as the electrolyte, interconnect and seals, as closely as possible. Large differences in thermal expansion coefficients can lead to delamination, cracking and loss of performance. The thermal expansion coefficient should remain stable and fairly insensitive to changes in oxygen partial pressures in the oxidant gas stream.

Current material choices

Cathode materials choices for current generation SOFCs are limited to noble metals and electronic or MIEC oxides. This limitation is imposed by the high operating temperature and the highly oxidizing environment experienced. Though Pt and other noble metals performed adequately in the early developmental stages, their prohibitively high cost precludes their use in commercial SOFC development. The bulk of the development thus has been spent on doped metal oxides.

By far the most widely studied metal oxide system for SOFC cathode use has been lanthanum manganate ($LaMnO_3$). Doped $LaMnO_3$ has many promising attributes that have made it so attractive for cathode use including high electrical conductivity in oxidizing atmospheres, adequate thermal expansion match with other fuel cell components, and chemical compatibility with YSZ (at or below the fuel cell operating temperature). $LaMnO_3$ is a perovskite type oxide that consists of three interpenetrating material networks: one each consisting of the A and B cations and a third of corner-sharing O_6 octahedra (see Figure 2-4 below).

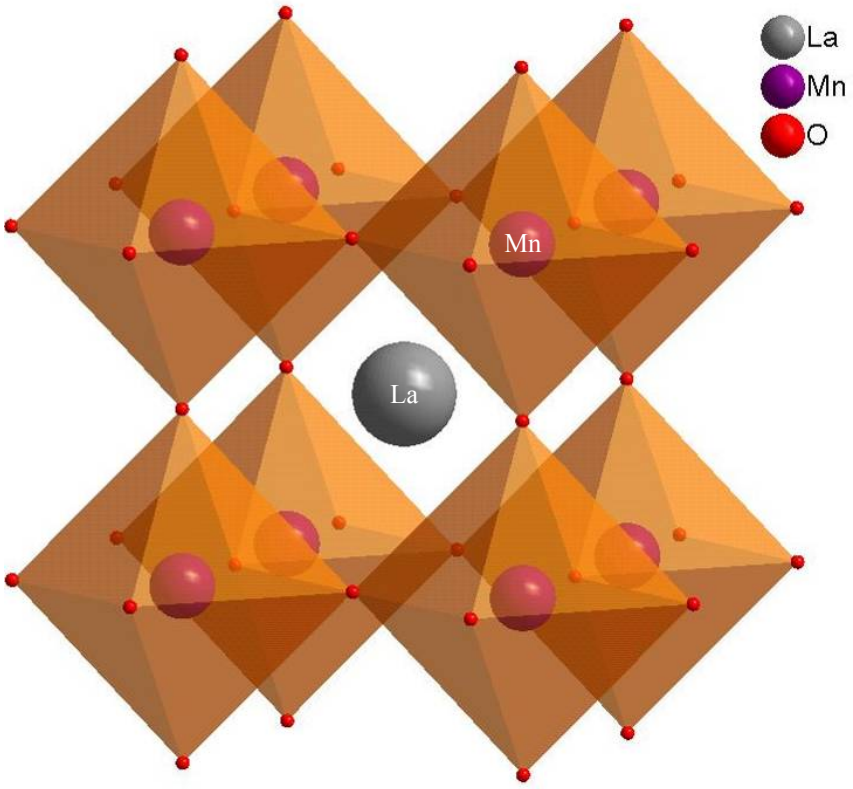

Figure 2-4. Ideal perovskite structure for $LaMnO_3$

$LaMnO_3$ is typically doped on the A site with a lower valence cation such as strontium (Sr^{2+}) which serves to increase the electronic conductivity of the material by increasing the Mn^{4+} concentration and provides better thermal expansion match with YSZ by increasing its thermal expansion coefficient; however, a high dopant content also results in reduced stability for the material[57]. Electronic conduction in LSM is believed to occur via the small polaron conduction mechanism wherein electron holes hop from manganese site to manganese site via an oxygen intermediate.

Anode

The main function of the anode is to provide a medium for the electrochemical oxidation of fuel (typically hydrogen). The following requirements for sufficient anode performance were detailed by Minh and Takahashi[51]:

Stability

The anode must be chemically, morphologically, and dimensionally stable in the reducing atmosphere at the fuel inlet as well as the slightly more oxidizing environment at the spent fuel exit. Disruptive phase transformations, including ones that lead to changes in molar volume or electronic conductivity, during temperature cycling can have detrimental effects on SOFC performance.

Conductivity

The anode material should possess adequate electronic conductivity in a reducing environment operating condition. The conductivity should be as large as possible to minimize ohmic losses in the cell. The conductivity should also remain fairly invariant with time.

Porosity

The anode must possess a level of porosity sufficient for it to allow gas transport to the reaction sites. The upper limits on porosity are dictated by structural/mechanical and electrical transport concerns while the lower limits are dictated by mass transport concerns.

Thermal expansion

The thermal expansion of the anode should match that of the adjacent cell components as closely as possible. Large differences in thermal expansion coefficients can lead to delamination, cracking and loss of performance. The thermal expansion coefficient should remain stable and fairly insensitive to changes in oxygen partial pressures in the fuel gas stream.

Current material choices

Current generation SOFCs typically make use of a cermet between nickel and the electrolyte material, in general YSZ. Nickel is the material of choice for anodes due to its low cost as compared to other precious metals and its high reactivity towards hydrogen oxidation. The electrolyte material has a three-fold effect: to provide better thermal expansion match between the anode and other cell components, to act as a support structure, and to inhibit the nickel grain growth over the lifetime of the SOFC.

Interconnect

The theoretical maximum voltage for a single hydrogen/oxygen fuel cell is approximately 1.23V (in practice the value is always less due to resistive losses within the cell, higher operating temperatures and current draw). For this reason, cells are typically linked together in various series and parallel formations to obtain a desirable useful working voltage. The fuel cell schematic shown in Figure 2-1 is that of a single cell and thus, does not show the interconnect material. The main function of the

interconnect is to link adjacent cells to one another to form a fuel cell stack. The interconnect provides electrical connection between adjacent cells as well as an impermeable barrier to each cell's respective gas stream. The following requirements for sufficient anode performance were detailed by Minh and Takahashi[51]:

Stability

The interconnect must be chemically, morphologically, and dimensionally stable in both the reducing atmosphere on its fuel side as well as the oxidizing environment on its cathode side. As mentioned above, the interconnect electrically joins the cathode of a cell to the anode of the next cell and thus will experience this dual gas environment. Disruptive phase transformations, including ones that lead to changes in molar volume or electronic conductivity, during temperature cycling can have detrimental effects on SOFC performance.

Conductivity

The interconnect material should possess adequate electronic conductivity in both a reducing environment and an oxidizing environment at the fuel cell operating conditions. The conductivity should be as large as possible to minimize ohmic losses. The conductivity should also remain fairly invariant with time.

Porosity

Gas leakage through the interconnect is highly damaging to the SOFC performance and thus the interconnect should be as fully dense as feasible. If pores are

present, they should be isolated and non-connecting. Additionally, the interconnect should be impervious to both oxidant and fuel gases at all temperatures in the range between room temperature and operating temperature.

Thermal expansion

The thermal expansion of the interconnect should match that of the adjacent cell components as closely as possible. Large differences in thermal expansion coefficients can lead to delamination, cracking and loss of performance. The thermal expansion coefficient should remain stable and fairly insensitive to changes in oxygen partial pressures in both the fuel gas stream and the oxidant gas stream.

Current material choices

Current generation SOFCs typically make use of a chromium based ceramic material for use as an interconnect. Lanthanum chromate has been the most commonly used oxide system but other researchers have also used materials such as $FeNiCr_5$ as an interconnect material[58]. These researchers also managed to use the interconnect material as part of a hermeticly sealed SOFC without the use of external sealants.

A summary of the requirements for each of the above discussed fuel cell components is given in Table 2-1 below.

Table 2-1. Summary of requirements for ceramic fuel cell components (reproduced from Minh and Takahashi[51])

Component	Requirements				
	Conductivity	Stability	Compatibility	Porosity	Thermal Expansion
Electrolyte	High ionic conductivity and negligible electronic conductivity	Chemical, phase, morphological and dimensional stability in fuel and oxidant environments	No damaging chemical interactions nor interdiffusion with adjoining cell components	Fully dense	Thermal expansion match with adjoining components
Cathode	High electronic conductivity	Chemical, phase, morphological and dimensional stability in oxidant environments	No damaging chemical interactions nor interdiffusion with adjoining cell components	Porous	Thermal expansion match with adjoining components
Anode	High electronic conductivity	Chemical, phase, morphological and dimensional stability in fuel environments	No damaging chemical interactions nor interdiffusion with adjoining cell components	Porous	Thermal expansion match with adjoining components
Interconnect	High electronic conductivity and negligible ionic conductivity	Chemical, phase, morphological and dimensional stability in fuel and oxidant environments	No damaging chemical interactions nor interdiffusion with adjoining cell components	Fully dense	Thermal expansion match with adjoining components

Kinetic Modeling

Mass and charge balances are typically the starting point for mathematical treatment of kinetic modeling. The equations obtained from these relations typically allow for time-independent analytical solutions to steady-state systems. Difficulties arise in the case of multi-step reactions where the interplay between the differential equations describing the system can become hectic. Several authors have applied an empirical Butler-Volmer type relationship where all but one step, the rate-limiting one, is considered to be at equilibrium[3, 26, 27, 30]. These models give an effective current/overpotential relationship such as:

$$i = i_0 \left[\exp\left(\frac{nF\alpha_a}{RT}\eta \right) - \exp\left(-\frac{nF\alpha_c}{RT}\eta \right) \right] \tag{2.1}$$

where i and i_0 are the current density and exchange current density, α_i are the charge transfer coefficients, F is Faraday's constant, R is the gas constant, T is temperature and η is applied overpotential. The main drawback of this approach is the lack of generality as it oftentimes fails to account for the convoluted manner in which the various reaction steps contribute to the overall impedance[6, 34]. Rarely does one step in the electrode reaction mechanism completely and overwhelming dominate all others. Because this expression defines the mechanism with only a few kinetic constants, they may allow for accurate data fitting, but give little insight to the elementary reaction steps.

Several types of electrode reactions can occur at various points in the electrode, including the exterior electrode surface, the interior electrode pore surface and at the TPB. The particular electrode/electrolyte material system determines which reactions will

actually manifest. Five main types of reaction steps are generally considered: gas-phase reactions, adsorption/desorption, dissociation, diffusion and charge transfer. Gas phase reactions are more prevalent at the anode than the cathode due to number of chemical species present. For instance, at the cathode, the only reacting species in the oxidant stream tends to be molecular oxygen. In contrast, several reacting species can exist in the fuel stream including hydrogen, water, hydrocarbons, and carbon monoxide just to name a few. Adsorption/desorption refers to the way in which an atomic species or molecule adheres to the surface. The surface in question includes both the internal and the external surfaces of the electrode. For molecules, adsorption can occur either associatively or dissociatively, meaning that the molecule itself adsorbs to the surface or it first dissociates into another species before adsorbing. If associative adsorption occurs, then the possibility of dissociation of the molecule exists. For example, if an oxygen molecule adsorbs to the cathode surface, it may dissociate into adsorbed oxygen atoms. Diffusion refers to the movement of any surface adsorbed species or movement of an ionic species through the bulk of an MIEC electrode under the influence of either a chemical gradient or a potential gradient. The last type of reaction to be considered is charge transfer. This step involves transfer of electrons and occurs either on the surface of the electrode to an adsorbed species or at the TPB where incorporation/evolution occurs. The five main types of elementary reaction steps to be considered are shown schematically in Figure 2-5.

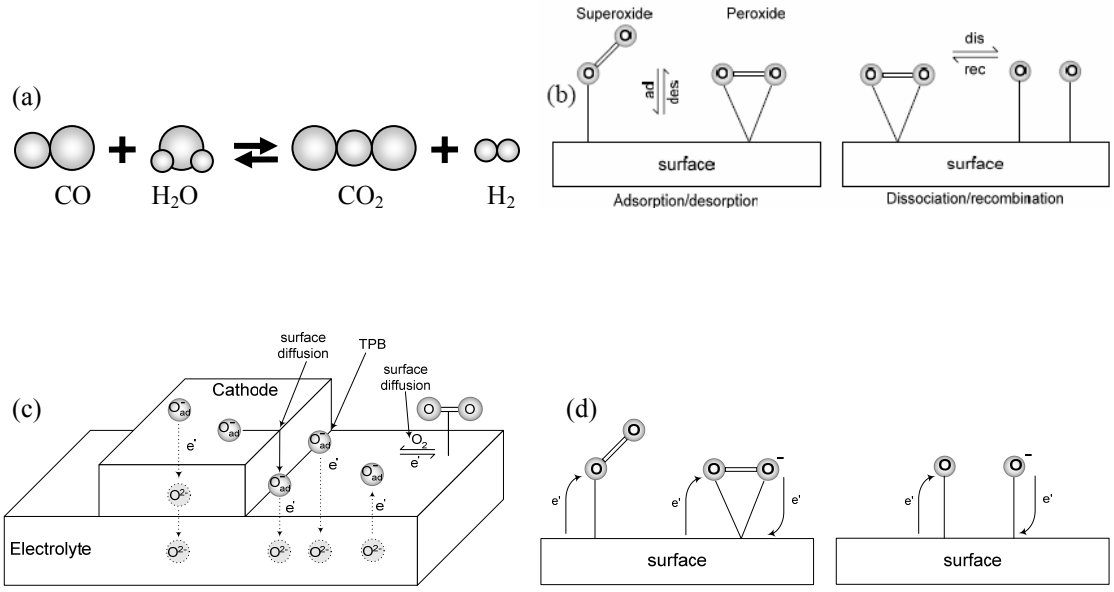

Figure 2-5. Schematic showing the main types of reactions under consideration including (a) gas phase, (b) adsorption/desorption and dissociation, (c) bulk and surface diffusion, and (d) charge transfer reactions.

Electrochemical Impedance Spectroscopy

Electrochemical impedance spectroscopy (EIS) is a method of characterizing many of the electrochemical properties of materials and their interfaces using electronically conducting electrodes[59]. EIS is typically measured by applying a small signal AC potential to the system over a wide frequency range and measuring the resulting current output. One of the basic assumptions of EIS is that linearity of the system prevails and using a small signal perturbation (1 – 20mV) typically confines the systems to this regime. The current response of the system contains the excitation frequency and its harmonics and these can be analyzed using Fourier transforms. The impedance of the system, *Z*, in an expression analogous to Ohm's Law, is thus a ratio of the applied sinusoidal potential to the resulting sinusoidal current:

$$Z = \frac{E(\omega)}{I(\omega)} = \frac{E_0 \cos(\omega t)}{I_0 \cos(\omega t - \varphi)} = Z_0 (\cos\varphi + j \sin\varphi) \quad (2.2)$$

EIS data are typically analyzed through the use of equivalent circuit models. This involves the use of electrical components (resistors, capacitors and inductors) to model the physical electrochemistry occurring in the system. The mathematical representations for these circuit elements are given below in Table 2-2. EIS models typically consist of a network of circuit elements in various serial and parallel configurations. When combining impedances in series, the elements sum directly to give to the total impedance. When combing impedances in parallel, the reciprocal of the elements sum to give the reciprocal of the total impedance. Data are typically presented in the form of a Nyquist plot (see Figure 2-6) where the real and imaginary parts of impedance are plotted versus each other or Bode plots where the both the absolute value of impedance and phase shift on the y-axis are plotted versus log of frequency on the x-axis.

Table 2-2. Mathematical representations of impedance circuit elements

Electrical Element	Current/Voltage Relationship	Impedance Expression
Resistor	$E = IR$	$Z_R = R$
Capacitor	$I = C\frac{dE}{dt}$	$Z_C = \frac{1}{j\omega C}$
Inductor	$E = L\frac{dI}{dt}$	$Z_L = j\omega L$

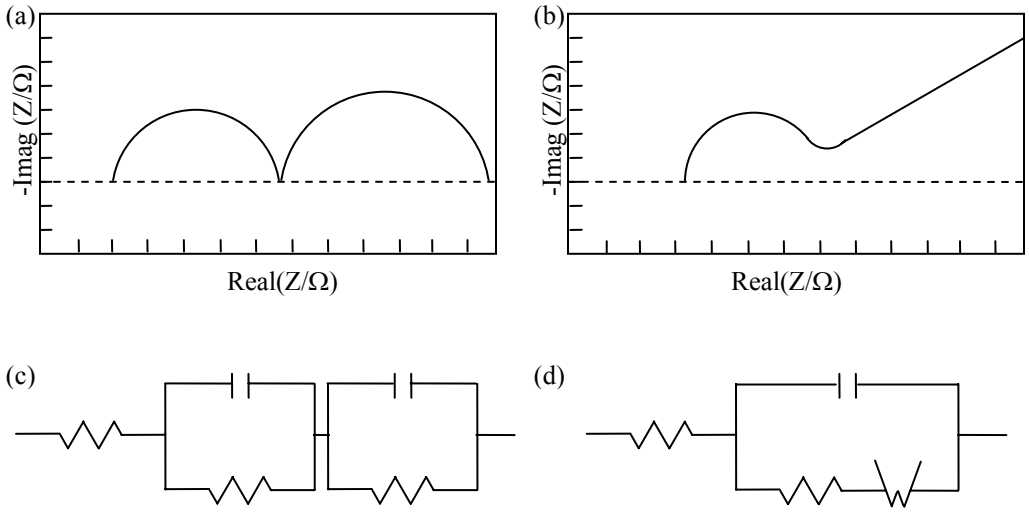

Figure 2-6. Typical impedance spectra showing (a) a series of kinetic processes, (b) a combination of kinetic and diffusion process, and their possible equivalent circuit representations in (c) and (d), respectively

These circuit elements are used to represent some physical aspects of the system. Capacitors typically model physical elements such as the double layer capacitance which exists when an electric double layer develops at the interface of an electrode. Resistors are used to model bulk resistance which arises from the opposition to flow of charged species, charge transfer resistance which can appear from a kinetically controlled electrochemical reaction and polarization resistance which develops whenever the electrode is forced away from its equilibrium potential. Diffusion will create a special kind of impedance called Warburg impedance that is a function of the frequency of the potential perturbation. Inductance is a less common feature in EIS systems, but can arise from an overlapping of several potential dependent processes or from the lead wires or equipment (this latter case would constitute an error in the analysis)[59]. Double layer

capacitance, bulk resistance, charge transfer resistance, polarization resistance, and diffusion can all be adequately modeled using these circuit elements.

Though EIS is a powerful tool, one of the main limitations of the technique is the lack of uniqueness of an equivalent circuit that describes its generated spectrum. Figure 2-6(c) is only one of several possible equivalent circuits that will reproduce the spectrum in Figure 2-6(a). Additional knowledge of the system is needed to accurately develop its physical model and these should, in turn, be verified wherever possible (e.g. modifying a system parameter and checking for the expected change in the impedance spectra).

State Space Modeling Approach

The state-space representation has been shown to be one of the most reliable linear time-invariant (LTI) models to use for computer analysis[16, 25-27, 60]. Researchers have shown the applicability of using a transfer function description along with the state-space model and that will be extended for this study[25-27]. The state-space modeling approach is a control theory approach to addressing differential algebraic equations of dynamic systems. It uses a combination of experimental data, modeling and simulation to identify reaction mechanisms in various systems[16]. The experimental data are used to help elucidate a practical reaction mechanism and to provide kinetic information such as rate constants.

State variables represent the smallest subset of system variables needed to completely describe the system under study at any given time. The variables are linearly independent and the minimum number of state variables required to define a system is on the order of the primary differential system equation. For transfer function

representations, the minimum number of state variables is equal to the transfer function's denominator, when in its reduced form[61, 62].

Several expressions of the state-space type are available, but these studies will focus on the continuous linear time-invariant systems (LTI). Under this description, the general state-space representation of a system with p inputs, q outputs and n state variables is expressed as

$$\begin{aligned} \dot{x}(t) &= \mathbf{A}x(t) + \mathbf{B}u(t) \\ y(t) &= \mathbf{C}x(t) + \mathbf{D}u(t) \end{aligned} \tag{2.3}$$

within the domains and dimensions of

$$x(t) \in \mathbb{R}^n \quad y(t) \in \mathbb{R}^q \quad u(t) \in \mathbb{R}^p$$
$$\dim[\mathbf{A}] = n \times n \quad \dim[\mathbf{B}] = n \times p \quad \dim[\mathbf{C}] = q \times n \quad \dim[\mathbf{D}] = q \times p$$

$\dot{x}(t)$ is the time derivative of the x. x is known as the state vector, y is known as the output vector, and u is known as the input vector. The matrices that describe the system are **A**, the state matrix, **B**, the input matrix, **C**, the output matrix and **D**, the feed-through matrix. Because the systems under consideration are LTI systems, all of the system matrices are time-invariant also.

A transfer function description of the system can be garnered from the state-space description through the use of Laplace transforms. The transfer function is defined as the ratio of the output to the system to the input to the system. Care must be taken in converting from a state-space description to a transfer function description as loss of some internal information about the system may occur, providing a description of a system which is stable when the state-space description was unstable under certain conditions[62].

The state-space description of the models under study is as follows:

$$\begin{aligned} \dot{\theta} &= \mathbf{A}\theta + \mathbf{B}\eta \\ I_F &= \mathbf{C}\theta + \mathbf{D}\eta \end{aligned} \tag{2.4}$$

Here, θ is the vector of fractional coverage of adsorbed species, η is the applied overpotential and I_F is the faradaic current. The constants **A**, **B**, **C**, and **D** are matrices that will uniquely describe the system under study. The modeling aspect, represented by Equation(2.4) , places the whole system under study into a system of coupled differential algebraic equations. Typically, these resulting equations do not have an analytical solution and must be further conditioned for numerical simulation. Simulation is the final step in the state-space modeling approach and provides a means to evaluate the model developed and a way to interpret data obtained from the model.

Polarization Effects

A typical schematic of a voltage versus current trace for an SOFC is shown in Figure 2-7. The plot is nonlinear and contains three areas of interest: a concave up region at low current densities, a linear region at intermediate current densities and a convex up region at high current densities.

The initial concave up curvature ($d^2V/di^2 \geq 0$) observed is typically attributed to activation polarization, while the convex up curvature ($d^2V/di^2 \leq 0$) seen at higher current densities is attributed to the concentration polarization. The linear region at intermediate current densities is attributed to ohmic losses.

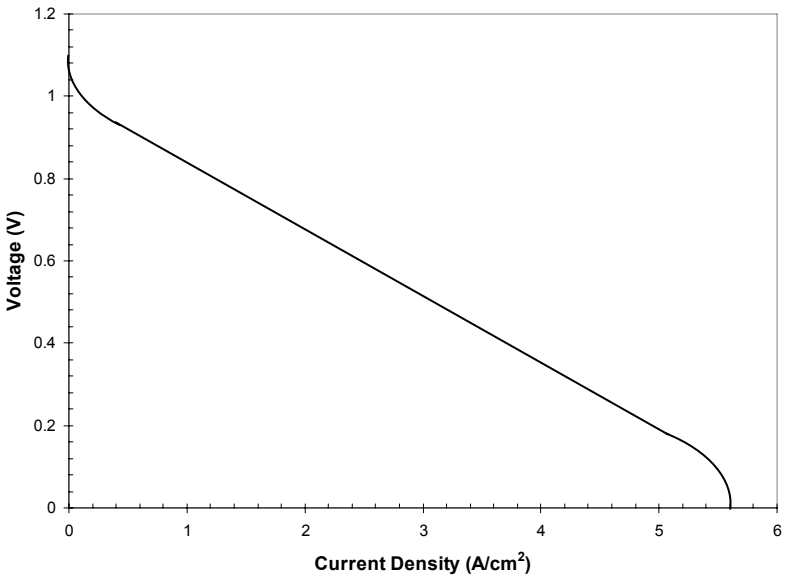

Figure 2-7. Typical voltage vs. current trace for an SOFC

Activation polarization (charge transfer resistance)

For chemical and electrochemical reactions to proceed, they must overcome certain energy barriers called the activation energy. The activation energy barrier is due to the transfer of charge between electronic and ionic conductors (and is typically called the charge transfer resistance) and results in an activation polarization imposed on cell. When solutions are well stirred, or currents are kept low enough so that the bulk concentrations of reacting species do not differ appreciably from those at the electrode surface (this situations effectively eliminate mass transport limitations), the activation polarization can be adequately described by the Butler-Volmer equation (Equation (2.1)). Additionally, if the above criterium of a well-stirred solution is not met, the Butler-Volmer equation can still be used, just with certain modifications.

When the charge transfer coefficient is taken as 0.5, simplifications to the Butler-Volmer equation arise. Rearrangement of the equation leads to an expression for the activation polarization as:

$$\eta_{act} = \frac{2RT}{nF} \sinh^{-1}\left(\frac{i}{2i_0}\right) \tag{2.5}$$

Additionally, the Butler-Volmer description leads to two special polarization conditions: high activation and low activation polarization. Under high activation polarization, the second exponential term diminishes and, through rearrangement, we arrive at the Tafel equation[63-65]:

$$\eta_{act} = -\frac{RT}{n\alpha F} \ln i_0 + \frac{RT}{n\alpha F} \ln i \tag{2.6}$$

Again, because of the assumption of large values of η_{act}, this assumption typically holds for cathodic overpotentals (where the values are typically much larger than on the anode side) but not for anodic overpotentials. For low activation polarization, typically a Taylor series approximation is performed and neglecting the higher order terms leaves

$$\eta_{act} = \frac{RT}{nFi_0} i \tag{2.7}$$

Recognizing the ohmic relationship between voltage and current, Equation (2.7) can further be simplified to

$$R_{ct} = \frac{RT}{nFi_0} \tag{2.8}$$

where R_{ct} is an expression for the charge transfer resistance.

Ohmic polarization

Ohmic losses occur from resistance to the flow of charge in the fuel cell components. This includes ions in the electrolyte and electrons in the electrodes. Typically, these losses are overwhelmingly dominated by the electrolyte. Because the ionic flow obeys Ohm's law the ohmic polarization can be defined as

$$\eta_{Ohm} = iR_e \tag{2.9}$$

Some researchers have taken this concept one step further and included an effective charge transfer resistance to account for the phenomenon where the reaction zone is spread out some distance from the electrode/electrolyte interface[66]. This assumption of including the charge transfer resistance as part of the ohmic polarization is not exclusive of using the Butler-Volmer equation to describe activation polarization. In fact, they can both be used in tangent because in cases where it is prudent to use the Butler-Volmer equation, the reaction zone spreads out some distance from the electrode/electrolyte interface into the electrode[67]. Tanner *et al.* redefined the area specific resistance of the electrolyte, R_i, to be a sum of the ohmic resistance and what they now termed an effective charge transfer resistance defined as

$$R_{ct}^{eff} = \frac{BR_{ct}}{B\left[\frac{1+\varphi}{1+\varphi\exp\left(-\frac{2l_e}{\kappa}\right)}\right]\left(1-\varepsilon\right)\exp\left(-\frac{l_e}{\kappa}\right)+\left[\frac{1+\varphi\exp\left(-\frac{l_e}{\kappa}\right)}{1+\varphi\exp\left(-\frac{2l_e}{\kappa}\right)}\right]\kappa\left[1-\exp\left(-\frac{l_e}{\kappa}\right)\right]+B\varepsilon} \tag{2.10}$$

where

$$\kappa = \sqrt{\sigma_e B\left(1-\varepsilon\right)R_{ct}} \text{ and } \varphi = \frac{\sigma_e R_{ct} - \kappa}{\sigma_e R_{ct} + \kappa}$$

This much more rigorous approach has been shown to garner more precise predictions about the ohmic polarization than those previously to date[66].

Concentration overpotential

The rate of mass transport to the reaction sites is a diffusion limited process. The situation is further complicated in that the diffusion occurs through a porous electrode. Isothermal transport of gases through a porous media can be broken up into ordinary diffusion and Knudsen diffusion. Ordinary diffusion occurs when the pore diameter is significantly larger than the mean free path of the gas molecules. Conversely, Knudsen diffusion governs when the gaseous transport is through pores that are small in comparison with their mean free path. Under Knudsen diffusion, molecules collide much more frequently with the pore walls than in ordinary diffusion and this effect further impedes the diffusion process[68].

Oridinary diffusion coefficients for a binary gas system can be calculated using the Chapman-Enskog theory[69]

$$D_{AB} = 0.0018583 \cdot \left(\frac{1}{M_A} + \frac{1}{M_B} \right)^{0.5} \cdot \frac{T^{1.5}}{p\sigma_{AB}^2 \Omega_{DAB}} \tag{2.11}$$

where D_{AB} is the binary diffusion cofficient, M is the molecular mass, T is the temperature, p is the pressure, σ_{AB} is the collision diameter of two molecules, and Ω_{AB} is the collision integral. To account for the non-linear or tortuous path the gas molecules must traverse and that the diffusion only occurs inside the pores of the material, the diffusion coefficient can be modified to give an effective diffusion coefficient

$$D_{AB(eff)} = D_{AB} \frac{\varepsilon}{\tau} \tag{2.12}$$

where ε is the porosity and τ is the tortuosity. For the particular system of interest (humidified H_2 as fuel and air as the oxidant) experiments have shown that the binary diffusion coefficients at room temperature are $D_{O_2-N_2} \approx 0.22\ cm^2/s$ and $D_{H_2-H_2O} \approx 0.91\ cm^2/s$ [70]. The Knudsen diffusion coefficient can be predicted using kinetic theory by relating the diameter of the pore and the mean free path of the gas by the expression[71]

$$D_{A,K} = \frac{\bar{U}d}{3} \tag{2.13}$$

where the subscript *k* denotes Knudsen diffusion, *d* is the pore diameter and $\bar{U}$ is the velocity of the gas molecules. For straight, round pores, the diffusion coefficient of component A becomes

$$D_{A,K} = 97.0r\left(\frac{T}{M_A}\right)^{0.5} \tag{2.14}$$

where *r* is the mean pore radius defined by the bulk density, ρ_{bulk}, the surface area of the porous solid, *S*, and the porosity by

$$r = \frac{2\varepsilon}{S\rho_{Bulk}} \tag{2.15}$$

An effective Knudsen diffusion coefficient can be defined similar to the effective ordinary diffusion coefficient by

$$D_{A,K(eff)} = D_{A,K}\frac{\varepsilon}{\tau} \tag{2.16}$$

Both ordinary and Knudsen diffusion may occur at the same time. For equimolar counter transfer (as seen in the anode side), the effective diffusion coefficient in a porous material is defined as

$$\frac{1}{D_{A(eff)}} = \frac{1}{D_{AB(eff)}} + \frac{1}{D_{A,K(eff)}} \tag{2.17}$$

The governing equations for isothermal gas transport through porous media for a binary mixture of gases A and B is given by[72]

$$J_A = -D_{A(eff)} \nabla n_A + x_A J \frac{D_{A,K(eff)}}{D_{A,K(eff)} + D_{AB(eff)}} - x_A \left(\frac{nB_0}{\mu} \right) \frac{D_{AB(eff)}}{D_{A,K(eff)} + D_{AB(eff)}} \nabla p \tag{2.18}$$

$$J_B = -D_{B(eff)} \nabla n_B + x_B J \frac{D_{B,K(eff)}}{D_{B,K(eff)} + D_{AB(eff)}} - x_B \left(\frac{nB_0}{\mu} \right) \frac{D_{AB(eff)}}{D_{B,K(eff)} + D_{AB(eff)}} \nabla p \tag{2.19}$$

The total flux of a species arises from two contributing factors: diffusive flux and viscous flux. For the limiting cases of one-dimensional diffusion, the diffusion coefficients, being composition independent, and the electrode microstructure, being position independent, researchers found that the partial pressures of hydrogen, water and oxygen in terms of the current density as [65, 67, 73]:

$$p_{H_2} = p^0_{H_2} - \frac{RTl_a}{2FD_{a(eff)}} i \tag{2.20}$$

$$p_{H_2O} = p^0_{H_2O} + \frac{RTl_a}{2FD_{a(eff)}} i \tag{2.21}$$

$$p_{O_2} = \frac{p_c}{\delta_{O_2}} - \left(\frac{p_c}{\delta_{O_2}} - p^0_{O_2} \right) \exp\left(\frac{\delta_{O_2} RTl_c i}{4FD_{O_2(eff)} p_c} \right) \tag{2.22}$$

where

$$\delta_{O_2} = \frac{D_{O_2,K(eff)}}{D_{O_2,K(eff)} + D_{O_2-N_2(eff)}} \text{ and } D_{a(eff)} = \left(\frac{p_{H_2O}}{p_a} \right) D_{H_2(eff)} + \left(\frac{p_{H_2}}{p_a} \right) D_{H_2O(eff)}$$

With these now known partial pressures, the concentration overpotential can be calculated from the Nernst equation.

Objectives

The main goal of this research is to gain a clear understanding of the types of reactions occurring in various domains of a SOFC and to delineate the mechanism by which oxidation/reduction of fuel/oxidant occurs. On the cathode side, various elementary reaction steps relevant to oxygen reduction will be considered in modeling of electrode reactions including oxygen adsorption/desorption, dissociation of oxygen molecules to atoms, ionization of adsorbed oxygen atoms or molecules, surface/bulk transport of adsorbed oxygen species, and combination reactions involving oxygen vacancies. More specifically, this research will achieve the following objectives:

- To determine the elementary steps involved in oxygen reduction at different sites on the cathode including the TPB and cathode surface to form a complete mechanism for oxygen reduction.
- To determine mathematical models for the proposed mechanisms occurring at the cathode electrode and simulate the electrochemical impedance responses expected from such mechanisms. This will be directly verified by impedance measurements.
- To determine the effect of operating conditions (such as oxidant/fuel partial pressure, temperature, and electrode polarization) on the simulated electrochemical impedance spectra.
- To verify the above mechanism by fabricating half cells and performing EIS analysis on them.

Organization of work

As mentioned previously, the literature contains numerous authors' research that has used mechanistic studies for probing the intricacies of electrode reactions [2, 3, 8, 10, 12, 14, 16, 17, 21, 24, 26, 27, 30, 34, 50, 53, 65, 74-76]. Even more specific, some authors have employed the state-space approach to their mechanistic and other studies [16, 25-27, 77]. The limitations of the majority of these models stem from their use of equivalent circuits to explain the experimental impedance data. Though complex non-linear least squares (CNLS) fitting, the method most typically used to fit proposed equivalent circuits to the experimental data, provides excellent matching of the models to the data, ultimately it requires that one have prior knowledge of exactly what the reaction mechanism is and what other losses occurring in the cell are. This method comes with a significant limitation as several vastly different equivalent circuits can reproduce the same datasets. Additionally, due to the nature of the CNLS fitting, there's no way to unambiguously determine if one proposed equivalent circuit is more correct than another, as adjusting the values of the equivalent circuit elements can give equivalent fits. Moreover, when auditioning new materials for potential electrode applications, prior knowledge of the system's kinetic response (information that will allow you develop an equivalent circuit for the system) is rarely available.

Another limitation of the equivalent circuit modeling approach arises when the experimental conditions are varied. Large changes in oxygen partial pressure or overpotentials applied to the cell, for example, can greatly influence the cell's responses and make a reaction pathway that was once rate limiting into an extremely facile process. The common technique in handling this problem with equivalent circuits is to propose a

different equivalent circuit for each experimental condition. This becomes prohibitive when dealing with numerous experimental parameters (such as oxygen partial pressure, temperature, overpotential, surface geometry, etc) and, thus, the proposed equivalent circuit's extent is limited to a small range of experimental conditions.

This study is divided into two main sections that will attempt to address the above concerns: an experimental approach to mechanism determination and a computational approach to the same problem. During the first section, we will develop a system that is an ideal platform for studying the oxygen reduction mechanism. Through a combination of steady-state and electrochemical spectroscopic experiments we will propose the steps by which oxygen is ultimately incorporated into the electrolyte lattice and under what conditions those mechanisms hold. The experimental data will give us insight into what experimental conditions lead to particular rate limiting steps. Additionally, close examination of the developed microstructure will allow us to correlate geometric changes into an overall mechanism for the system by changing the overall length of triple phase boundary. The second section will focus on using the experimental and microstructural data obtained in the previous section to first estimate kinetic parameters and then incorporate those parameters into a microkinetic model of the system. It is believed that this approach can better encompass changes in experimental conditions without the need to redesign models, as with the equivalent circuit approach.

CHAPTER 3

FABRICATION AND CHARACTERIZATION OF DENSE COMPOSITE ELECTRODES

Dense $La_{0.85}Sr_{0.15}MnO_{3-\delta}$ (LSM) – $Ce_{0.9}Gd_{0.1}O_{1.95}$ (GDC) composite electrodes have been developed for study of surface modification of cathodes. A dense LSM-GDC composite electrode is typically fabricated with a GDC electrolyte layer to form a bi-layer structure using a co-pressing and co-firing process. The LSM and GDC grains in the composite were well defined and distinguished using energy dispersive x-ray (EDX) analysis. The specific three-phase boundary (TPB) length per unit electrode surface area was systematically controlled by adjusting the LSM to GDC volume ratio of the composite from 40% up to 70%. The TPB length for each tested sample was determined through stereological techniques and used to quantitatively correlate the cell performance and degradation with the specific TPB length per unit surface area. This method provides an unambiguous way to measure the performance of an electrode and allows for an accurate comparison between samples of varying TPB length.

Introduction

The dense $La_{0.85}Sr_{0.15}MnO_{3-\delta}$ (LSM) – $Ce_{0.9}Gd_{0.1}O_{1.95}$ (GDC) composite electrode can provide some unique advantages to investigate cathodic reactions. First, all triple phase boundaries (TPB) are on the surface of the dense composite and can be well defined through ceramic processing. Again, the a TPB line is defined here as the interface

between the electrode, electrolyte and gas (or adsorbed intermediate). Many of the problems associated with kinetic studies on porous SOFC electrodes are avoided. Second, all potential electrochemical reactions will occur on the open surface, making them more accessible to the application of various characterization techniques (such as SEM, Raman spectroscopy, μ-impedance spectroscopy, etc). Third, it is possible to quantitatively correlate the cell performance and degradation with the specific triple phase boundary length/area per unit surface area. LSM was selected here because it is an electronic conductor whose ionic conductivity is typically negligible. GDC was used as the electrolyte material in place of the more widely used yttria-stabilized zirconia to avoid the formation of poorly conducting insulating phases[46]. In this case, it is reasonable to assume that the electrochemical processes will only take place along the TPB area.

Recently, other studies using various methods such as photolithography have been done to precisely control the TPB length[56, 78, 79]. While these methods are effective in producing cells with desired TPB lengths, they require multiple complex fabrication steps and typically necessitate the use of clean room facilities. Further, the detailed microstructure of the TPBs fabricated by photolithographic processes may not be the same as those in an actual porous electrode (which is typically fabricated by co-firing).

The specific TPB length in unit surface area was systematically controlled by adjusting the LSM to GDC volume ratio of the composite. To accomplish this, we fabricated a series of composite electrodes with different LSM/GDC volume ratios from 40% up to 70%. The TPB length for each tested samples was quantitatively determined. To estimate the amount of active TPB length in each sample a Monte Carlo simulation

was employed. The results and their implications will be outlined in the following sections.

Experimental

Preparation of dense GDC-LSM cathodes

The dense composite pellets with a two-layered structure of GDC/LSM-GDC were fabricated using a co-pressing and co-sintering method. LSM ($La_{0.85}Sr_{0.15}MnO_{3-\delta}$, from Rhodia, average particle size: 1.1 μm) and GDC ($Ce_{0.9}Gd_{0.1}O_{1.95}$, from Rhodia, average particle size: 0.3 μm) powders with various volume ratios ranging from 40:60 to 70:30 were heavily mixed in a mortar further reducing particle sizes.

The co-pressing consisted of several successive steps. First, the as-prepared mixture powder was added to a die (diameter of 10 mm) and tapped smooth using a pestle. Next, GDC powder was loaded into the die. Finally, the whole body was cold-pressed under 200 MPa into cylindrical pellets using a uniaxial die-press.

After firing the samples at 1450^{o}C for 5 hours in air, dense GDC/LSM-GDC wafers were obtained. The thicknesses of GDC and GDC-LSM composite were ~0.5 mm and ~0.15 mm, respectively. The sheet resistance of the as-prepared composite electrode ranged from 200-600 ohms (increasing with increasing GDC volume percentage) when measured directly by a multimeter at room temperature. The conductivity of LSM increases dramatically at measuring temperatures (>600^{o}C) and provides sufficient electronic conduction for current collection for electrochemical impedance measurement. Figure 3-1 and Figure 3-2 show scanning electron micrographs (SEM) of the bi-layer structure and the dense composite layer. After performing EDX characterization on numerous small particles, it was found that particles with a terrace structure on their

surface corresponded to LSM, while those with small dents on their surface corresponded to GDC. These surface differences were readily discernable in SEM micrographs. In this manner, the two phases were able to be differentiated.

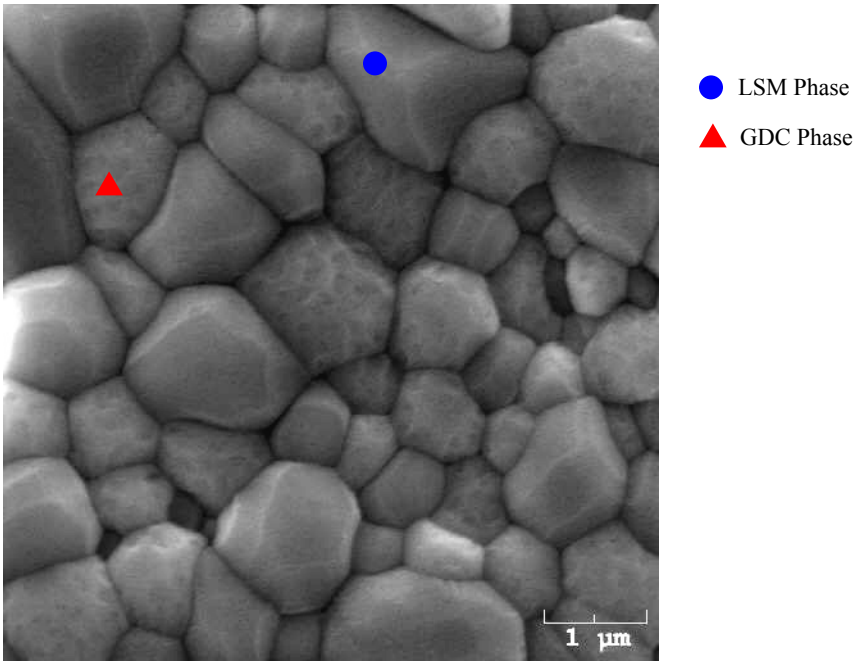

Figure 3-1. Scanning electron micrograph (SEM) of the dense composite GDC-LSM surface

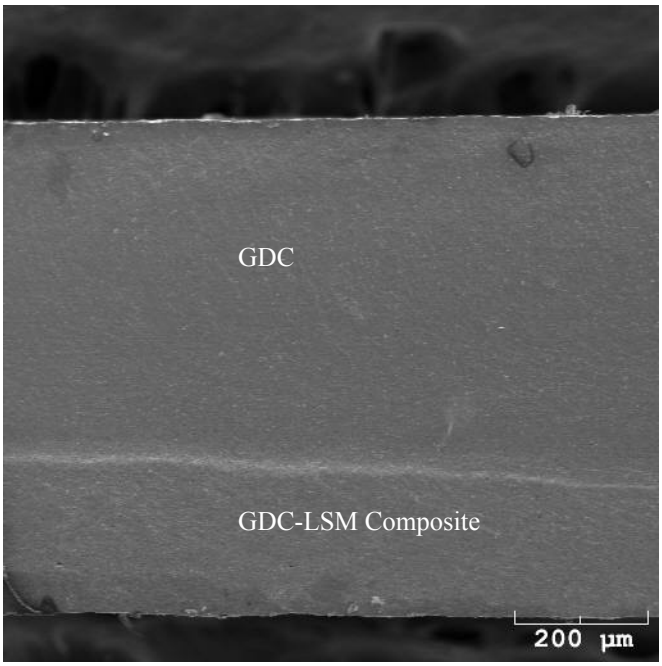

Figure 3-2. SEM side view of the bilayer structure showing the relative thicknesses of the dense GDC layer (top layer) and the dense GDC-LSM composite layer (bottom layer)

Phase stability of the composite was checked using x-ray diffraction (XRD). Unlike the dense LSM/YSZ composite, no apparent side reactions took place to any appreciable extent at the high fabrication temperature, thus no insulating phases were seen in the XRD pattern (see Figure 3-3 and Figure 3-4). For the LSM/YSZ system, in contrast, it is believed that a $La_2Zr_2O_7$ phase forms under the above fabrication conditions[80].

During the above fabrication phase, successive samples and subsequent SEM analysis showed that an electrode:electrolyte mass ratio of approximately 1:2 (varying slightly depending upon the volume percentage of GDC) produced bilayer structures with a minimum of curvature and good lamination to each other. Deviations from this ratio typically resulted in delamination or severe cracking in the bilayer.

For each sample, one of two methods was used for current collection. Either a painted silver (Haraeus C8710) counter electrode was applied to the GDC surface symmetrical to the composite layer. Contacting silver wire (dia. 0.25 mm) was attached to both surfaces for current collection. Or a platinum or gold mesh was compressed to the surface of the sample for current collection. Electrochemical impedance spectroscopy (EIS) using a Solartron system (1287 electrochemical interface, 1255 frequency response analyzer) was performed to test the performance of the cells.

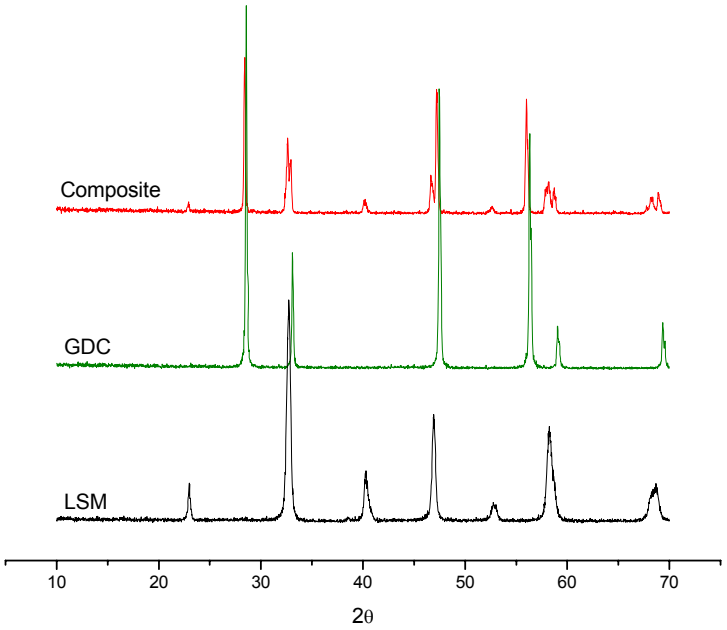

Figure 3-3. X-ray diffraction (XRD) pattern comparison for LSM, GDC, and a composite of the two showing no interacting phases produced during processing

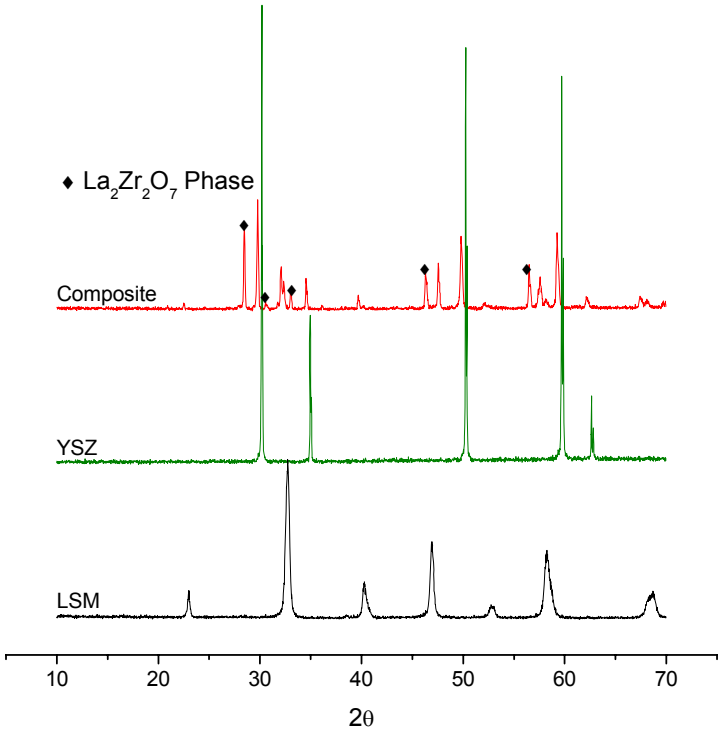

Figure 3-4. XRD pattern comparison for LSM, YSZ, and a composite of the two showing the insulating $La_2Zr_2O_7$ phase produced during processing

Stereological calculations of the composite microstructure

To quantify the TPB length for the various sample sets, established stereographic techniques were employed[81]. Micrographs of the sample surfaces were taken using SEM and test lines were overlaid on the image. Using the known magnification of the micrograph, the actual total length of the test lines was determined. The number of intersections between the test lines and the LSM-GDC grain boundaries (which represents a TPB line), P_L, was counted. This process was repeated at different locales on the surfaces of several samples for a minimum of thirty fields of view, and an average value of the number of intersections per test line, $\langle P_L \rangle$, was calculated. The average value of the total boundary length per unit area, $\langle L_A \rangle$, is related to $\langle P_L \rangle$ thru the simple expression shown in Equation (3.1):

$$\langle L_A \rangle = \frac{\pi}{2} \langle P_L \rangle \tag{3.1}$$

The lengths of triple phase boundary for the various composite compositions were determined directly from the value of $\langle L_A \rangle$, with the units of $\mu m/\mu m^2$.

Typically, these types of measurements are performed by commercial software for added expediency. However, these types of software packages could not be used for these images as the software algorithms rely on contrast between the various phases. The phases in the acquired SEM images can only be distinguished by particle features while the contrast between the particles is very low. Thus, all measurements had to be completed manually. The photo editing software package Adobe Photoshop® was used to overlay the test lines.

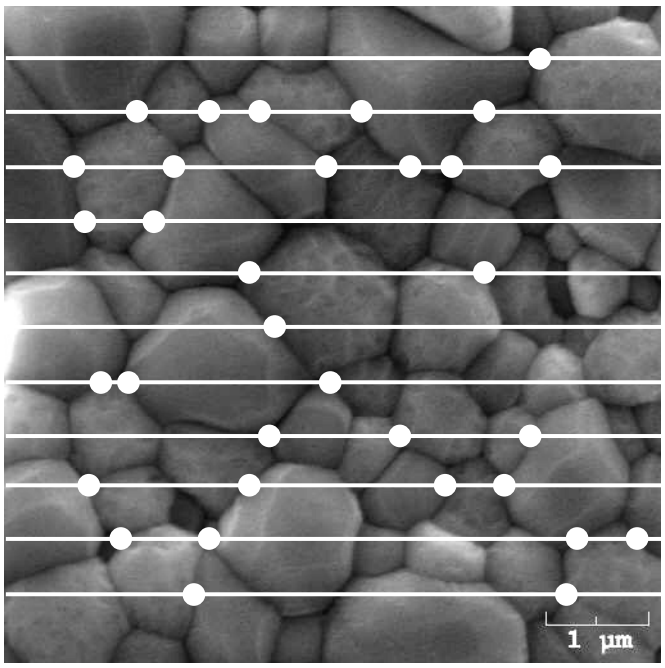

Figure 3-5. SEM of a composite surface showing an overlay of test lines used for stereological calculations. Areas of test line intersection with TPB points are circled.

Particle size of each phase was also estimated using a modified version of the method described in the ASTM Standard E 112-88. This article describes the lineal intercept method in general and the Heyn procedure in particular. To use this method for the composite material (two distinct phases) the same test line pattern used in the TPB calculation above was first overlaid on the SEM image. For each phase, the length of test lines falling within that phase was taken as the total length of test line, L_T. The number of grain intersections for that phase, P, were then counted and then the ratio of those two was taken as the grain size ($\bar{L}_A$) in units of microns. This is expressed as:

$$\bar{L}_A = \frac{L_T}{P} \tag{3.2}$$

Impedance spectroscopy measurements

The GDC/LSM–GDC samples were tested using impedance spectroscopy to quantify the cathode's performance. Silver wires were attached to each surface using Ag paste for current collection. The Ag wire on the GDC side was attached to the CE/RE2 connection of the Solartron 1287 while the LSM–GDC composite side was connected to the WE/RE1 connection. Isothermal impedance measurements were typically recorded for the frequency range of $1 \cdot 10^{6}$ – $5 \cdot 10^{-3}$ Hz with a signal amplitude of 10mV. Measurements were taken at 25°C increments from 650°C – 725°C. The cell configuration and wire connection is schematically shown in Figure 3-6.

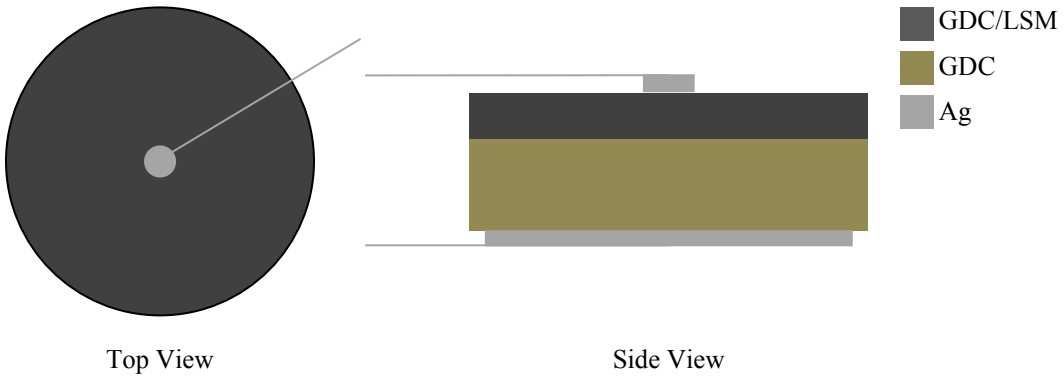

Figure 3-6. Schematic showing the top and side views of the testing setup. Silver paste was painted onto the electrode surfaces and used for current collection.

Additional testing apparatus

In addition to the above testing cell, another apparatus was also used to better control the atmosphere of the testing environment as well as provide better current collection from the sample.

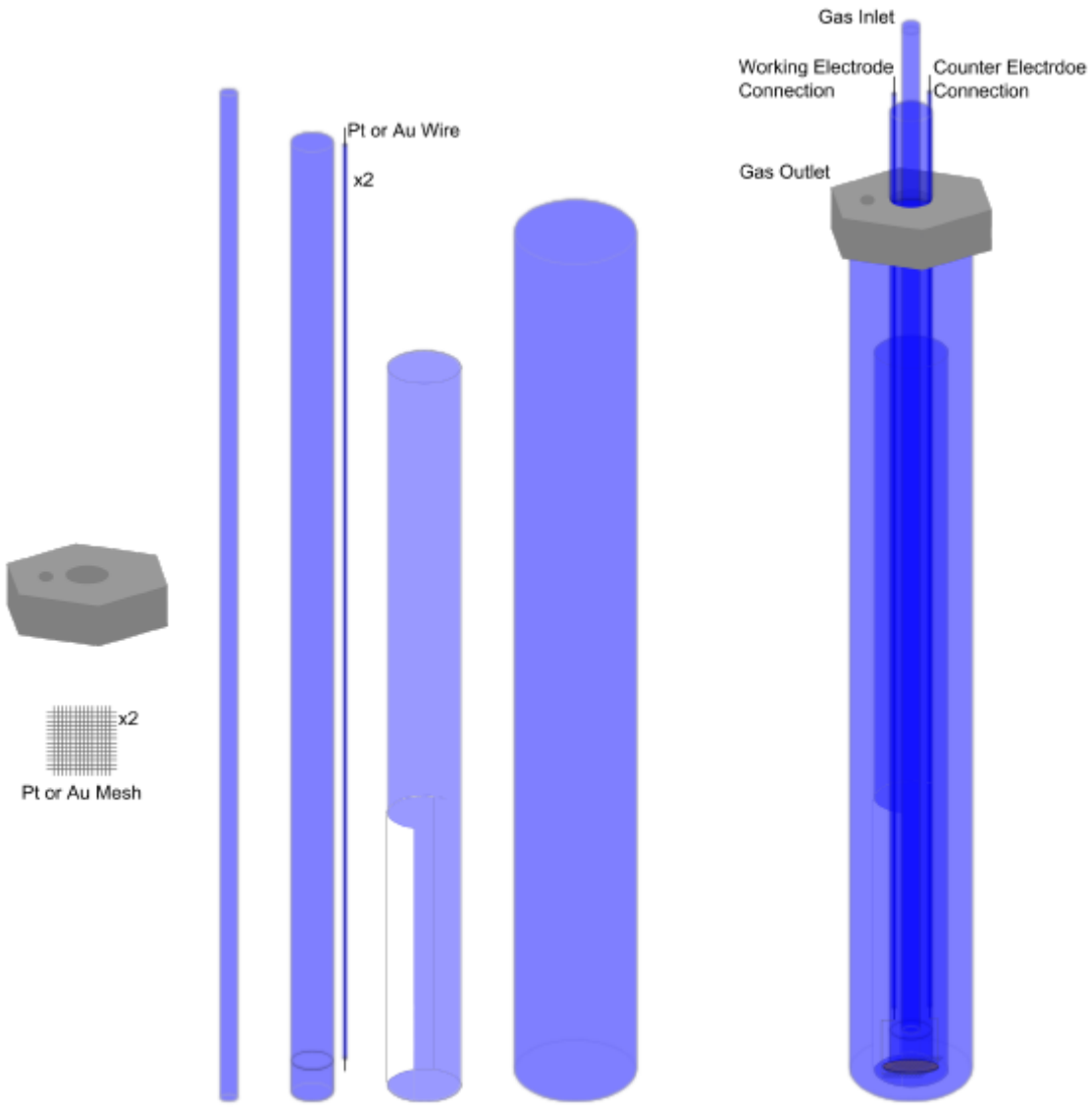

Figure 3-7. Quartz sample testing apparatus. The various components of the apparatus are shown on the left while the fully assembled testing setup is shown on the right. Pt or Au mesh and wire were used for the electrical connections to the sample. A glass frit above the sample allows for adequate gas flow to the sample surface

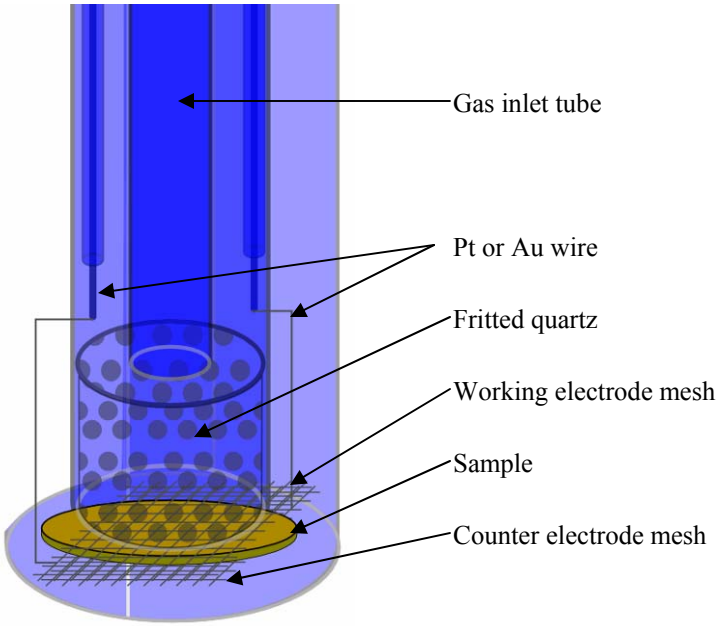

Figure 3-8. Close-up view of the bottom portion of the quartz testing setup showing the electrical connections between the sample and Pt/Au wire. Contact is maintained via compression from two springs (not shown).

The setup pictured in Figure 3-7 is composed primarily of quartz tubes and either platinum or gold mesh used for current collection. Moving from left to right in Figure 3-7, the first tube is the gas inlet tube. The next piece houses both the gas inlet tube and the electrical connection tubes. On the lower end of this tube is a piece of fritted quartz that allows for even gas distribution over the sample surface that sits adjacent to it. The next pieces are thin quartz tubes that house Pt or Au wire. Each wire connects to a mesh of the same metal sitting on opposite sides of the sample used for current collection from the working electrode and the counter electrode, respectively (see Figure 3-8). The next tube provides both an access window through which the sample can be changed and a bottom support for the counter electrode side of the sample. The metal mesh maintains its contact with the sample through a compressive force from two springs (not shown) connected to both the fritted tube and the access window tube. The final quartz tube

houses the internal setup and contains the atmosphere for the test. The entire assembled setup is shown on the right side of Figure 3-7.

Using the above setup, current collection from the entire sample surface is ensured through contact with a metal mesh. Additionally, the smaller volume inside the quartz tubes (as opposed to relatively large volume of the tube furnace) allows for much more precise atmosphere control. The sample geometry was also modified from that shown in Figure 3-6 in that no Ag paste was applied to the sample and a painted LSM counter electrode was used in place of the painted Ag paste.

Testing parameters for the EIS experiments were similar to those used in the previous testing setup and are summarized in Table 3-1. The second setup allowed for a larger temperature range for the measurements due to using the platinum mesh for current collection that had a much higher melting point than the silver wire/silver paste combination. Additional studies, such as effect of applied overpotential (DC bias) were also performed with the second apparatus that were not able to be completed using the first one for reasons explained in the results section of this chapter.

Table 3-1. Experimental parameters and measurement ranges for EIS measurements

Experimental Parameter	**Measurement Range**
Temperature	650°C – 750°C (25°C increments)
Oxygen Partial Pressure	100% P_{O2} 23% P_{O2} 1% P_{O2} 0.1% P_{O2}
Overpotential	0.000V – 0.300V (0.075V increments)
Frequency Range	$1 \cdot 10^{6}$ – $5 \cdot 10^{-3}$ Hz (6 points per decade)

Experimental TPB Measurement Results

The change in length of TPB for various volume percentages of LSM are shown in Figure 3-9 below. A maximum in TPB length was witnessed for the 50 volume percentage of LSM samples. This is the expected result because for a given particle size and perfectly random mixture, the TPB length should be maximized when the volume percentages are equal. Deviations from a 50-50 mixture would result in more like particles being adjacent to each other, thus lowering the overall TPB length of the sample. The curve is asymmetric about the maximum point. Better symmetry would be expected if the other parameters such as grain size of the two phases were more consistent.

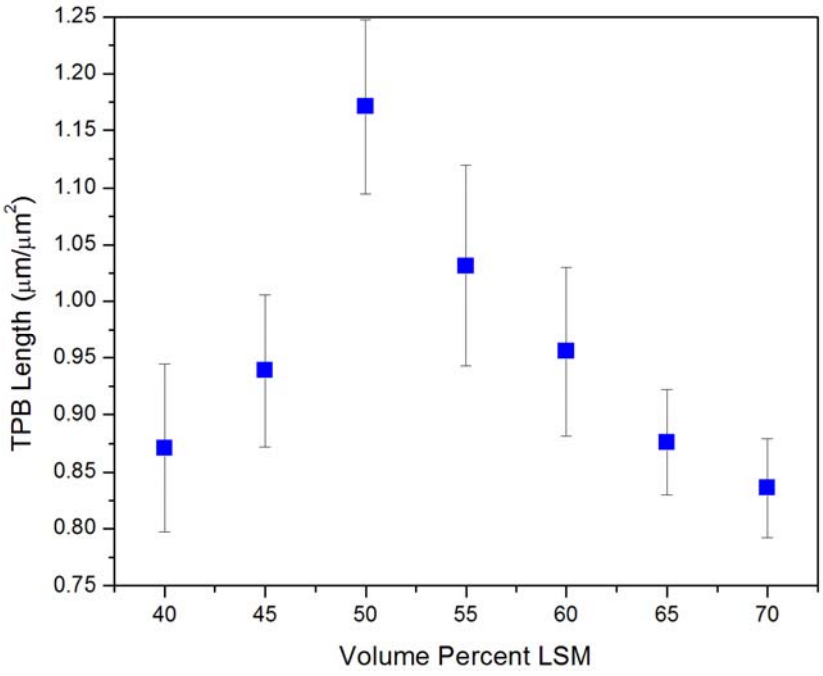

Figure 3-9. Change in TPB length with volume percentage of LSM for the dense composite electrode

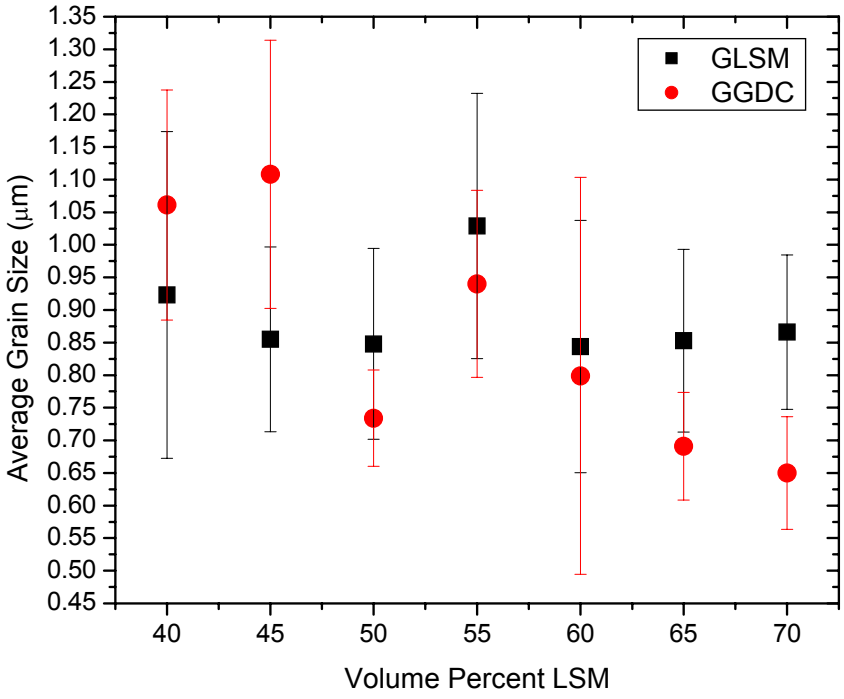

Figure 3-10. Change in average grain size with volume percentage of LSM for both the LSM (square) and GDC (circle) phases. The error bars show the uncertantiy in the calculation which gives a measure to particle size distribution for particular volume percentage.

Figure 3-10 shows the change in the average grain size of both the LSM and GDC particles in the composite layer for the varying sample sets (note the axes do not start at zero). Particle size was determined using the mean lineal intercept method described in the ASTM Standard E 112-88. The LSM particle size remained relatively constant except for the 55 volume percentage samples, while the particle size for the GDC continuously decreased with increasing LSM volume percentage, except for the 50 volume percent samples. The decrease in GDC particle size was most likely due to slower growth after sintering stemming from the increasing number of LSM particles. More consistency in grain size could be controlled by varying the firing schedule to allow more or less growth of the GDC particles.

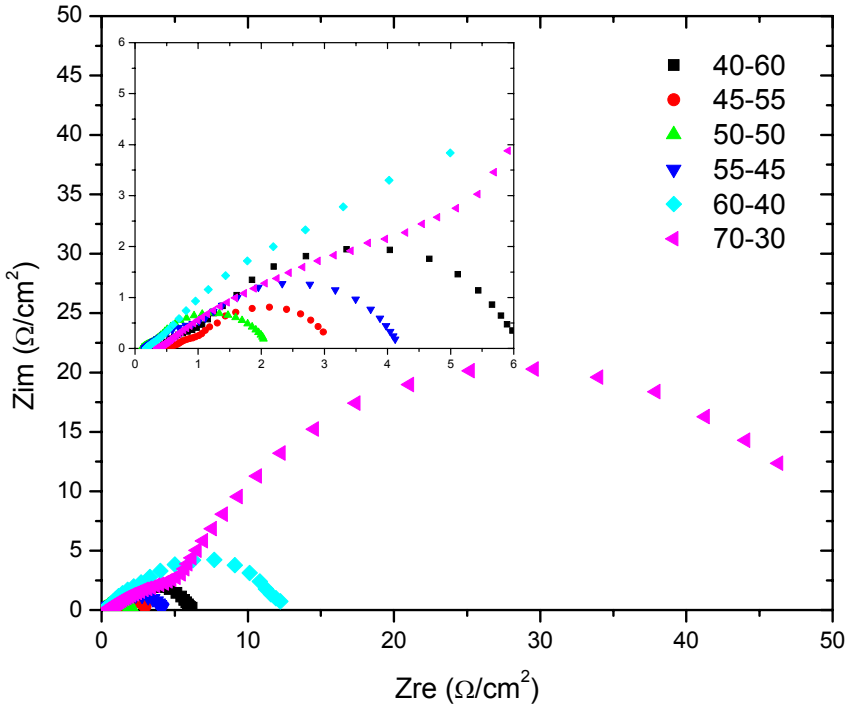

Figure 3-11. Typical impedance spectra obtained for the various volume percentages of 40:60 through 70:30 (LSM:GDC) at 725°C. The above data was collected using first mentioned testing setup and is scaled by the area of the Ag current collector.

Shown in Figure 3-11 are the typical Nyquist plot impedance spectra obtained for the various volume percentages of LSM. The inset shows the lower range in greater detail. The polarization resistance, a measure of the cell's performance was garnered from the impedance data by taking the difference between the low frequency intercept with the real axis and that of high frequency intercept with the real axis. Figure 3-12 shows a plot of inverse area specific polarization resistance versus total TPB length. The plot is expected to be linear but shows significant scatter, specifically from the low volume percentages of LSM samples. The main cause of this nonlinearity is most likely due to not all of the TPB lines for each sample being active. For the TPB around each LSM particle to be considered active, it must contact a GDC particle that is part of a percolating cluster through the composite electrode to electrolyte. The likelihood of

percolation for the GDC particles becomes increasingly smaller as the volume percentage of LSM increases. It is expected that once phase percolation is taken into account and the amount of active TPB length is calculated, better linearity will be achieved.

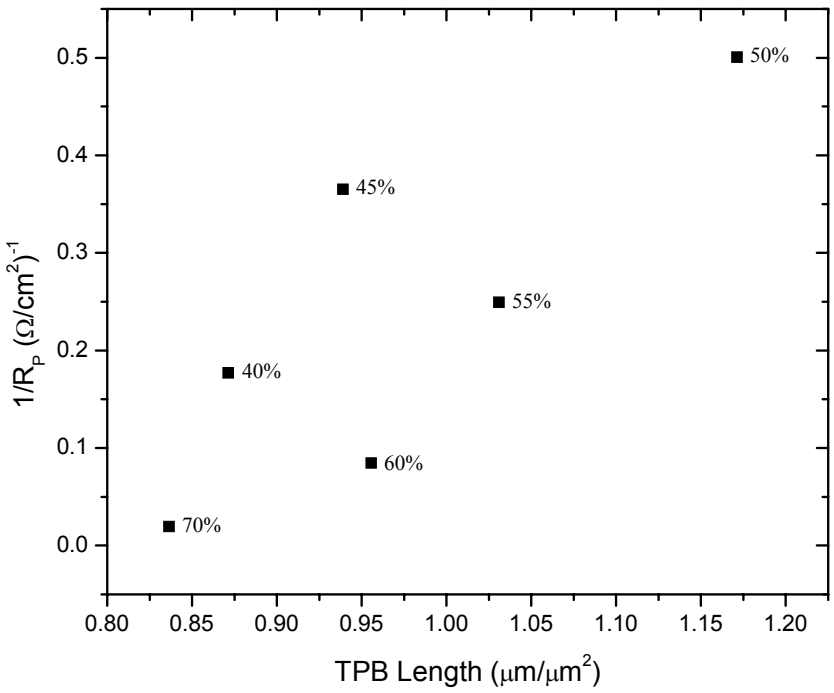

Figure 3-12. Plot of inverse area specific polarization resistance ($1/\overline{R}_P$) versus TPB length. The number to the right of each data point represents the LSM volume percentage for those samples

Investigation of Phase Percolation

As mentioned in the previous section, percolation was suspected to play a major role in the performance of the composite layers. Figure 3-13 demonstrates the role that percolation plays in determining the activity of a TPB line. The figure shows a sample random 2-D slice of a fictional microstructure. Assuming that the top surface represents the exposed dense composite electrode, there are three GDC clusters helping to form five points of TPB line (circled in the picture). As can be seen in the image, only through the

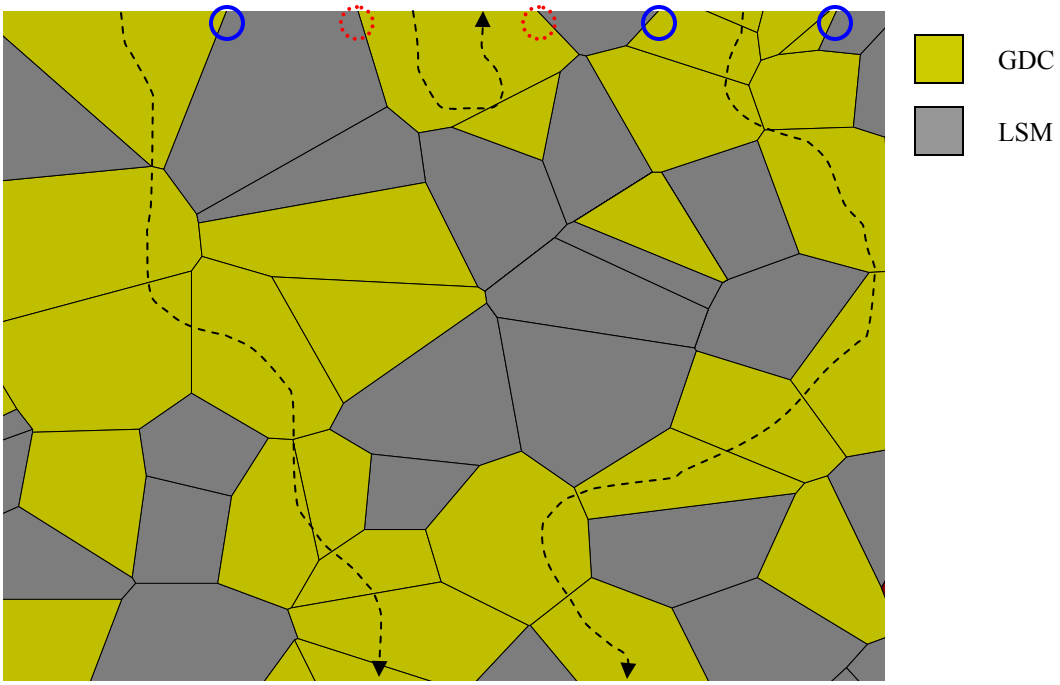

Figure 3-13. Sample 2-D random microstructure showing percolating (solid outlined circles) and non-percolating TPB points (dashed circles). The dashed lines further illustrate possible paths that incorporated oxygen may traverse to reach the electrolyte layer. Grain geometry is not indicative of actual grain geometry, but used for demonstration purposes only.

leftmost and the rightmost clusters can one traverse a continuous non-interrupted path from the top surface to the bottom surface (which is in contact with the GDC electrolyte). These two clusters are considered part of a percolating cluster. The middle cluster, on the other hand, is isolated from the electrolyte layer. This isolation essentially renders the TPB points it produces (dashed line circles) inactive because any oxygen incorporated into the lattice at those points is trapped and has no recourse but to desorb back to the surface. The above illustration ignores any effects of a three-dimensional network.

Percolation model description

To obtain a more complete picture of the composite systems under study and to make the systems more readily comparable, percolation simulations were developed to

estimate the percentage of the surface TPB lines that are actually part of a percolating GDC cluster. An overlapping spheres model was used to represent the GDC phase. The volume space outside of the spheres was assumed to belong to the LSM phase. Thus, throughout the sample space, two distinct phases were identifiable and used to represent the dense composite. The spheres were continuously placed at random positions in the sample space volume until the desired volume fraction was reached. A simplified Monte Carlo simulation was used to determine the volume fraction in the sample space. Random points in space were tested for whether or not they resided inside the volume of a particle. If so, then a hit was recorded. The volume percentage was determined from the ratio of hits to total test points. The number of test points was chosen so that the calculated volume percentage was within a tolerance of $1 \cdot 10^{-5}$. Typically, this was around 10^6 test points. Simulations were run on a Windows XP workstation powered by dual AMD Operteron 248 processors (running at 2.19 GHz) and 3GB of RAM. All simulation code was written in the C++ programming language. A description of the program and its specific functions is given in Appendix A.

Initially, a specific number of particles and their corresponding radii were calculated and these two numbers determined the sample space volume for a given volume percentage. These particles were then randomly placed inside the sample space and the Monte Carlo volume fraction simulation was performed on the whole sample space. Due to allowable particle overlap, the total occupied volume was invariably less than the target volume. Particles were then added singly until the target volume was attained. Before the addition of each particle another Monte Carlo volume fraction simulation was performed on the space for the potential new particle position. Using this

information, the amount of added volume to the total sample space from the additional particle was able to be calculated.

The model also included several tunable parameters including: the number of particles, the average particle radius, the distribution of particle radii, the target volume percentage, and the amount of allowable overlap for each particle. The number of particles was chosen to be large enough to minimize large fluctuations between disparate simulations. The minimum number of particles used was 5000, but the typical simulation contained over 10,000 particles. During the study of the effect of particle size on percolation where the sample space was kept constant while the particle radii were varied, simulations including well over 100,000 particles were needed to obtain the high volume percentages. The effect of average particle radius was tested for particles ranging in radius from 1 to 4 units in steps of 0.5 units. Again, for this test, the sample space was kept constant and the changing parameter was essentially the ratio of average particle radius to the sample space parameter L_0 (where L_0 is the length of one side of the cubic sample space).

The model also allowed for various particle radii distributions. Monodisperse, bidisperse and log-normal distributions were all configurable. The log-normal distribution was calculated using the Box-Muller method for log-normal distributions first developed by George Edward Pelham Box and Mervin Edgar Muller[82]. This method generates pairs of independent normally distributed random numbers from a source of uniformly distributed random numbers. Assuming the mean, μ, and the standard deviation, σ, are defined, and using pairs of random numbers, x_1 and x_2, from a

uniform distribution between 0 and 1, a particle radius, *r*, that is part of a log-normal distribution was serially calculated from:

$$r = \sqrt{-2\log\left(x_1\right)} \tag{3.3}$$

$$r = r \cdot \sin\left(2\pi x_2\right) \tag{3.4}$$

$$r = \log\left(\mu\right) - \frac{1}{2}\log\left(1 + \frac{\sigma^2}{\mu^2}\right) + r\sqrt{\log\left(1 + \frac{\sigma^2}{\mu^2}\right)} \tag{3.5}$$

$$r = e^r \tag{3.6}$$

These calculations were repeated for each particle in the system. To test the robustness of the above algorithm, histograms were produced for an average particle size of 1.0 and values of σ equal to 0.00, 0.05, 0.15, and 0.25. These histograms are presented in Figure 3-14.

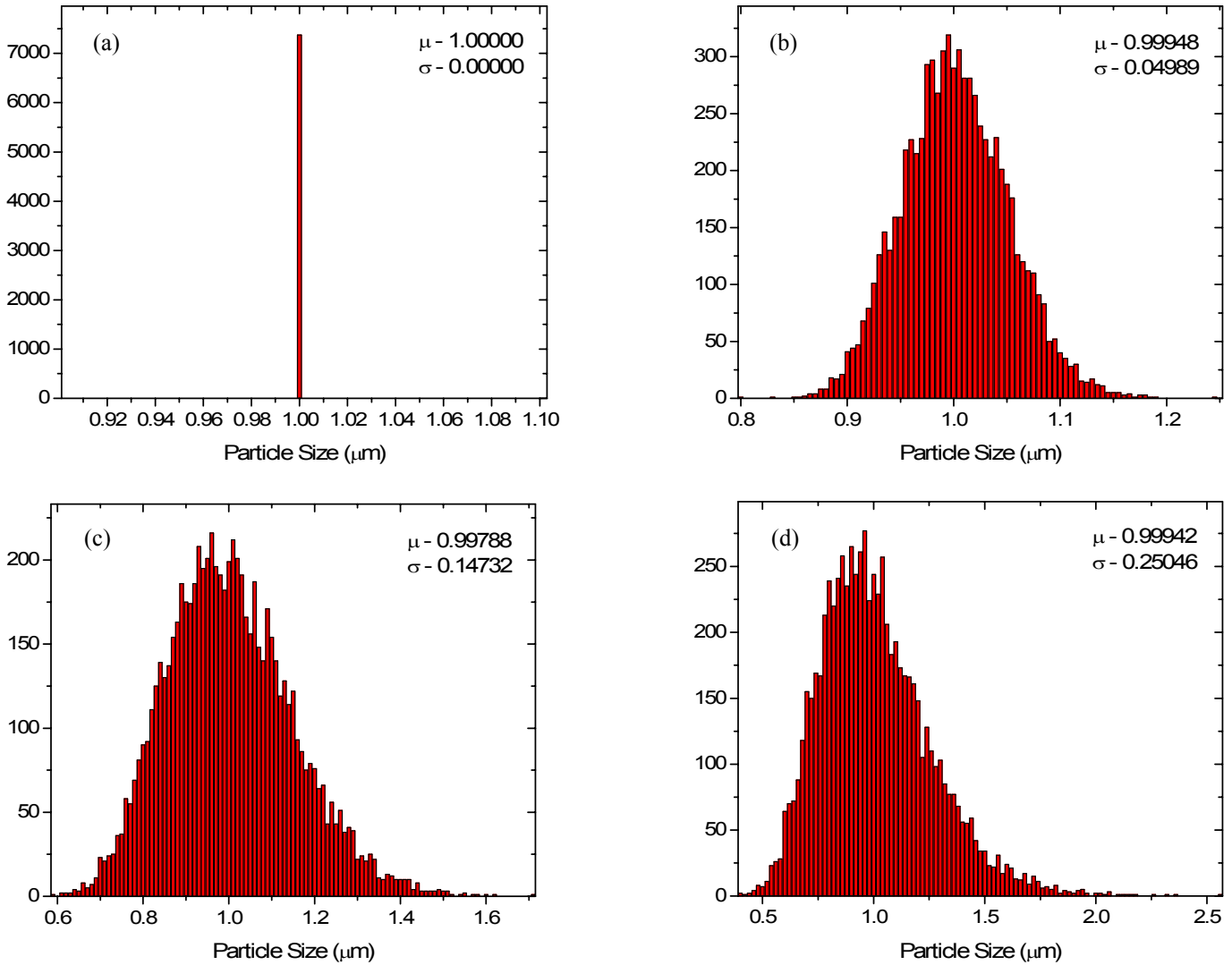

Figure 3-14. Histograms showing effect of variation in σ from (a) 0.00, (b) 0.05, (c) 0.15 and (d) 0.25

Variation of the volume percentage was the main thrust for the percolation simulations. The volume percentage was varied from 30% GDC to 70% GDC. A greater number of points were typically simulated close to 30% and between 50 and 60%. This was done to achieve a greater level of detail around the points of interest: the onset of percolation and the volume percentage above which negative returns in TPB length were achieved.

The last input parameter was the amount of allowable overlap between particles. This parameter gave the percentage of the particle radius below which no interpenetration from another particle was allowed. Setting this parameter to 0.0 caused the model be a fully overlapping spheres model, while setting it to 1.0 changed the model to a hard sphere model (see Figure 3-15). Variation in this parameter allowed the model, to a first approximation, to simulate the sintering effect their real world counterparts experienced. Typical values ranged from 0.0 to 0.7.

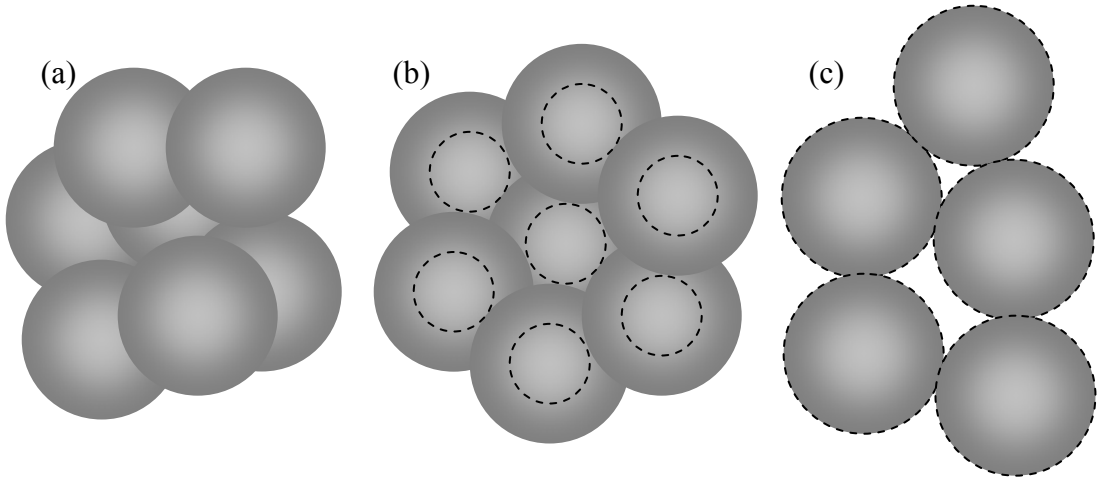

Figure 3-15. Effect of the overlap parameter, σ_c, as it varies from (a) 0.0, to (b) $0 \leq \sigma_c \leq 1.0$, to (c) 1.0

Cluster labeling and an efficient cluster counting algorithm are an essential part of the simulation. Several authors have developed very robust means for attacking this problem for both regular and random lattices[83-85]. These methods typically made use of two registers to keep track of both the labels and labels of the labels. The method used in this simulation was a simplified version of the Hoshen-Kopelman algorithm and required a two-pass counting scheme. Some authors have considered particles touching if they were within a certain distance from each other[84]. In this simulation, however, particles were considered to be touching if the distance between their centers was less than or equal to the sum of their radii. As other authors have done[86, 87], a particle was considered on a surface if it lied within a boundary region of the surface (see Figure 3-16). The thickness of the boundary region was determined by the average particle size in the simulation.

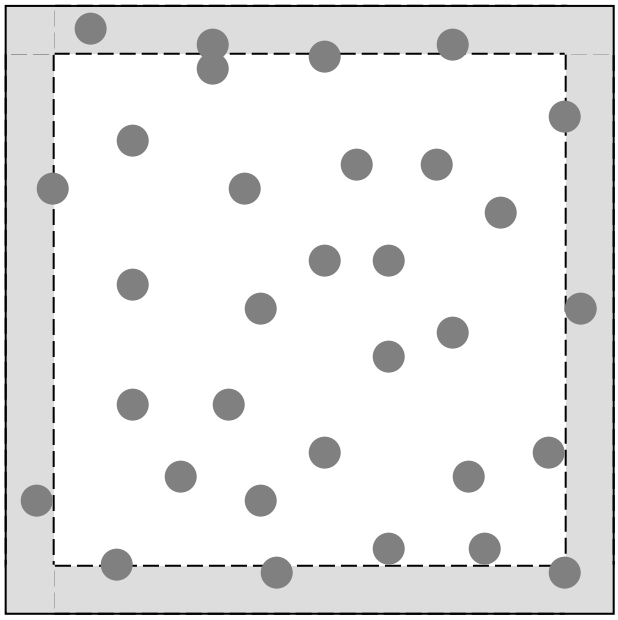

Figure 3-16. Sample space showing the boundary region (grey) that a particle must inhabit to be considered part of the surface. For a cluster to be considered percolating, particles in that cluster must lie in boundary regions on opposite sides.

Percolation simulation results

Below in Figure 3-17 through Figure 3-24 are select 3-D and 2-D cross-sectional views of the simulation space output. The images were produced using Matlab v7.0.4. Due to memory limitations only subsections of the total space are presented for some of the 3-D figures, however, the effect for each parameter is clearly shown. Variation is shown for the following parameters: average particle radius, μ, standard deviation of particle radii, σ, particle overlap, σ_c, and volume fraction of GDC, ϕ_{GDC}.

The images serve as a check to the simulation to ensure that properties of the simulation were changing as expected. It is clearly shown in Figure 3-17 and Figure 3-18 that as the average particle radius increases for a given volume fraction of GDC, the number of particles must decrease. In Figure 3-21 and Figure 3-22 as σ_c is increased the amount of overlap between particles is decreased and thus we see less overall particles and more spherical particles as simulation approaches the hard sphere model. As the hard sphere limitation is approached, the amount of surface area per volume (or perimeter per area) that each particle adds to the simulation space increases, and thus we expect to see less and less of a symmetric curve as in Figure 3-9 and more of a linear relationship.

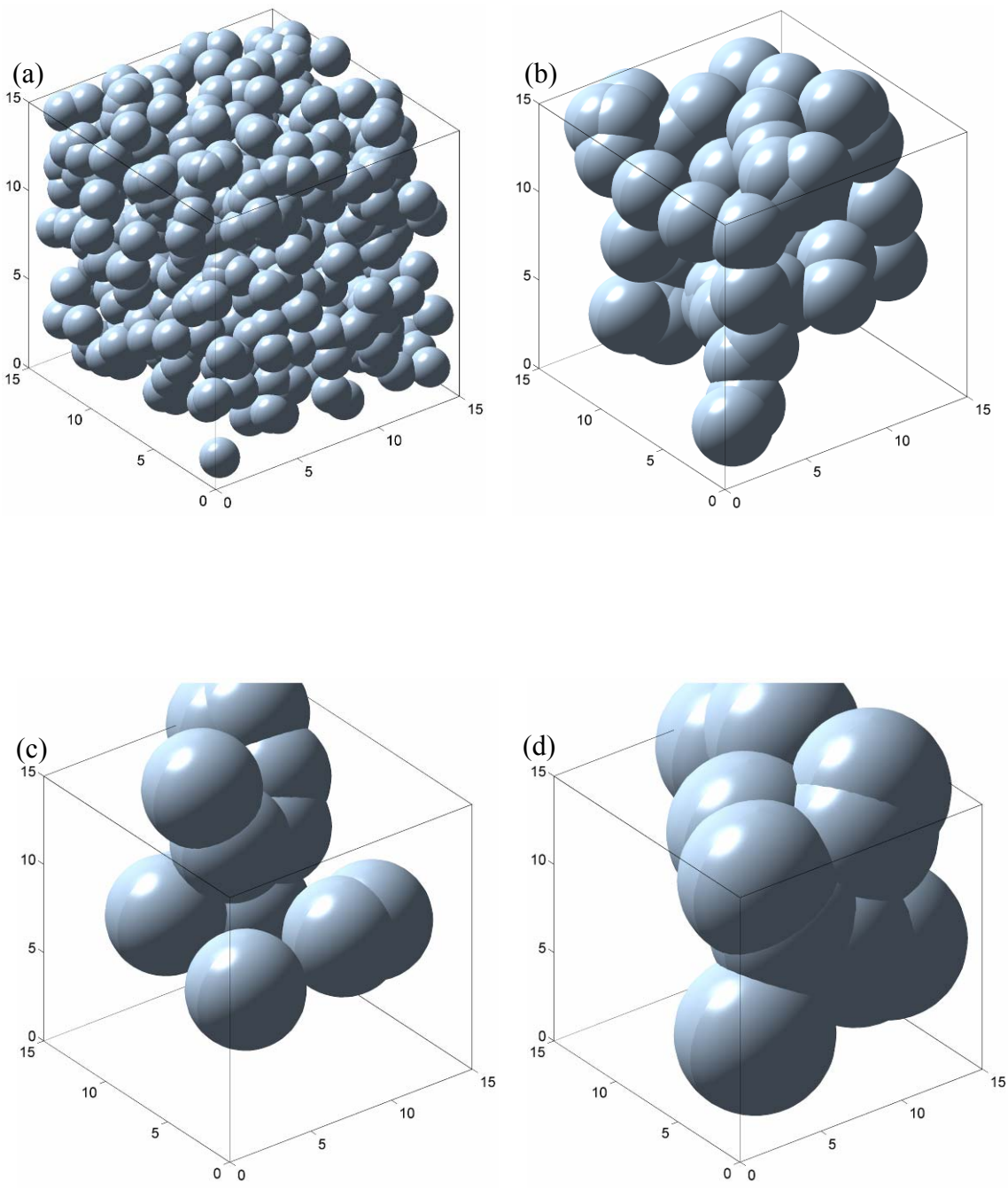

Figure 3-17. Percolation simulation results showing 3-D spatial changes as the average particle radius, μ, varies from (a) 1.0, to (b) 2.0, to (c) 3.0 and to (d) 4.0. Particle radius standard deviation and particle overlap parameters were both set to zero (monodisperse particles and complete overlap allowed).

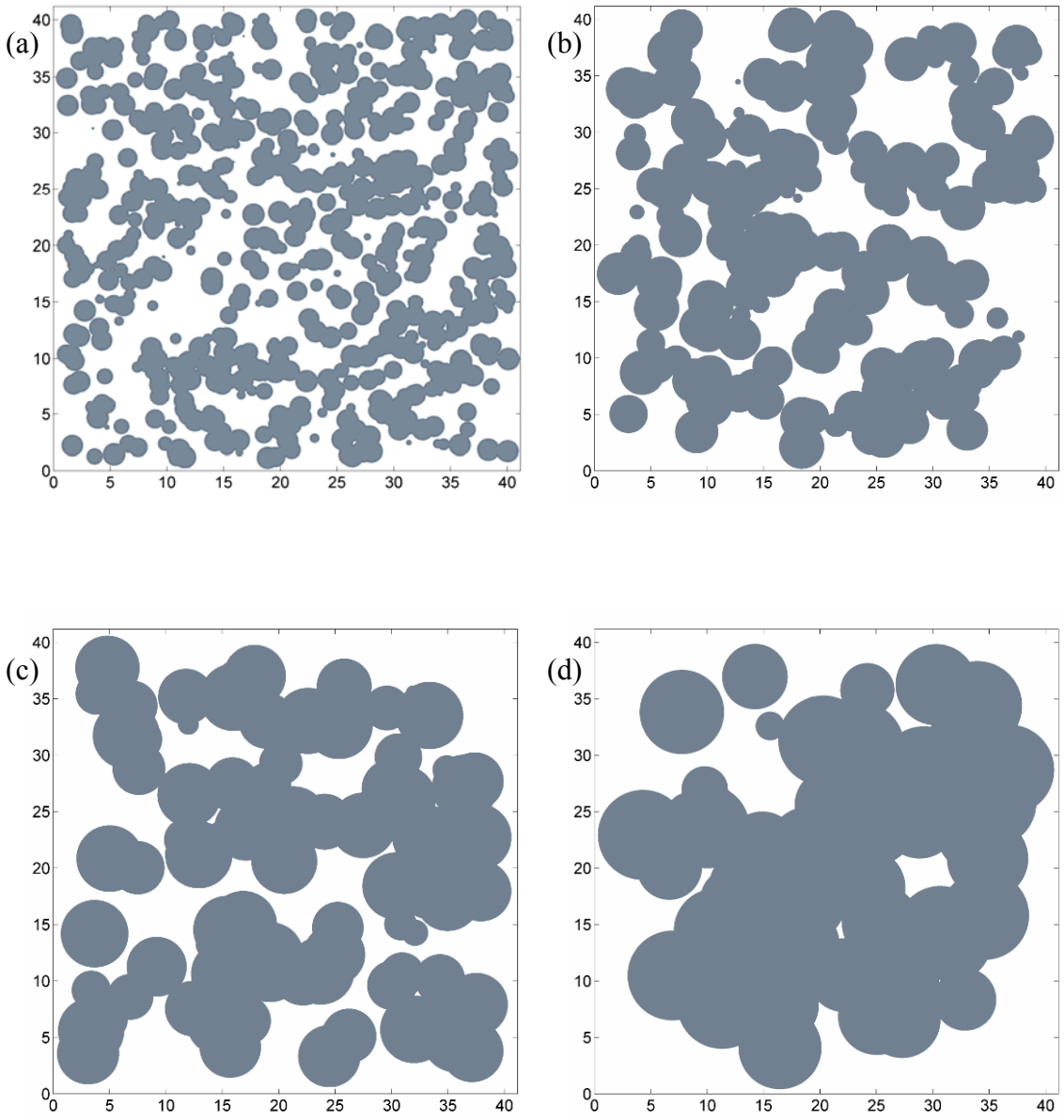

Figure 3-18. Percolation simulation results showing 2-D cross-sectional spatial changes as the average particle radius, μ, varies from (a) 1.0, to (b) 2.0, to (c) 3.0 and to (d) 4.0. Particle radius standard deviation and particle overlap parameters were both set to zero (monodisperse particles and complete overlap allowed).

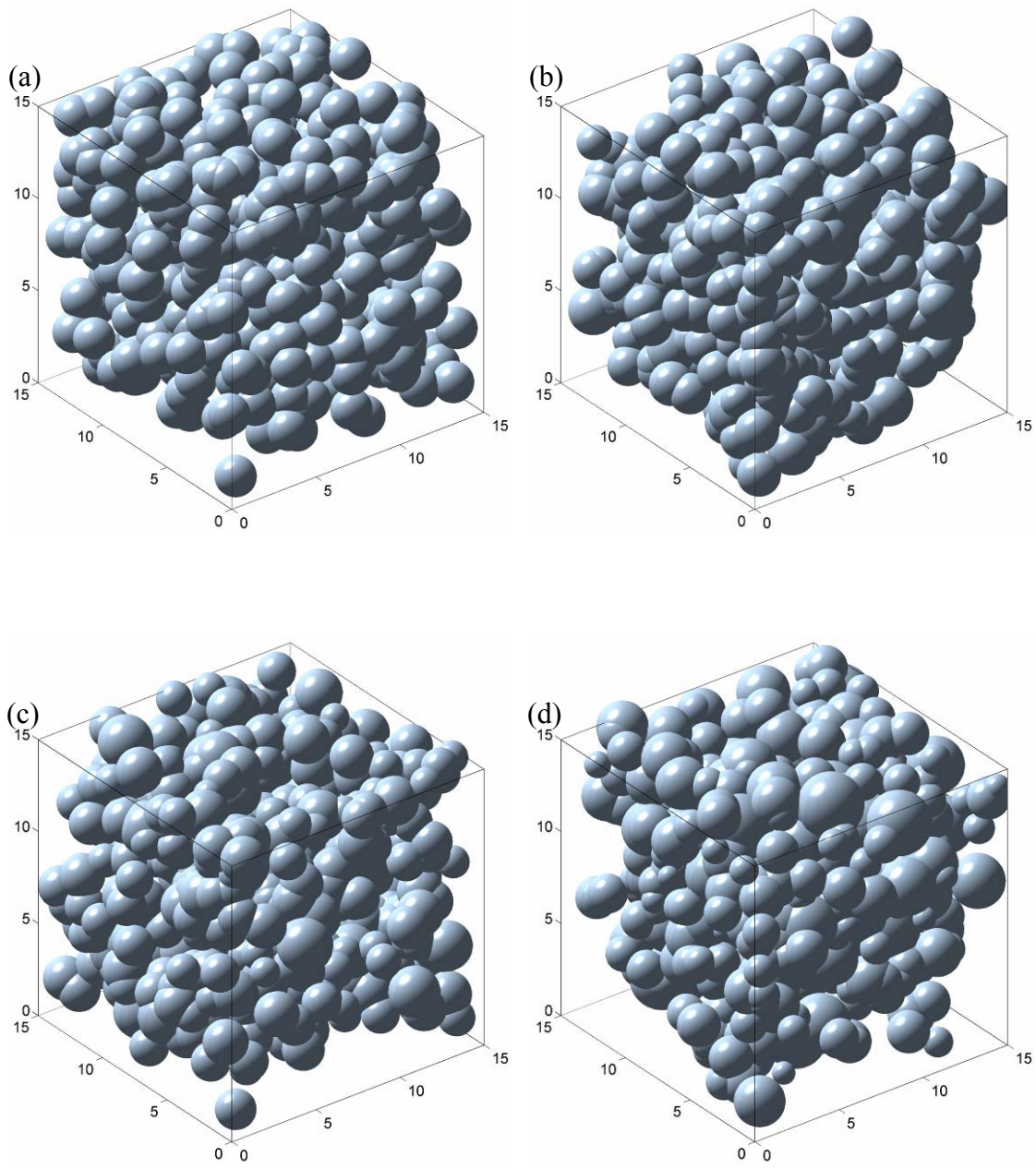

Figure 3-19. Percolation simulation results showing 3-D spatial changes as the particle radius standard deviation, σ, varies from (a) 0.00, to (b) 0.10, to (c) 0.15 and to (d) 0.25. Particle radius was set to 1.0 and the particle overlap was set to zero (complete overlap allowed).

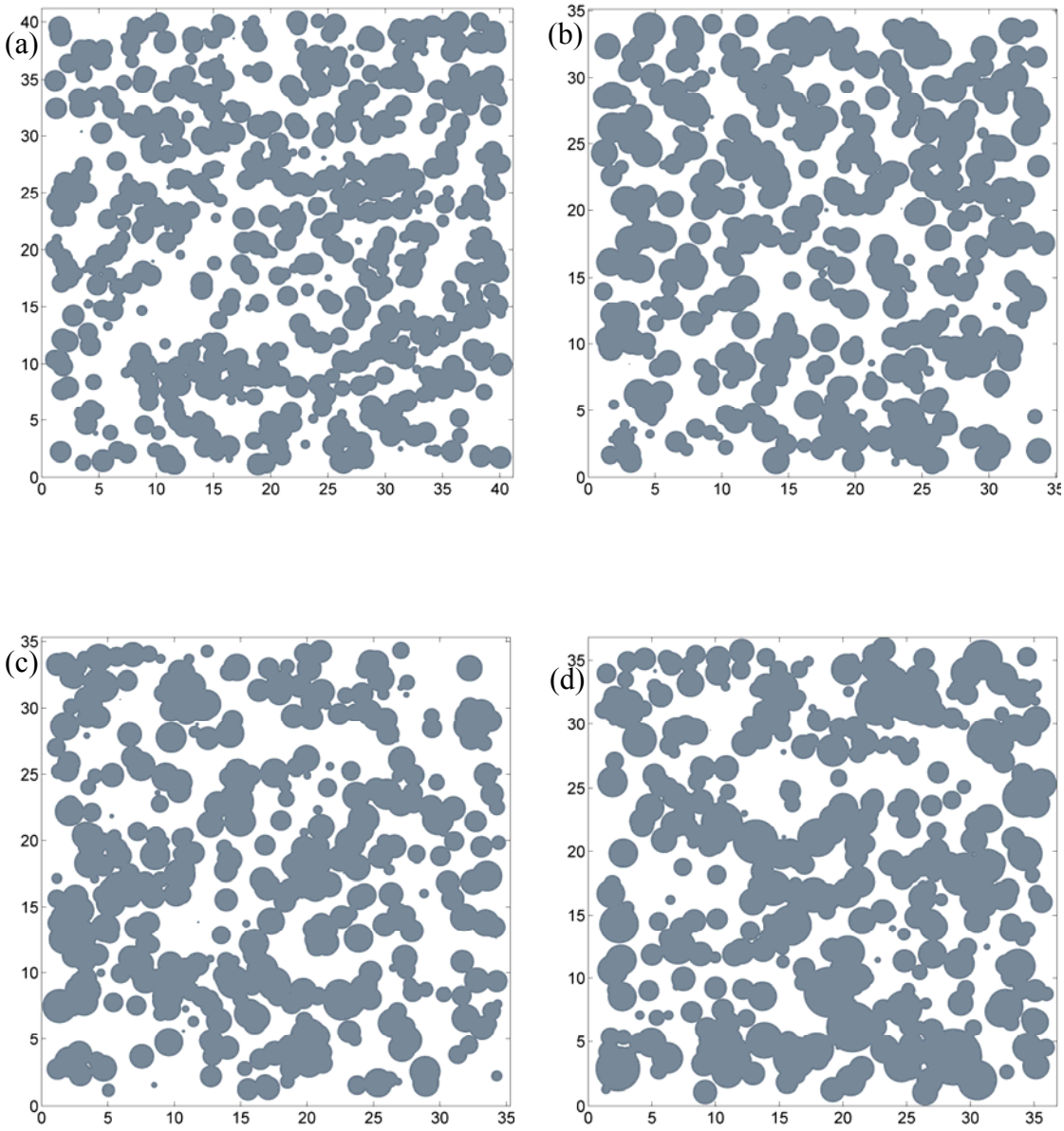

Figure 3-20. Percolation simulation results showing 2-D cross-sectional spatial changes as the particle radius standard deviation, σ, varies from (a) 0.00, to (b) 0.10, to (c) 0.15 and to (d) 0.25. Particle radius was set to 1.0 and the particle overlap was set to zero (complete overlap allowed).

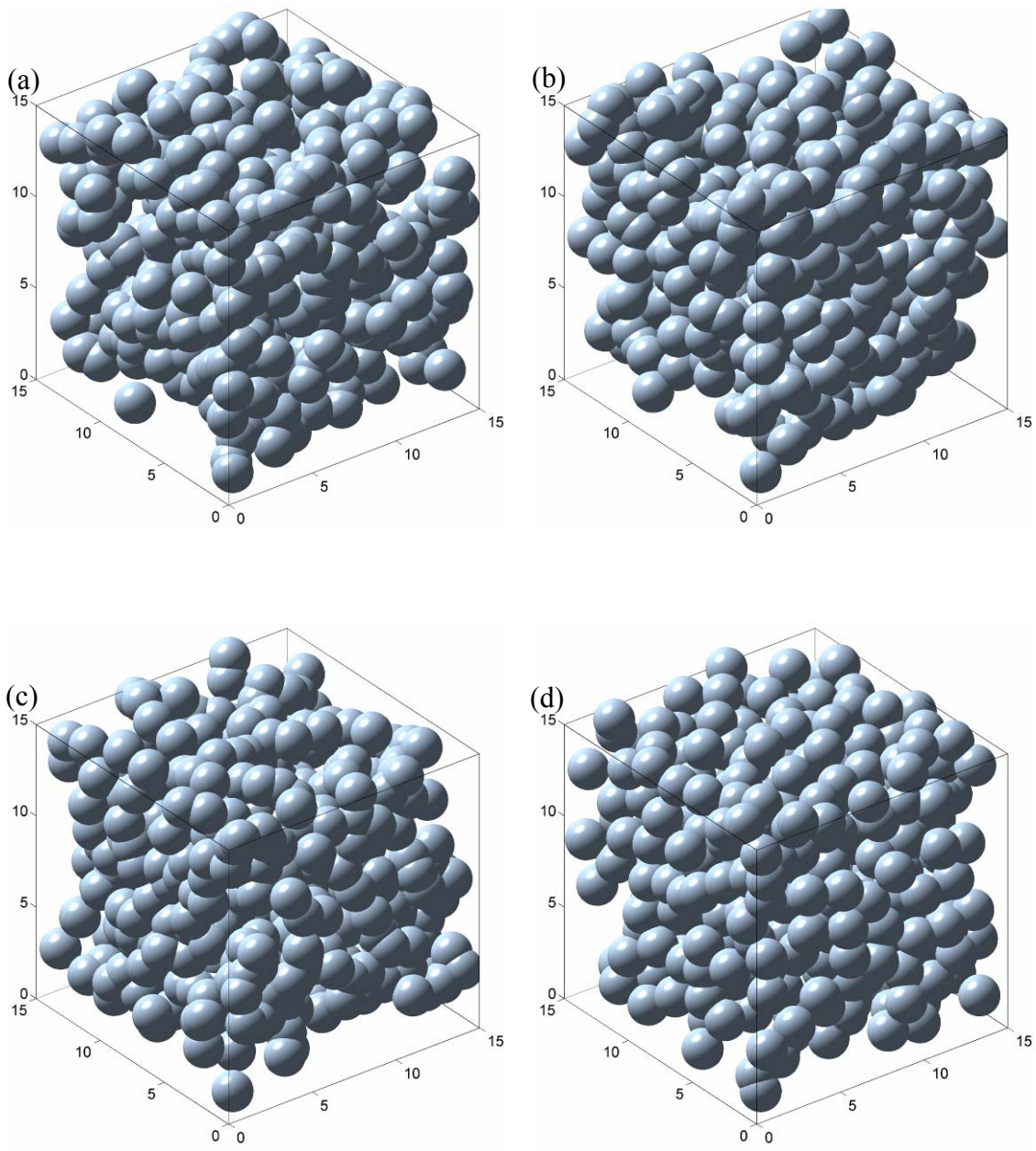

Figure 3-21. Percolation simulation results showing 3-D spatial changes as the amount of particle overlap, σ_c, varies from (a) 0.00, to (b) 0.20, to (c) 0.40 and to (d) 0.70. Particle radius was set to 1.0 and its standard deviation was set to zero.

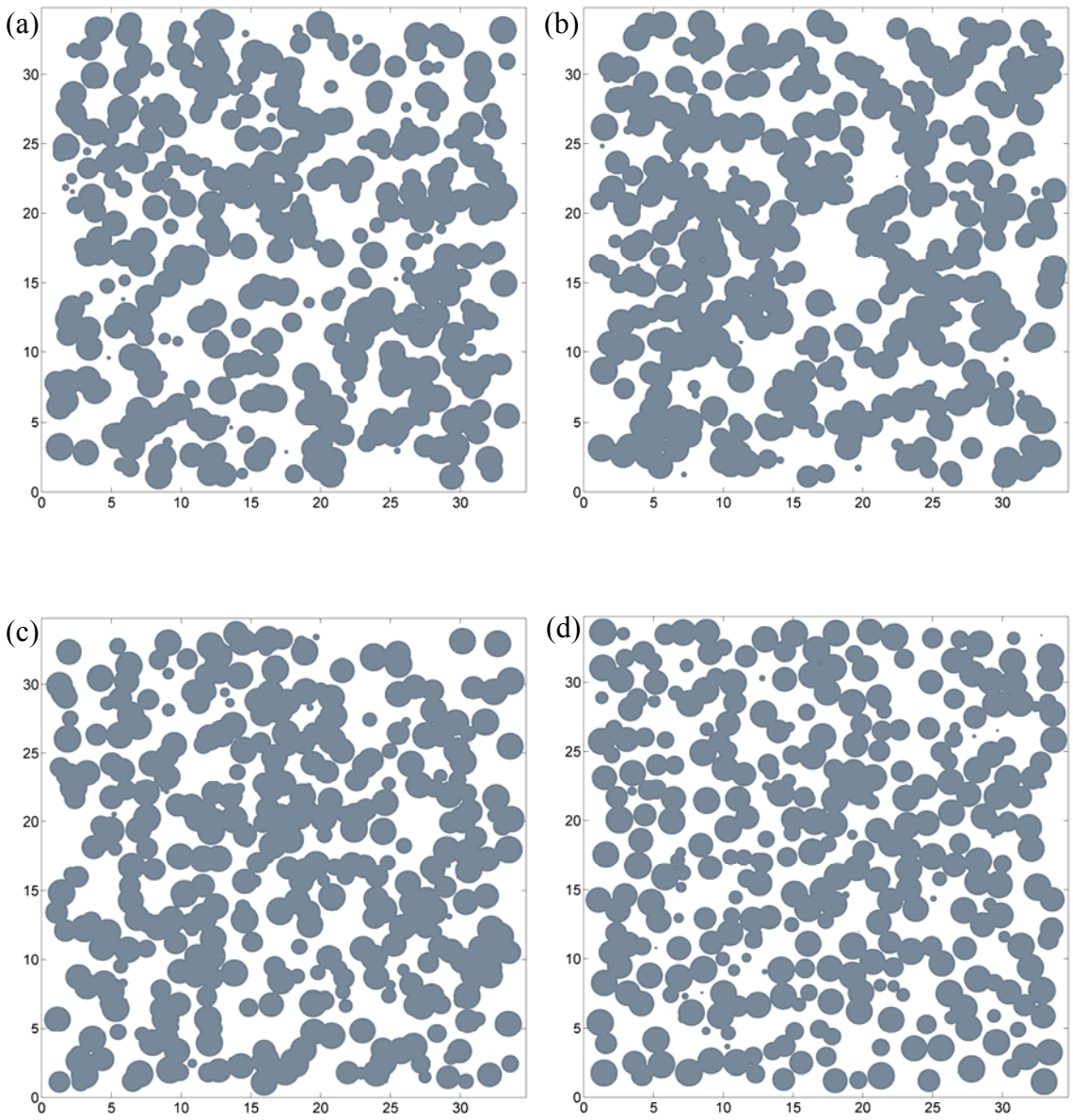

Figure 3-22. Percolation simulation results showing 2-D cross-sectional spatial changes as the amount of particle overlap, σ_c, varies from (a) 0.00, to (b) 0.20, to (c) 0.40 and to (d) 0.70. Particle radius was set to 1.0 and its standard deviation was set to zero.

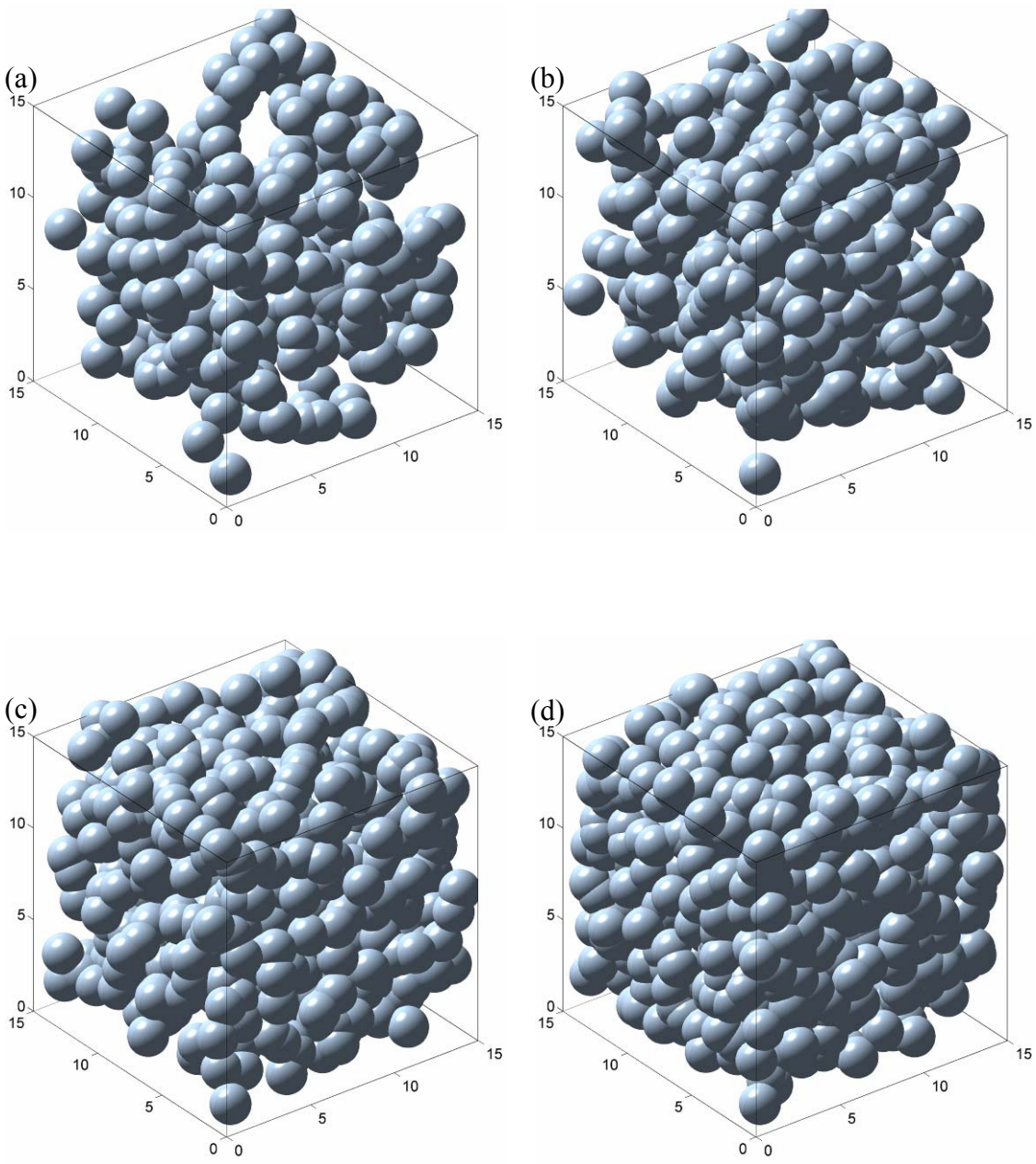

Figure 3-23. Percolation simulation results showing 3-D spatial changes as the volume fraction of GDC, ϕ_{GDC}, varies from (a) 0.30, to (b) 0.425, to (c) 0.55 and to (d) 0.70. Particle radius was set to 1.0, particle radius standard deviation and particle overlap parameters were both set to zero (monodisperse particles and complete overlap allowed).

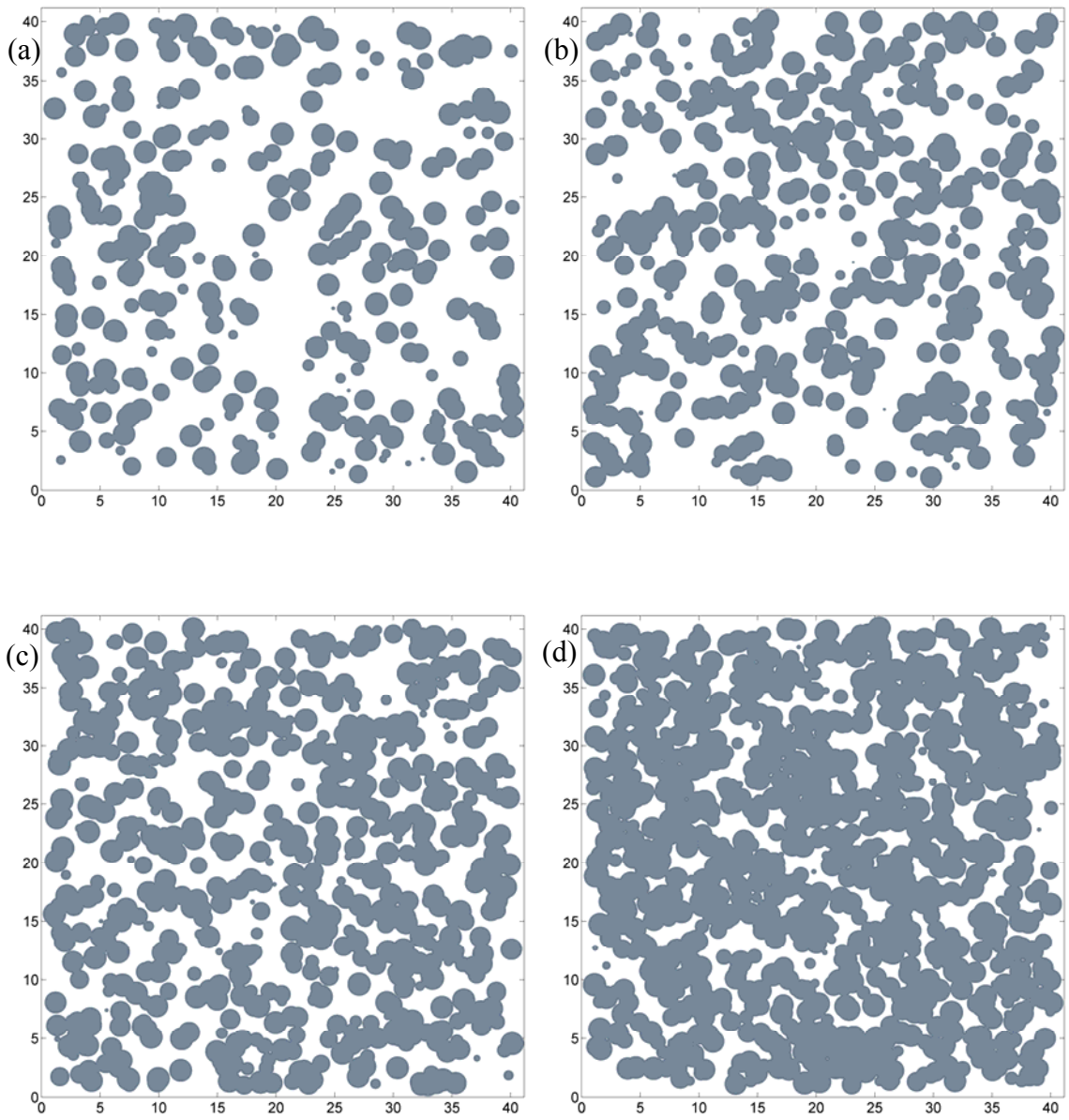

Figure 3-24. Percolation simulation results showing 2-D cross-sectional spatial changes as the volume fraction of GDC, ϕ_{GDC}, varies from (a) 0.30, to (b) 0.425, to (c) 0.55 and to (d) 0.70. Particle radius was set to 1.0, particle radius standard deviation and particle overlap parameters were both set to zero (monodisperse particles and complete overlap allowed).

Following the spatial output from the simulation are the actual simulation results. The effect of the above four parameters on percolation, the total amount of TPB length and the corresponding amount of active TPB length are shown in Figure 3-25 through Figure 3-27. In all three figures, sub-figure (a) shows the standard deviations for the percolation and TPB length calculations, (b) shows how the percolation varies with volume fraction of GDC, (c) shows how the total amount of TPB length varies with volume fraction of GDC, and (d) shows how the amount of active TPB length varies with volume fraction of GDC. For each plot, a minimum of 20 simulation runs were completed. The experimental data shown in Figure 3-9 shows that the total TPB length initially increases with increasing volume fraction of GDC to a maximum and then decreases again for values greater than 0.5 (note the figure shows volume fraction of LSM which is $1 - \phi_{GDC}$). A similar trend was witnessed for the total simulated TPB length shown in Figure 3-25c, Figure 3-26c and Figure 3-27c. In each case for an increasing volume fraction of GDC, the total TPB length increased to a maximum and then began to decrease again. This volume fraction effect confirms the earlier assertion that for sinterable materials, a maximum in perimeter will be reached as the volume fraction of one phase is increased. The overlapping sphere model simulates the sintering effect and thus we obtain negative gains in TPB length beyond a critical volume fraction of GDC. This does not hold for non sinterable materials, as the addition of more of one phase continuously increases the perimeter.

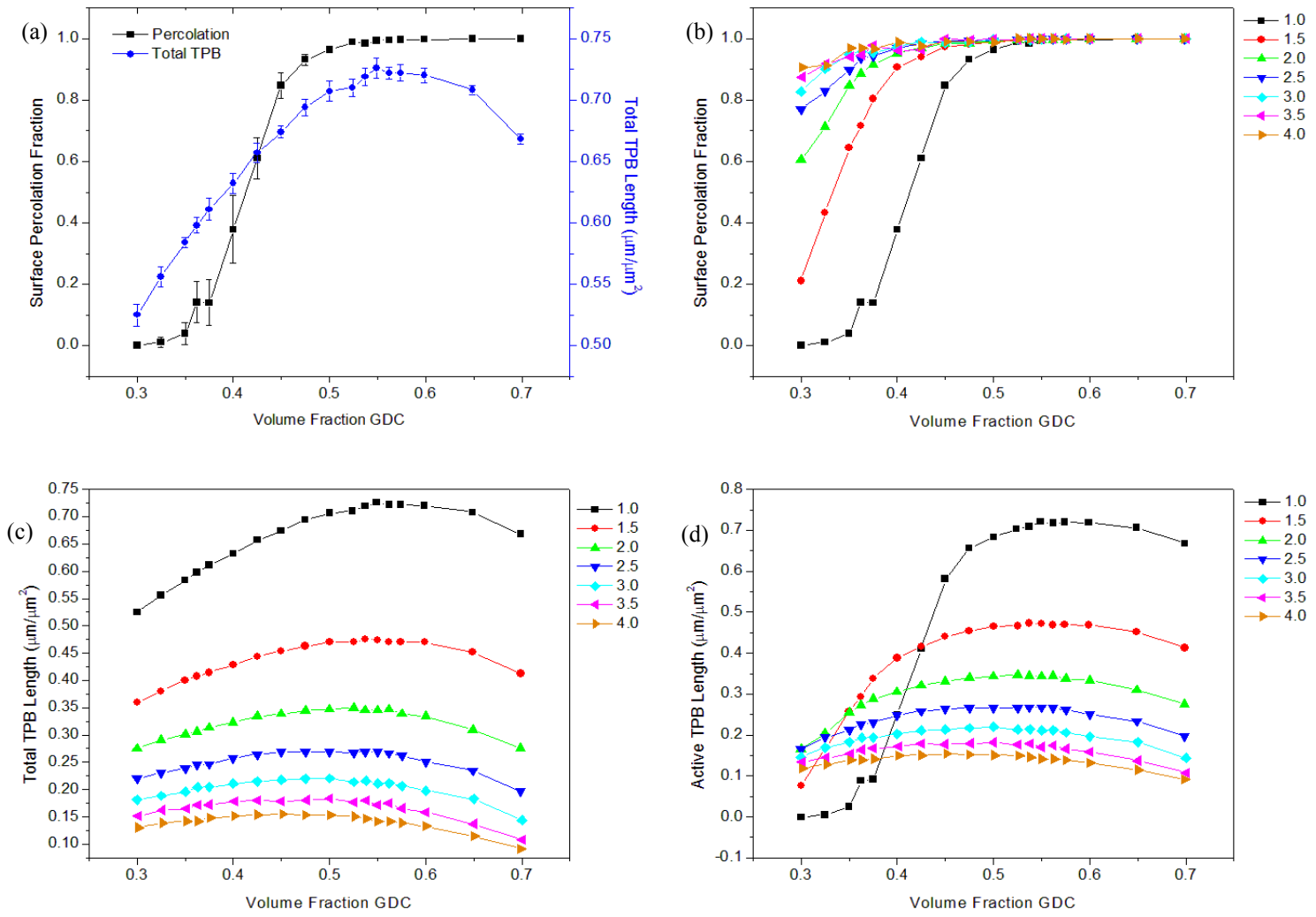

Figure 3-25. Percolation simulation results for various values of μ (σ and σ_c were both kept constant at 0) Plots show (a) typical deviations between simulations, (b) percolation, (c) total TPB length and (d) active TPB length.

The effect of average particle radius is shown in Figure 3-25(b) – (d). Sub-figure (b) shows that as the radius is increased from 1.0 to 4.0μm, the onset of significant levels of percolation shifts to lower and lower volume fractions of GDC. Thus, as the aspect ratio of particle radius, r, to sample space parameter L_0 increases, the probability of percolation occurring at lower volume fractions increases. Conversely, as shown in sub-figure (c), as the ratio r/L_0 increases, the amount of total TPB length decreases at each corresponding volume fraction point. This is because the volume of the spheres increases proportionally to r^3 while the surface area increases proportionally to r^2 causing increases in r to shift the amount of total TPB length to lower values. The effect on active TPB length results from a competition between the percolation effect and the total TPB length effect. The high percolation values for the larger particle radii cases serve to offset to their relatively low total amounts of TPB for the lower volume fractions of GDC giving a typically overall higher value of active TPB length. This trend reverses itself as the amount of active TPB becomes more dependent upon the amount of total TPB length at the higher volume fractions of GDC.

Another interesting effect of particle radius is that as it increases, it tends to push the maximum value for the total amount of TPB to higher volume fractions. The overall effect of particle size seems to be to shift the onset of significant amounts of percolation to lower volume fractions while sacrificing the total amount of TPB length. In designing composite electrodes for maximum amounts of active TPB length, smaller grain sizes and higher volume fractions for the electrolyte would be ideal.

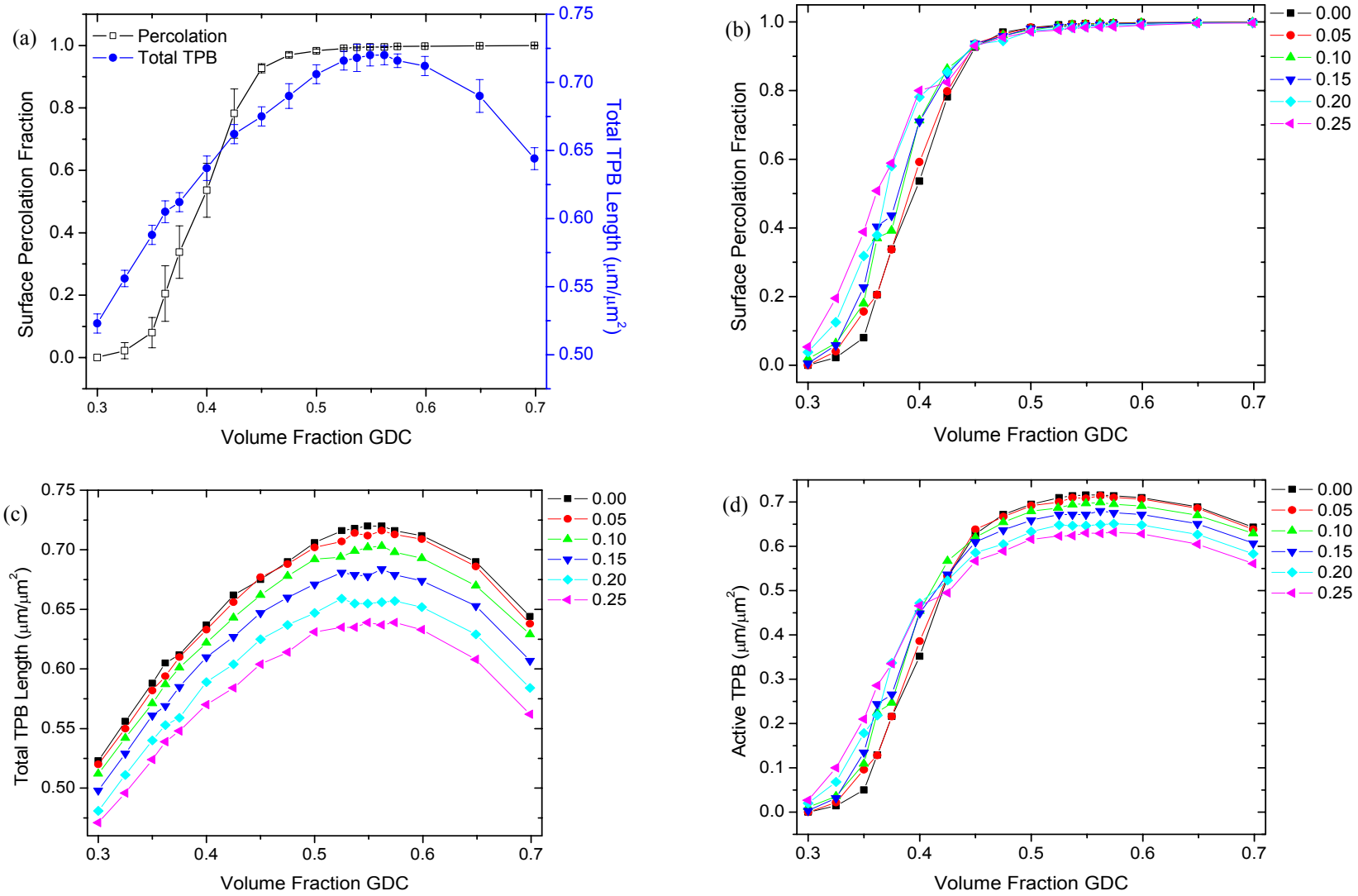

Figure 3-26. Percolation simulation results for various values of σ (μ was kept constant at 1.0 and σ_c was kept constant at 0). Plots show (a) typical typical deviations between simulations, (b) percolation, (c) total TPB length and (d) active TPB length.

The effect of particle size distribution is shown in Figure 3-26(b) – (d). Again, the distribution used was the log-normal distribution and not the normal distribution. Because of this, increases in the particle size standard deviation serve to add more larger sized particles than smaller sized ones to the simulation producing an effect similar to that seen with changes in r above. Sub-figure (b) shows that as the simulation distribution increases from the monodisperse case, the fraction of percolating particles shifts to lower values of the volume fraction. Due to the increasing numbers of large sized particles, the total amount of TPB decreases at each volume fraction of GDC point with increasing standard deviation values.

As with the previous parameter, μ, the simulations with smaller values of σ initially begin with smaller overall active amounts of TPB but quickly reverse that trend with increased GDC volume fractions. The effect is much less pronounced than that seen for the μ parameter. As with that parameter, in designing composite electrodes for maximum amounts of active TPB length, tighter particle size distributions (smaller values of σ) and higher volume fractions for the electrolyte would be ideal.

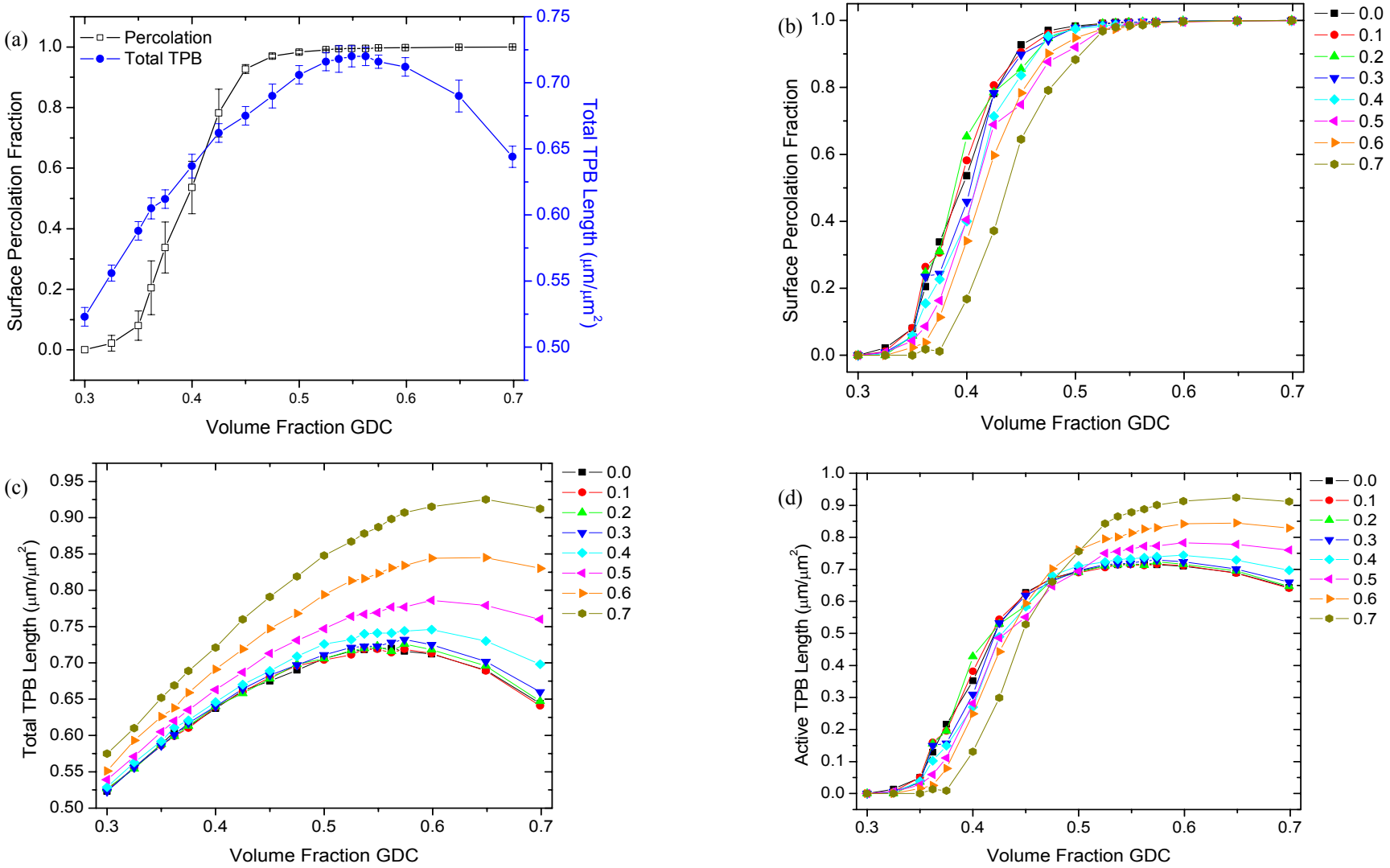

Figure 3-27. Percolation simulation results for various values of σ_c (μ was kept constant at 1.0 and σ was kept constant at 0). Plots show (a) typical deviations between simulations, (b) percolation, (c) total TPB length and (d) active TPB length.

The effect of particle overlap is shown in Figure 3-27(b) – (d). Sub-figure (b) shows that percolation values are shifted to higher volume fractions as the amount of allowable overlap is decreased (σ_c is increased). However, increasing σ_c serves to increase the amount of total TPB length at each volume fraction. Additionally, the maximum in total TPB length is shifted to higher volume fractions of GDC as σ_c increases. For the completely hard sphere model (σ_c = 1.0) no maximum in total TPB length would be seen as a linear trend would be expected. Unlike the effect in the changes in μ, increasing the volume fraction (adding more spheres to simulation) will always add more surface area to the simulation at the same rate as the volume fraction is increased. Thus, a doubling of the volume fraction will correspond to a doubling in the amount of surface area. In fact, sub-figure (c) shows that the model approaches linearity as σ_c approaches 1.0.

In designing composite electrodes for maximum amounts of active TPB length, having the particles maintain their spherical shape (less sintering), while still achieving high densities and having higher volume fractions for the electrolyte would be ideal.

Comparison of simulation results with experiment

Various microstructural trends can be garnered from Figure 3-10 and, through comparison with the simulation results, can help to explain Figure 3-9. As the volume fraction of GDC increases, the particle size also tends to increase. According to the simulation results, this would cause the amount of total TPB length for the higher volume fractions of GDC to be less than the case where the particle size did not change, relative to the lower volume fraction points. Additionally, the error bars on the points in Figure

3-10 give a measure to the deviation from the average particle size. As seen in the figure, the particle size distribution also tends to increase as the volume fraction of GDC increases. This would further depress the amount of total TPB length of the higher GDC volume fraction points relative to a constant distribution. This has the effect of shifting some of the points in Figure 3-9 to right as shown qualitatively in Figure 3-28

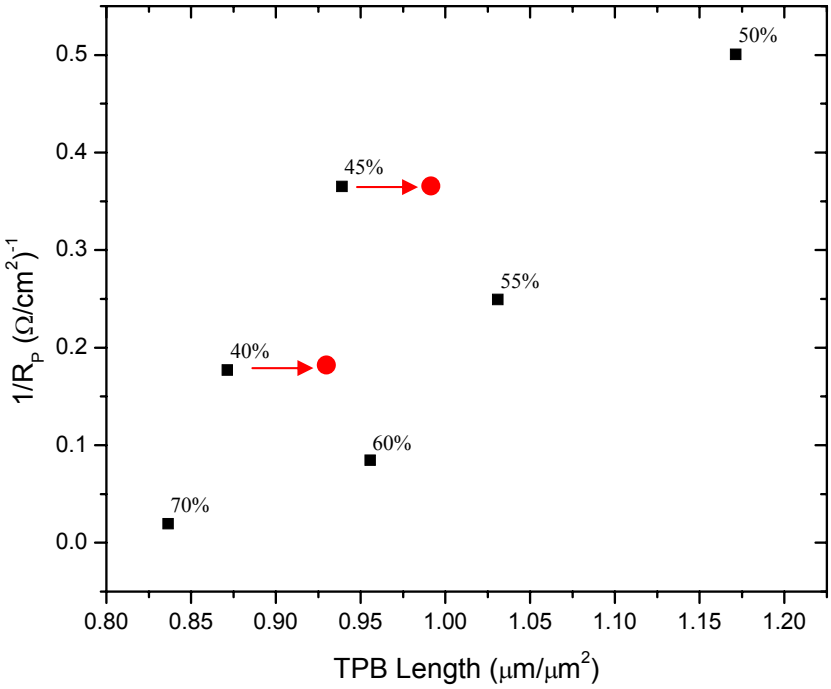

Figure 3-28. Reproduction of Figure 3-9 showing a qualitative shifting of some data points based upon the percolation simulation results.

The main change to Figure 3-9 would come via the effect of percolation. As reinforced in all the simulations, the lower volume fraction of GDC points, would have significantly lower amounts of active TPB length than the higher volume fraction points. This would cause a negative shift along the TPB length axis for those low GDC points. Qualitatively, these two effects are shown in Figure 3-29 below.

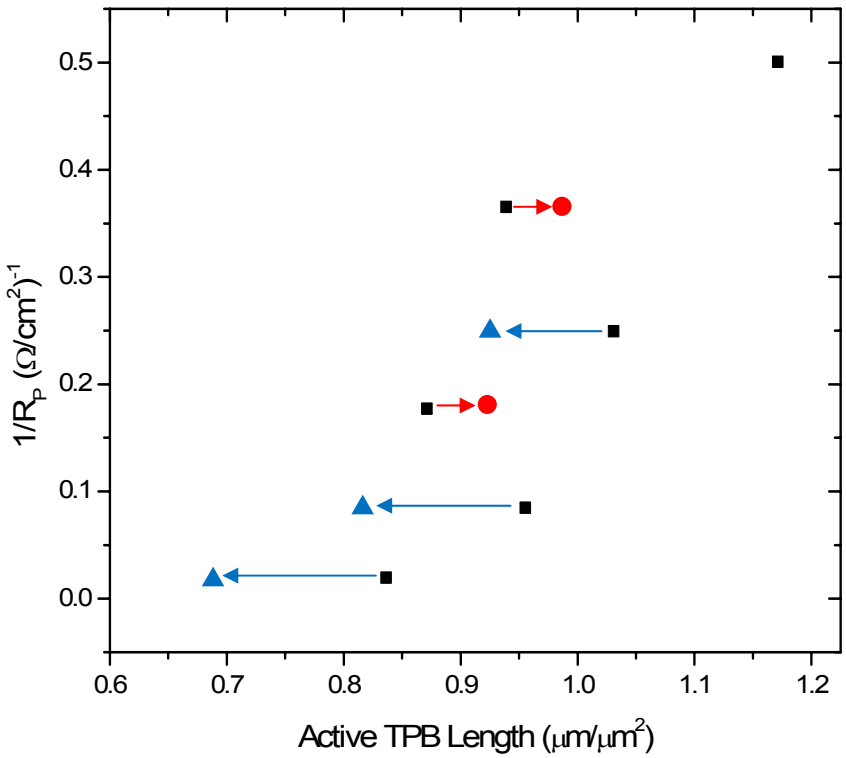

Figure 3-29. Qualitative representation for how the amount of active TPB length would change the data position of the data presented earlier in Figure 3-9. ● represent data points shifted due to changes in particle size and ▲ represent data points shifted due to percolation effects.

The representation in Figure 3-29 produces a plot that has much more linearity than its predecessor; however, it should be noted that the plot is only a qualitative representation based upon the conclusions drawn from the percolation simulation. Also according to the simulation results (and depending upon the particular choice of input parameters), a maximum in TPB length should be seen between 47 – 57 volume percent of GDC. Coupling all of the simulation results gives the following guidelines for optimal testing conditions for the dense composite cathode:

1. Volume percentage of the electrolyte phase should fall between 47 and 57 percent.
2. The particle size of the electrolyte phase should be as small as possible to maximize the amount of TPB length.
3. The particle size distribution should be as narrow as possible.
4. Sintering of the electrolyte phase should be discouraged, but sintering of the second phase (LSM in this case) should be encouraged to improve overall densification (a requirement for the composite electrode) and to maximize the contact area (TPB) between the two phases.

The following section will present the EIS data obtained from these samples at the conditions described in Table 3-1.

EIS Performance Data

Presented below is a sampling of the EIS spectra collected under the experimental conditions laid out in Table 3-1. To address the concerns of reproducibility of the samples, each set of impedance data was repeated across a minimum of three different sample sets. This allowed for a consistency check in the fabrication procedure and helped to optimize the fabrication methods. For this platform to be used as a viable method for testing, a great deal of confidence must be placed on the reproducibility across sample sets; otherwise, one could not compare data collected over time. All data presented has been reproduced at least twice and each dataset has been within an experimental error range of 0 – 10% difference (as determined from comparison of EIS data). Additionally, as the 50 volume percent samples produced some of the largest amounts of TPB length, the data shown here are all for the 50 – 50 LSM/GDC volume ratios.

Initial testing with the painted silver cathodes (the first testing setup) was abandoned for three reasons. The first was a concern about the current collection from the dense cathode surface. It was suspected that the sheet resistance of the cathodes was such that the entire surface was not active. Previous studies had shown this to be the case with thin electrodes and those with low conductivity[56]. The second concern presented itself after initial EIS testing with an applied overpotential. Optical images of the sample surface before and after testing are shown in Figure 3-30. The final concern was that the painted silver may have been participating in oxygen reduction reaction and obscuring the LSM – GDC – air TPB data.

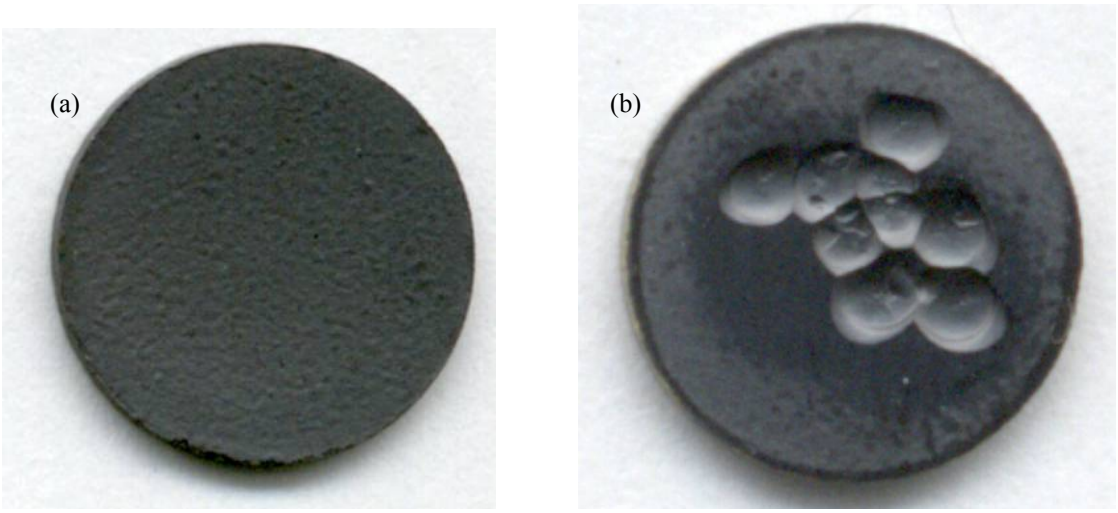

Figure 3-30. Optical images showing of the sample surface (a) before and (b) after EIS testing with an applied overpotential up to 0.300V

Upon inspection of the sample after testing, extreme localized deformation of the surface was found. All of the deformation was localized around the painted silver current collector. After careful removal of the silver layer, spherical indentations in the surface were observed. The deformation seen was reminiscent of melting and not of physical trauma to the surface. This, coupled with the fact that the deformation was only seen after applying an overpotential during the EIS testing, led to an enlarging of the sample surface area and changing the testing setup to alleviate this issue. The sample size was adjusted from using a 10mm die to a 13mm die and the testing setup was changed from that in Figure 3-6 to the testing setup shown in Figure 3-7. The changes were made in an attempt to collect current from the entire sample surface (use of a metal mesh in place of the painted silver), isolate the oxygen reduction reaction to LSM – GDC – air TPB (replacing silver which is highly active to the oxygen reduction reaction with a less active metal such as platinum or gold) and to spread the current over a larger surface area to prevent the melting effect.

After the above changes to both the testing setup and the sample preparation were made, no distortion of the sample surface was seen even after applying an overpotential of 0.300V for the duration of the EIS testing. The metal used in the testing setup for current collection was typically 80 mesh platinum woven from 0.076mm diameter wire. The mesh covered the entire sample surface and was fine enough to minimize the effects from sheet resistance, but also coarse enough to allow sufficient oxidant flow to reach the sample surface.

As mentioned previously, each measurement was performed over multiple sample sets to ensure reproducibility of the data. Figure 3-31 and Figure 3-32 below show the EIS results obtained from samples tested from three different sample sets. The testing was done in air at 650°C without an overpotential applied. Good agreement between the sample sets was seen, with slight variations in the ohmic resistance (high frequency intercepts of Figure 3-31 and also in the inset for a magnified view) and the widths of each subsequent loop. The Bode plots show even better agreement across the frequency range tested. This data agreement was typical across all the sample sets prepared and tested in the quartz testing setup.

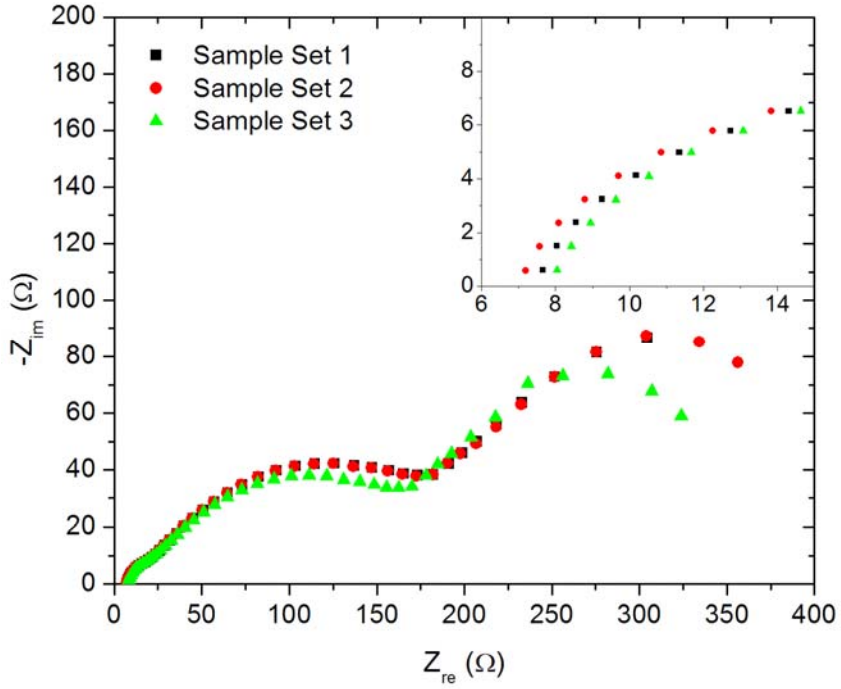

Figure 3-31. Nyquist plot across three sample sets for the EIS data taken at 650°C in air with no applied overpotential

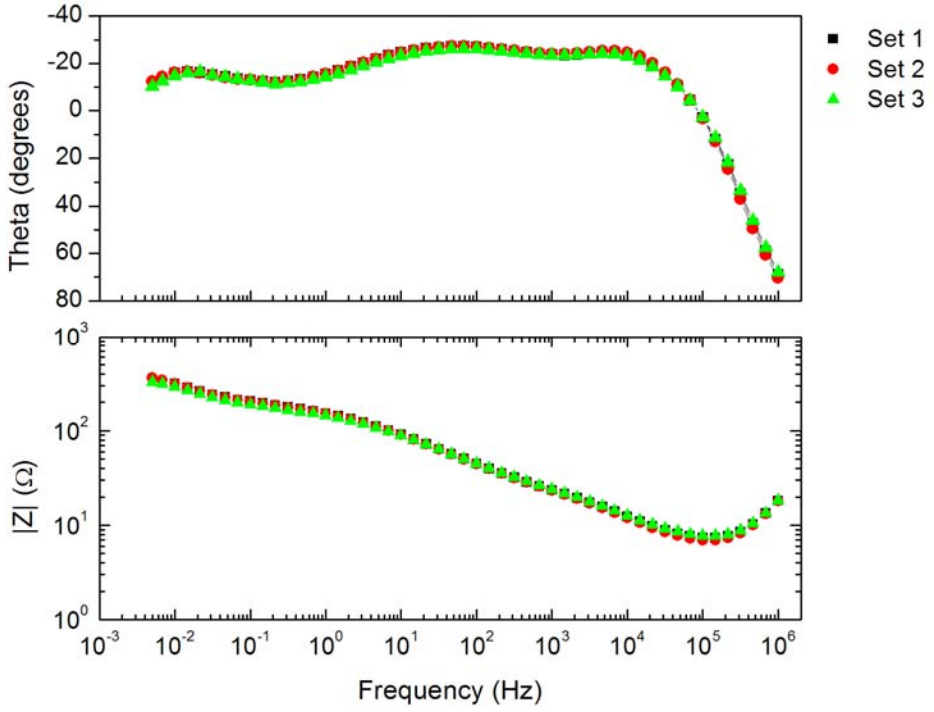

Figure 3-32. Bode plots across three sample sets for the EIS data taken at 650°C in air with no applied overpotential

Once the sample reproducibility was confirmed, the testing conditions set out in Table 3-1 were completed. Figure 3-33 and Figure 3-34 show typical results seen as the temperature was varied from 650°C – 750°C. The experiments were performed on the 50 – 50 volume percent (LSM – GDC) essentially ensuring that the majority of the sample surface was connected and active, according the percolation model results in the previous section. The impedance data presented has been scaled by the total area of the composite electrode. Additionally, the inductive portion on the Nyquist plot (stemming from the lead wire connections) is not shown.

As the temperature was increased during the testing, the impedance for all processes decreased. The Nyquist plot shows two clearly discernable loops with the possibility of a third loop on the high frequency end of the plot. Support for this third loop is further seen in the Bode plot of magnitude versus frequency as a nearly horizontal area is seen in the frequency region of $3 \cdot 10^4$ to $2 \cdot 10^5$. The phase angle versus frequency diagram shows two resistive processes (signified by flat areas around the 0° phase shift line) and the makings of a third had the tests been allowed to proceed to lower frequencies. As expected the ohmic resistance of the cell (contributions coming mainly from the electrolyte) decreased with increasing temperature also.

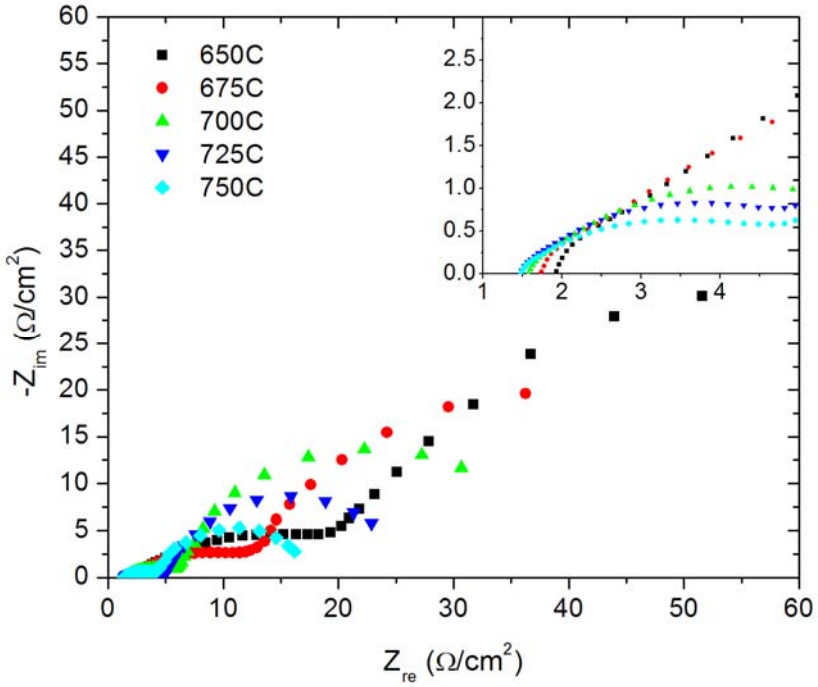

Figure 3-33. EIS data showing how the impedance varies with temperature. The inset shows the high frequency points in greater detail. Data were collected in oxygen and without an applied overpotential.

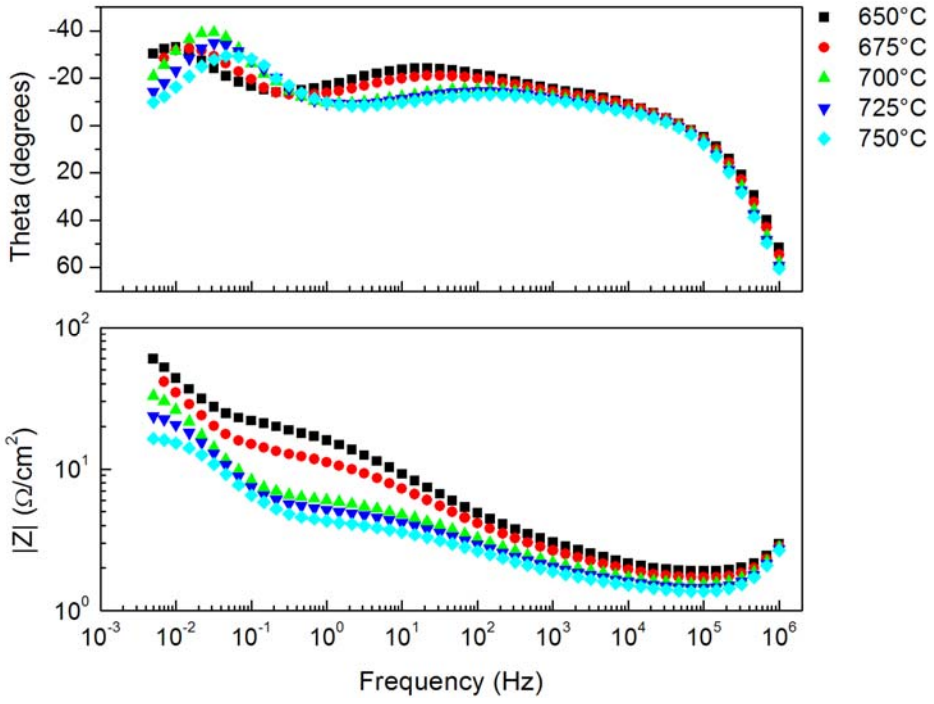

Figure 3-34. Bode plot showing how the impedance data varies with temperature. Data were collected in oxygen and without an applied overpotential.

The effect on the impedance by changing the partial pressure of oxygen provided to the cell is shown in Figure 3-35 and Figure 3-36 below. Again two clear semicircles are seen in the Nyquist plot (with the same possibility of a higher frequency loop being obscured) signifying that at least two overlapping processes occurred during testing. A complete experiment was one where the low frequency loop finished on the real axis in the complex plane (Nyquist plot). Although the impedance experiments were typically not allowed to run to completion (the lower frequencies were time prohibitive), the software used to run the Solartron hardware (Zplot) included a complex nonlinear least squares (CNLS) fitting algorithm that allowed for precise fitting of the impedance data to give an accurate estimate of where the data would have progressed to, had the experiment continued to completion.

It was expected that a reduction in the partial pressure of oxygen would lead to an increase in the impedance for any diffusive process or any process directly dependent upon changes in p_{O2}. The data show that increasing the partial pressure of oxygen had the effect of decreasing the polarization resistance, R_P (given by the difference between the low frequency intercept and the high frequency intercept on the Nyquist plot). While both loops in the Nyquist plot were decreased after the increase in p_{O2}, the plots show that the high frequency loop experienced more of a reduction than the low frequency loop. This difference was much more pronounced at lower temperatures where diffusive processes are believed to dominate the electrode reaction. Though diffusion is typically associated with the lowest frequency loop, the data suggest that the next to lowest frequency loop relates to a diffusive process.

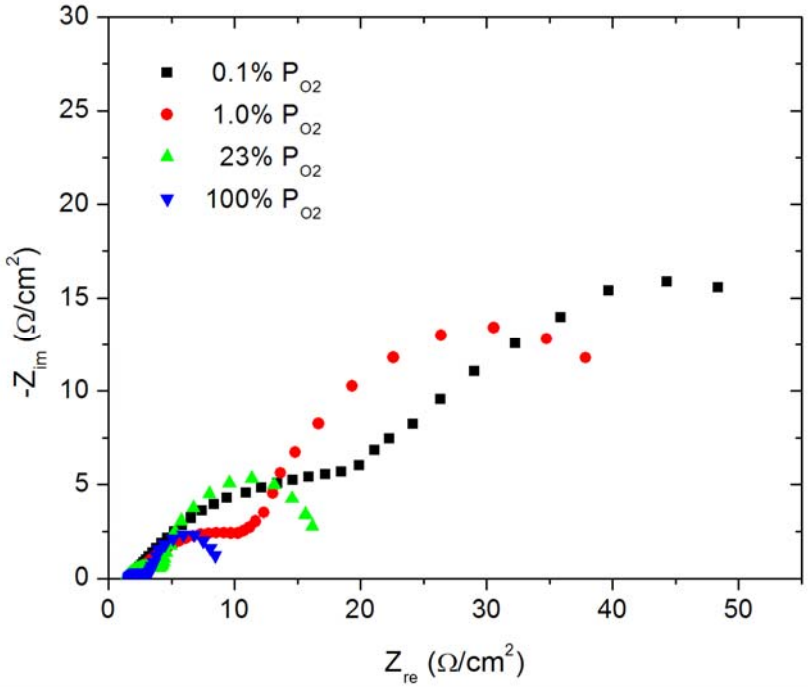

Figure 3-35. EIS data showing how the impedance varies with the partial pressure of oxygen. Data were collected at 700°C and without an applied overpotential.

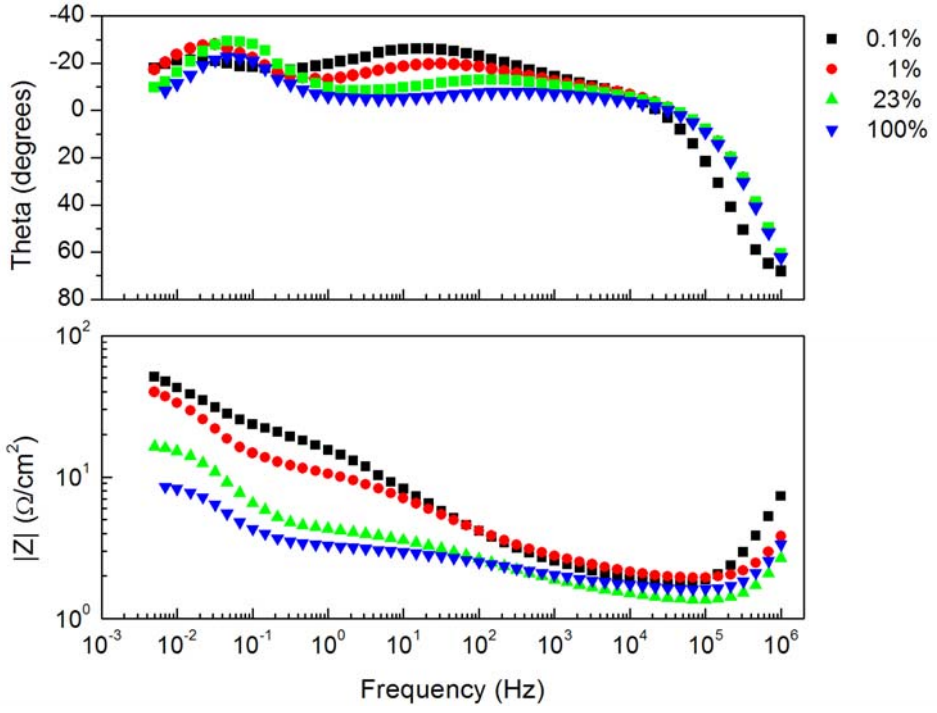

Figure 3-36. Bode plots showing how the impedance varies with the partial pressure of oxygen. Data were collected at 700°C and without an applied overpotential.

The effect of an applied overpotential on the electrode impedance is show in Figure 3-37 and Figure 3-38 below. The data shown were collected at 700°C in air. Applying an overpotential to the cell should have the primary effect of making the electrode reaction more facile. This in turn should lead to lower impedance for the reaction occurring at the TPB. Increasing the overpotential should also lower the equilibrium amount of surface oxide species (assuming the adsorption/desorption reaction is not potential dependent), thus a reduction in the impedance should be seen initially, but then an increase is expected. This effect was not seen during the testing as a sufficiently large overpotential was not applied to the sample due to the earlier issues involving the previous testing setup.

Here again, we saw a reduction in R_P as the applied overpotential was increased, but the reduction was not equal between the two main loops. The low frequency loop experienced more of a reduction in its impedance than the next to lowest frequency loop. This loop was attributed to the electrode reaction occurring at the TPB. To further support this, the data were examined under conditions where diffusion would not be expected to dominate the overall electrode reaction (high oxygen partial pressure and high temperatures) and a much larger discrepancy between the loop reductions was found.

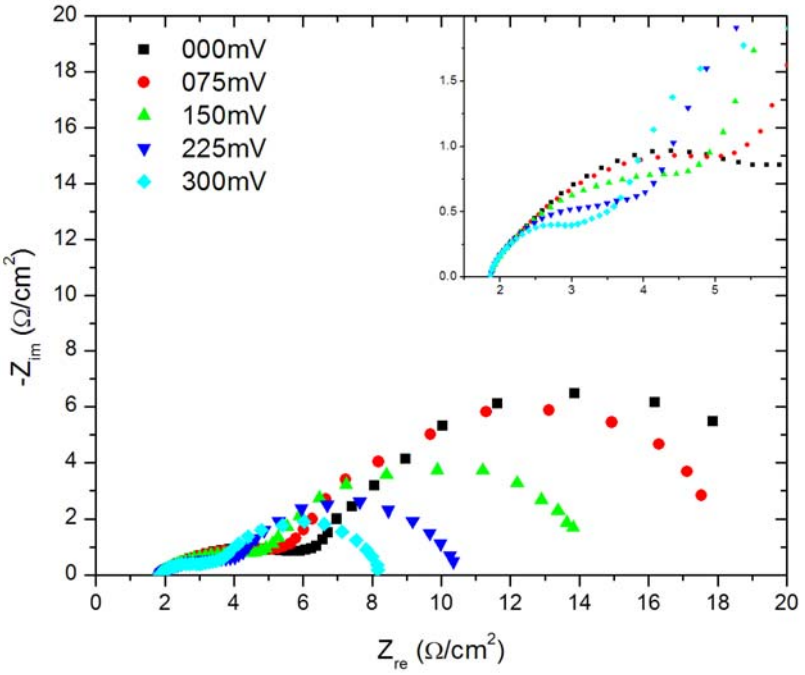

Figure 3-37. EIS data showing how the impedance varies with an applied overpotential. The inset shows the high frequency points in greater detail. Data were collected in air and at 700°C.

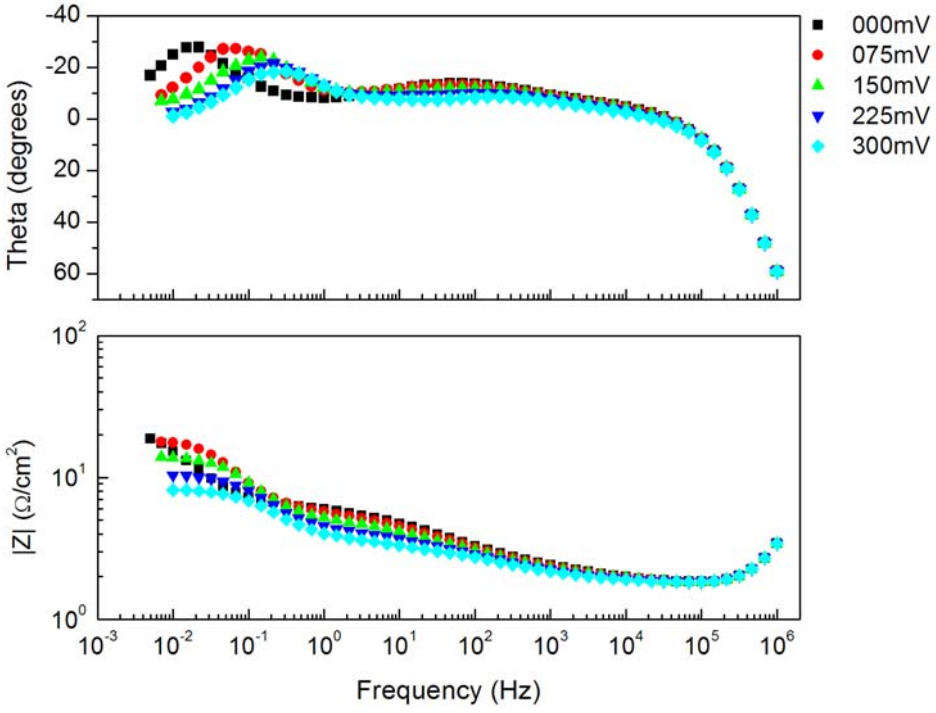

Figure 3-38. Bode plots showing how the impedance varies with an applied overpotential. Data were collected in air and at 700°C.

The relationship between the inverse area specific polarization resistance and the partial pressure of oxygen is shown below. Other researchers have shown a much higher dependence of R_P on p_{O2} witnessing a peak in their plots at lower partial pressures; however, they also performed the testing over a much greater temperature range extending down to 500°C [57, 88]. They found that the peak shifted to higher partial pressures of oxygen as the temperature increased. Because of this effect, better agreement with those studies and the present one occur at the higher temperatures where the plots were only linear over the same ranges. Additionally, to obtain a clear dependence on oxygen partial pressure, a comparatively large number of partial pressures were used as opposed to the four used in this study.

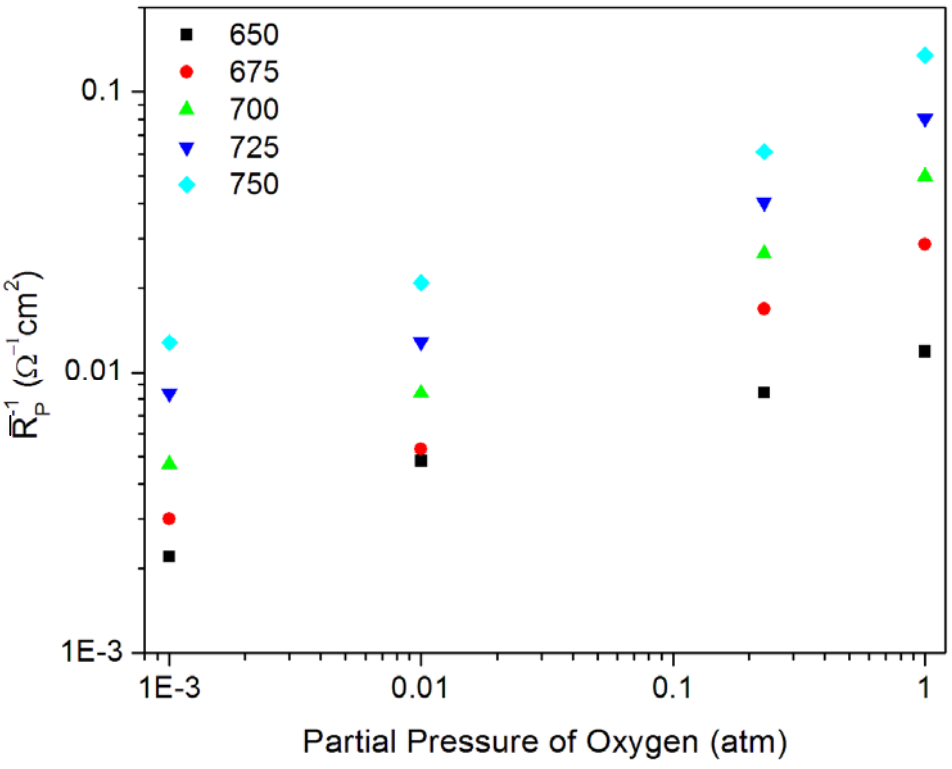

Figure 3-39. Inverse area specific polarization resistance as a function of pressure at various temperatures. Data were obtained from EIS measurements at 0 mV applied overpotential.

Of greater interest was the determination of the activation energy for the reactions. Figure 3-40 and Figure 3-41 show the Arrhenius plots of the inverse area specific polarization resistance as a function of partial pressure of oxygen and an applied overpotential, respectively. The activation energy decreases with decreasing partial pressure of oxygen and decreases with increasing applied overpotential. This can give some insight as to the reaction mechanism and the steps that are rate limiting over the various experimental conditions. At low temperatures and high partial pressures, the surface coverage of adsorbed intermediates should approach 1 because the likelihood of adsorption is greatly increased. Conversely, the lower temperatures hinder the reaction occurring at the TPB and thus, we saw higher activation energies for the mechanism. The TPB reaction should be the rate limiting step for this experimental condition. At the other extreme, under high temperatures and low partial pressures of oxygen, the likelihood of the adsorbed intermediates desorbing from the surface greatly increases and the surface coverage approaches zero. The increased temperature also serves to increase the TPB reaction causing the rate limiting step to switch to one of adsorption or diffusion.

An applied cathodic overpotential has the effect of shifting the rate limiting step from charge transfer controlled to adsorption or diffusion controlled. This occurs because application of a DC bias lowers the barrier for the charge transfer step making that process more facile. A counter effect of this is that because the charge transfer step is occurring more readily while the adsorption remains constant, the surface concentration of adsorbed intermediates decreases leading to adsorption or diffusion controlled kinetics.

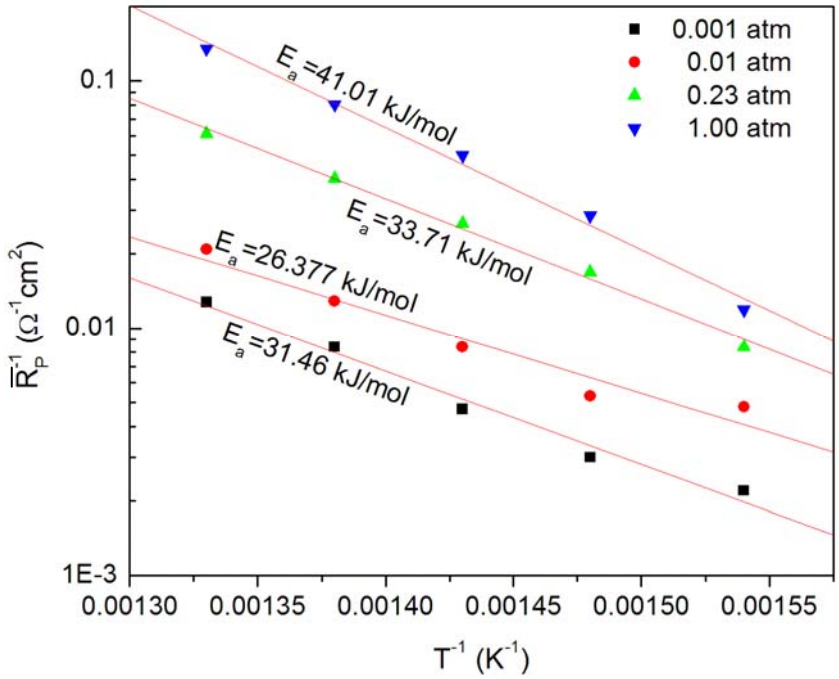

Figure 3-40. Isobaric Arrhenius plots of the inverse area specific polarization resistance. The activation energies calculated from the slopes of the linear fits are given in the plot.

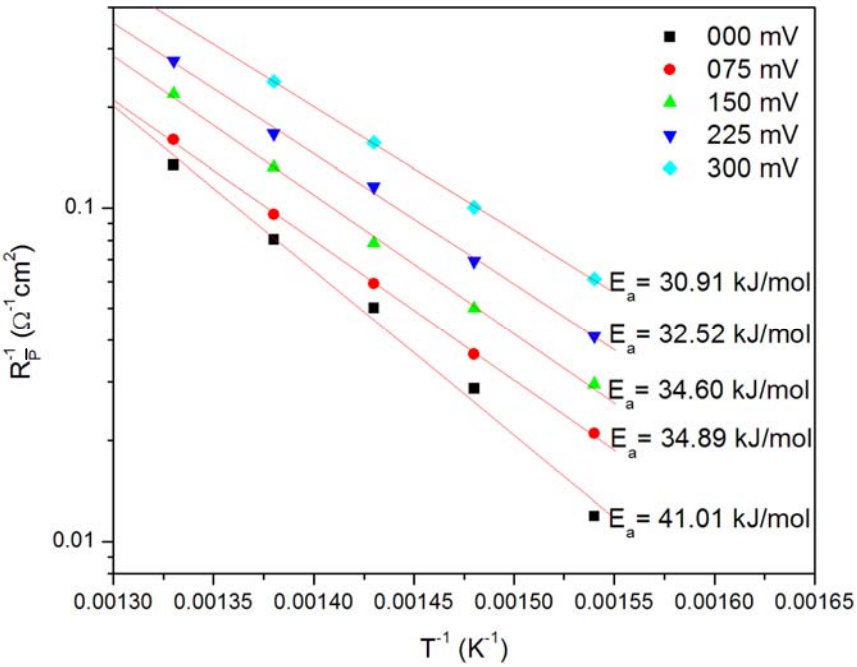

Figure 3-41. Potentiostatic Arrhenius plots of the inverse area specific polarization resistance. The activation energies calculated from the slopes of the linear fits are given in the plot.

From the above analysis, it appears that there are multiple steps in the reaction mechanism for this oxygen reduction reaction and that none are overwhelmingly dominant. Studies have shown that only one well-defined semicircle is typically present when the reaction mechanism is rate limited by only one step in the mechanism [89]. Additionally, it is typically a consensus opinion that during the collection of impedance data, the actual reaction kinetics occurring will be obscured by the double layer capacitance [59, 63, 90]. The double layer capacitance, C_{dl}, is typically introduced as a parallel element with the other faradaic processes occurring in the cell. Thus, during an impedance experiment, the total current through the interfaces is a sum of the faradaic current, i_f, and the double layer charging current, i_c. Figure 3-42 shows a schematic of the electrochemical cell (the electrolyte resistance, R_e is added as a series element in this description).

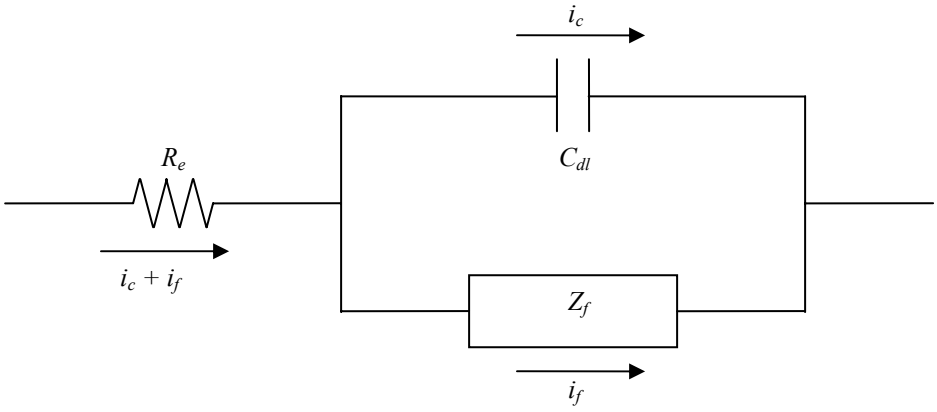

Figure 3-42. Equivalent circuit diagraph of an electrochemical cell showing the double layer capacitance in parallel with the faradaic impedance

For the purposes of determining the rate limiting steps and, ultimately, the reaction mechanisms, it is critical that the faradaic information can be extracted from the measured impedance data. One method for separating these parameters is to measure the cell impedance in a separate experiment under identical conditions, but in the absence of the electroactive couple, essentially deactivating the faradic path and leaving only R_e and C_{dl} [63]. This method, however, is often cumbersome, involving multiple experiments with complex setups or in most cases, not even feasible.

Recent work has shown a method for determining the overall value of a faradaic impedance being obscured by a double layer capacitance without prior knowledge of either [91]. The strength of this method lies in the fact that no use of an equivalent circuit for faradaic impedance is necessary. The only assumption made is that the double layer capacitance is in parallel with the overall faradaic impedance and all of that, in turn, is in series with the ohmic resistance (see Figure 3-42 above). The method works by subtracting out R_e and C_{dl} from the impedance data through an iterative process. One major drawback of the technique is that the accuracy of the C_{dl} calculation is highly dependent upon the value of R_e used. If this is not known very accurately, large deviations from the correct value of C_{dl} can arise.

Figure 3-43 shows the results of applying Berthier's C_{dl} subtraction technique on an idealized circuit. The values used are shown in Table 3-2. Following the idealized case shows the application of Berthier's technique on experimental data obtained under the conditions of 1 atm p_{O2}, 750°C and 0 applied DC bias.

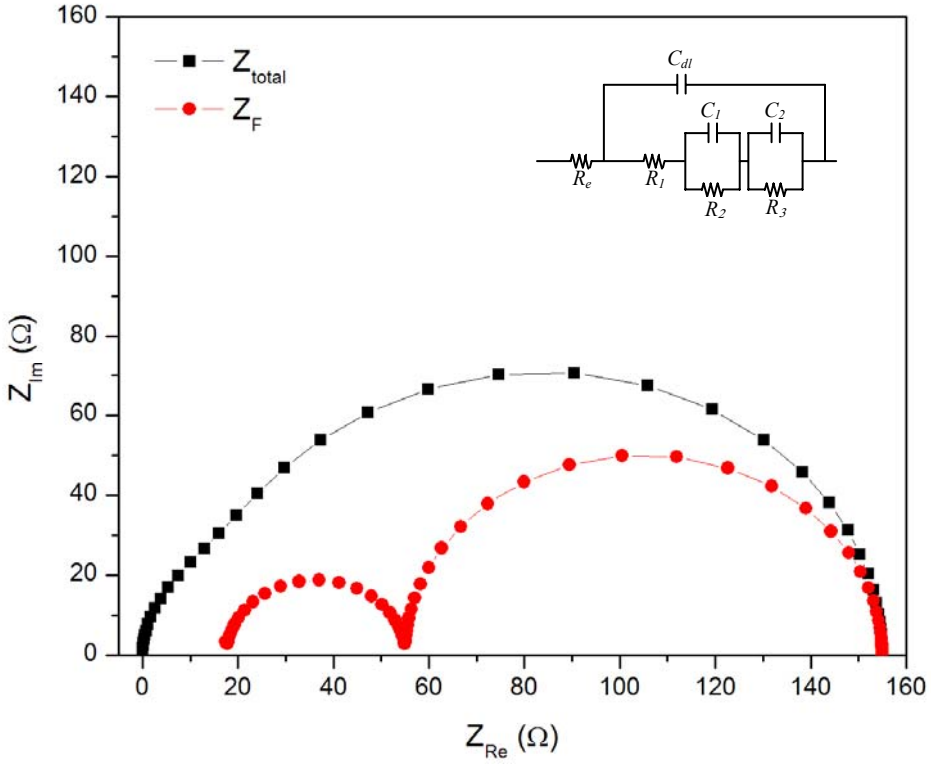

Figure 3-43. Ideal impedance spectra calculated from an equivalent circuit (upper right) showing the overall impedance (■), and the extraction of the faradaic impedance (●) using the method by Berthier *et al* [91].

Table 3-2. Calculation parameters used to simulate impedance spectra in Figure 3-43. Values correspond to the circuit in the upper right of the figure.

Circuit Element	Value
$\mathbf{R_e}$	10 Ω
$\mathbf{C_{dl}}$	$5.0 \cdot 10^{-4}$ F
$\mathbf{C_1}$	$1.3 \cdot 10^{-6}$ F
$\mathbf{C_2}$	$8.7 \cdot 10^{-4}$ F
$\mathbf{R_1}$	18 Ω
$\mathbf{R_2}$	37 Ω
$\mathbf{R_3}$	100 Ω

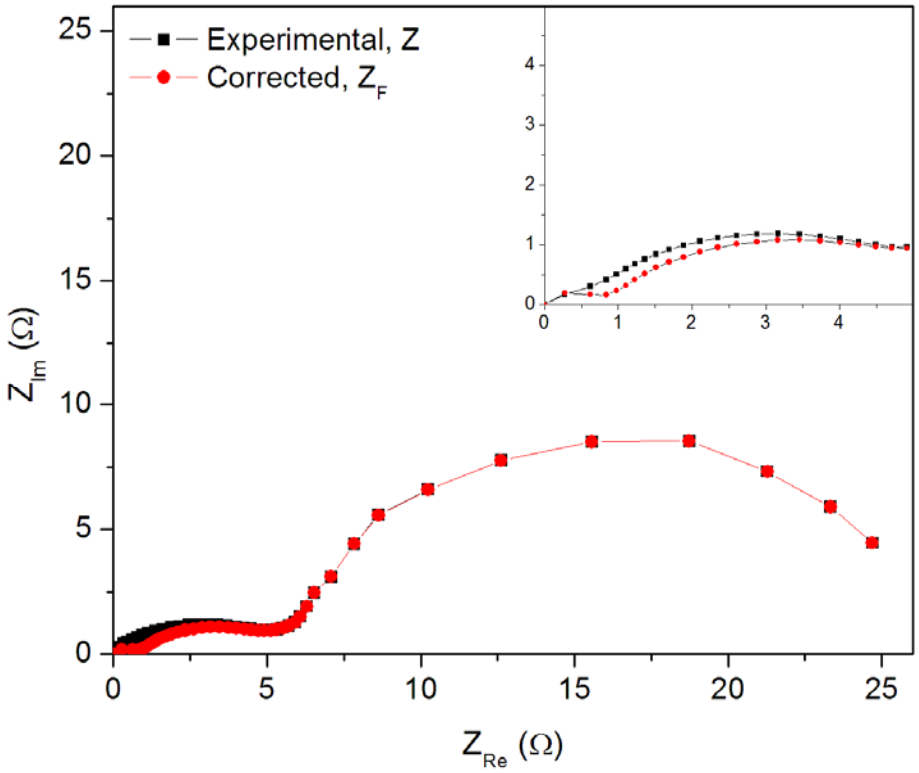

Figure 3-44. Plot showing application of the C_{dl} and R_e subtraction technique published by Berthier *et al*[91]. The low frequency loop remains constant, but a Z_F shows a high frequency loop previously obscured in Z.

The effect of separating out the faradaic impedance from the total impedance is much less noticeable when applied to the experimental dataset. Other authors have noticed this trend and chosen to use the experimental data as is[16]; however, this separation does more clearly reveal the high frequency loop that was expected to exist. For this data set, C_{dl} was determined to be $1.26 \cdot 10^{-4}$ F and a value of 5.97 Ω was used for R_e. R_e was determined from estimation of the high frequency intercept with the real axis in the Nyquist plot. As mentioned above, the value obtained for C_{dl} was highly dependent upon the choice made for the electrolyte resistance. This can be a significant source of error in the C_{dl} determination as errors in the estimate for R_e by ± a few percent can change the calculated value of C_{dl} by several orders of magnitude. Thus, the determined C_{dl} value is only as accurate as that of R_e.

Current – Voltage Performance Data

In addition to the above EIS experiments, Tafel experiments were also conducted at the various temperatures and oxygen partial pressures (shown in Figure 3-45). Assuming that the reaction is charge transfer controlled (only one charge transfer step in the mechanism is the rate limiting step), information such as the exchange current density, i_0, and the charge transfer coefficient, β, can be garnered from the Tafel analysis[63, 64].

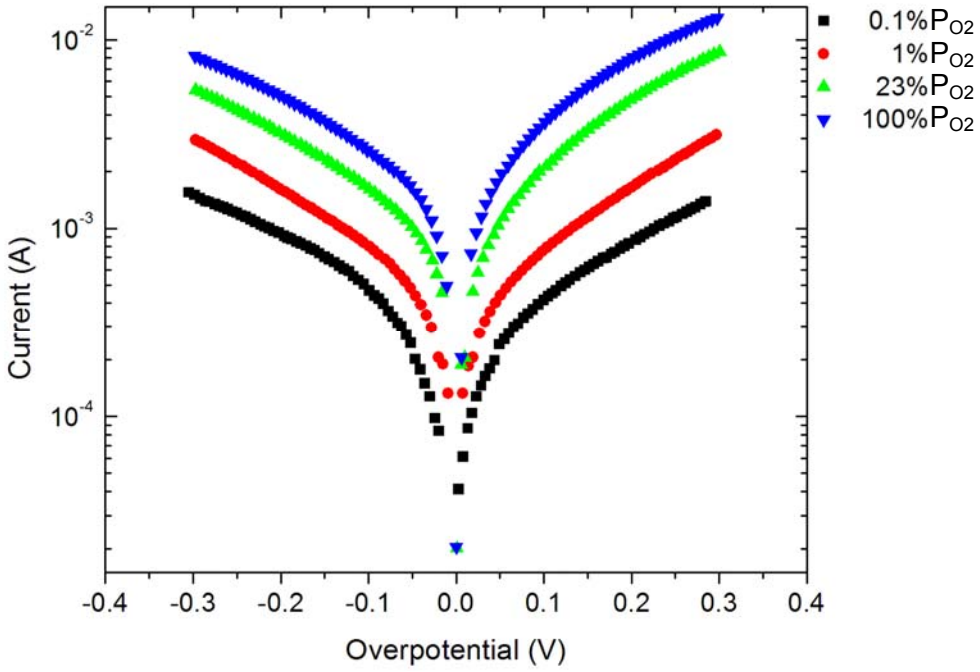

Figure 3-45. Isobaric Tafel plots conducted at 700°C

The exchange current density can be calculated from the linear sections of the Tafel plots. A linear fit of each branch of the Tafel plot is made and the current at which the two lines intersect is taken as the exchange current density. The potential at which

those two lines intersect is E_0. The apparent charge transfer coefficients can be calculated from the respective slopes of those lines and a model of the reaction mechanism.

In general, the linear sections of the anodic and cathodic sides of the plots had neither the same slope nor did they intersect at the zero potential point, thus producing a slightly asymmetric behavior. The expected behavior is for the Tafel slope to linearly increase with temperature as increasing overpotential lowers the activation energy, exponentially increasing the current density. The data in Table 3-3 exhibit this general increase in β save the values recorded at 675°C (the data obtained for the 675°C temperature is seen as an experimental outlier rather than a point of experimental interest).

Table 3-3. Kinetic data showing variation with temperature, gathered from experimental Tafel measurements in air.

Temperature (°C)	β_a **(mV)**	β_c **(mV)**	E_0 **(V)**	i_0 **(A)**
650	340.77	-385.95	-0.01476	$6.040 \cdot 10^{-3}$
675	360.24	-398.38	-0.02596	$8.848 \cdot 10^{-4}$
700	350.59	-390.01	-0.02152	$1.100 \cdot 10^{-3}$
725	387.95	-399.94	-0.02479	$1.655 \cdot 10^{-3}$
750	398.19	-408.14	-0.02187	$2.184 \cdot 10^{-3}$

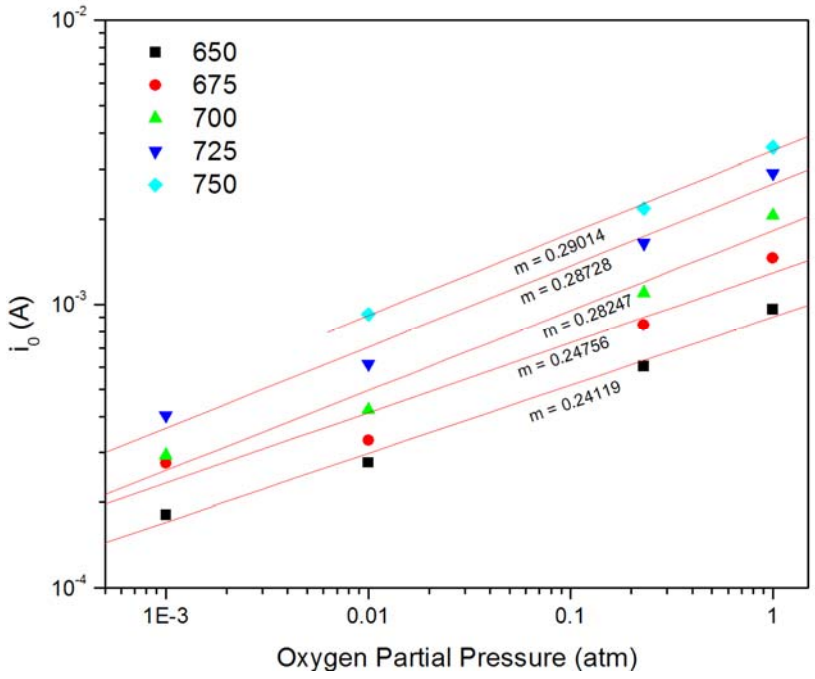

Figure 3-46. Isothermal curves showing the variation of i_0 with the partial pressure of oxygen assuming a constant Tafel slope.

Results from the Tafel analysis are presented in Figure 3-46. The i_0 dependence on partial pressure of oxygen is given by the slope of linear fit through the data points. Several studies have explored this relationship, both theoretically and experimentally, on metal electrodes and found an approximately $p_{O_2}^{1/4}$ dependence of i_0 for low p_{O_2} and high temperatures and an approximately $p_{O_2}^{-1/4}$ dependence of i_0 for high p_{O_2} values and low temperatures [92, 93]. These values were obtained using a Langmuir adsorption model for the oxide layers.

The above analysis assumed that the reaction mechanism remained constant across the partial pressure of oxygen range. Closer inspection of Figure 3-46 reveals that a change in the rate limiting step (signified by a change in slope) may have occurred

between 0.01 atm and 0.23 atm. Taking this into account, the log-log plot of exchange current density with partial pressure of oxygen is shown in Figure 3-47.

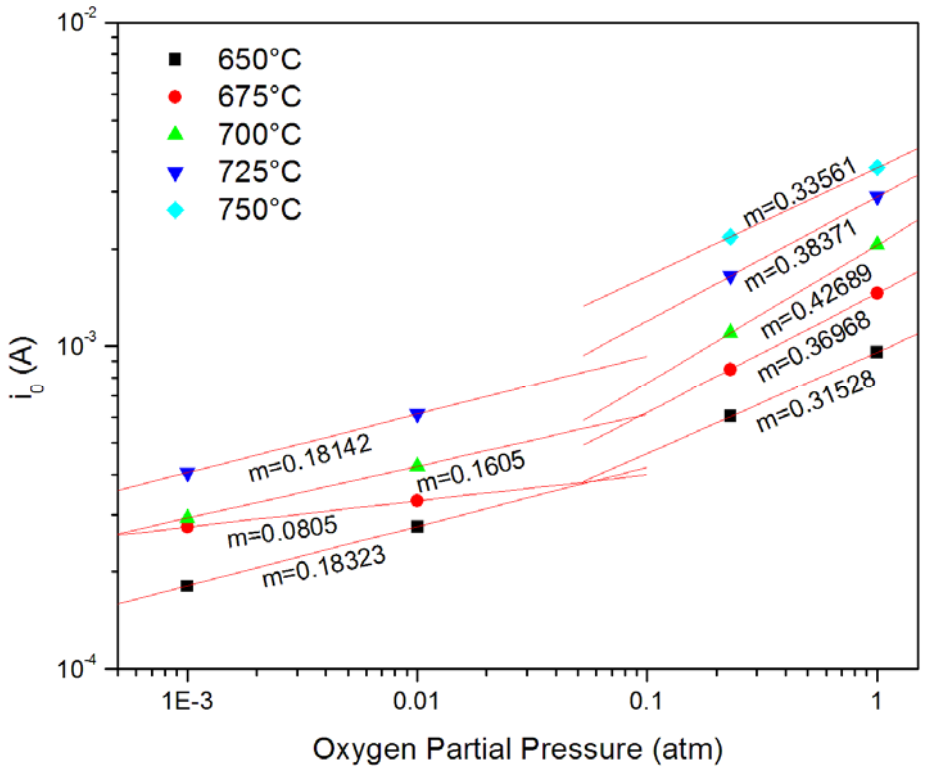

Figure 3-47. Isothermal curves showing the variation of i_0 with the partial pressure of oxygen assuming a variable Tafel slope.

The above figure demonstrates a change in the slope from approximately 0.17 to approximately 0.35. Other researchers reported similar changes in slope and attributed them to a change in adsorption kinetics going from molecular oxygen being adsorbed to a dissociative adsorption model [88]. These authors found that a 0.19 slope corresponded to dissociative adsorption. Based on that study and the current research, we believe that change in the rate limiting step occurred where the limiting step transitioned from being limited by dissociative adsorption to being limited by an electron transfer step (due to the

approximately $p_{O_2}^{\frac{3}{8}}$ dependence of the exchange current density discussed in the next chapter). This concurs with the earlier observations of the change in activation energy with oxygen partial pressure.

Conclusions

The mechanism for oxygen reduction at the LSM electrode is of major controversy in the current literature. We have developed a platform using a co-pressed and co-fired dense electrode/electrolyte composite to study these processes. This platform allows for rapid development and testing and allows us to limit the reaction zones to only the surface reactions which are accessible to *in situ* optical observations such as FTIR and Raman spectroscopy. Additionally, the length of TPB was calculated using repeatable stereological methods and the total length of TPB was controlled through varying the processing conditions. An overlapping spheres percolation model suggested that the majority of the TPB lines would be active and maximized if the volume percent of the electrolyte material was kept in the range of 47 – 57%. Additionally, other insights into the processing conditions to maximize the amount of active TPB length were garnered from both the stereology calculations and the percolation simulations.

Steady-state current voltage measurements as well as electrochemical impedance measurements on numerous samples under various environmental conditions were completed. The apparent activation energy for the reduction reaction was found to lie somewhere between 31 kJ/mol and 41 kJ/mol depending upon the experimental conditions. The exchange current density was found to vary with the partial pressure of oxygen differently over two separate regions. At relatively low partial pressures, i_0 had an

approximately $p_{O_2}^{0.17}$ dependence and at relatively high partial pressures, i_0 had an approximately $p_{O_2}^{0.35}$ dependence. This leads to the conclusion that a change in the rate limiting step occurs over as the partial pressure of oxygen is varied over the ranges studied. The experiments suggested that at high oxygen partial pressures, low temperatures and no applied bias leads to a charge transfer controlled reaction. Conversely, relatively low oxygen partial pressures, high temperatures and application of a cathodic overpotential leads to an adsorption or diffusion limited reaction.

In the next chapter we will focus on prediction of the composite cathodes' electrochemical performance through the simulation of proposed reaction mechanisms.

CHAPTER 4

MATHEMATICAL SIMULATION OF PROPOSED REACTION MECHANISMS

Reaction Mechanism Formulation

Possible reaction pathways and mechanisms were proposed and mathematically formulated to predict the dependence of kinetically controlled parameters (such as exchange current density, activation energy, electrode impedance, etc) on experimentally controllable conditions such as partial pressure of oxidant, temperature, and amplitude of DC polarization. Initially, the reaction mechanisms were formulated assuming a single rate-determining step for the reaction. This was then expanded to consider processes governed by multiple steps. The assumptions made for these formulations were that (1) electrode kinetics were governed by serial processes, (2) adsorption followed the Langmuir-type adsorption isotherms with no overlap of surface coverage (i.e. $\sum \theta_i \leq 1$), and that (3) microscopic reversibility ensued. Other mechanism specific assumptions were made as deemed necessary. The rates were expressed using mass-action laws and no assumption of low surface coverage was made, i.e. the concentration of adsorption sites is included in the formulation. The total number of surface adsorption sites was considered to be constant and independent of operating conditions and time.

As reaction pathways are typically materials dependent, the proposed mechanisms pertain to specific SOFC materials. Thus, the majority of mechanism development done was specific to perovskite-type materials on the cathode side since they are

overwhelmingly used as electrodes in SOFCs. Specifically, the material under investigation was strontium doped lanthanum manganate (LSM). The above mentioned material and others have been previously studied for use as electrodes in SOFC applications[4, 11, 12, 14, 17, 24, 28, 31, 39, 44, 46, 50, 94, 95] and will provide a good starting point for mechanistic studies. This study will, however, develop a methodology that is extendible to other types of materials.

Reactions occurring in SOFCs whether at the cathode or the anode are considered to be multistep processes involving various numbers of intermediates. It is the presence of these intermediates that ultimately decides via which particular reaction pathway the reaction proceeds. A method proposed by Lu *et al*[96] using potential dependent Fourier transform infrared emission spectroscopy (pd-FTIRES) has shown promise in detecting these types of reaction intermediates and is believed to be extendable to the systems under study. *In-situ* surface vibrational spectroscopy techniques such as Raman spectroscopy can be used to elucidate the specific reaction mechanism. These *in-situ* techniques can be used, for example, to try and determine whether the cathode surface contains only absorbed oxygen, absorbed superoxide ions, or adsorbed peroxide ions, or some combination of the three. The relative presence of each can also give some clue as to the lifetime of each species. A species with a very short lifetime can typically be modeled as having a steady-state concentration without introducing much error. This will greatly simplify calculations as it removes a variable from the overall coupled equations. Other methods, such as EIS, will be used to help discern if any particular reaction step is dominating or rate-limiting for the materials under study. This will be discerned from how the relative magnitudes of the resulting impedance loops vary as operating

conditions are changed. For example, when the partial pressure of a reacting species is lowered sufficiently, diffusion limitations should dominate the impedance performance. It is believed that significant changes in the operating conditions will affect the reaction mechanism and thus, experiments will be designed to determine the effect of operating conditions on the proposed mechanism. Knowledge of a species' presence and also the conditions under which a particular reaction step is dominating is will elucidate not only a mechanism for a materials system, but a particular mechanism under particular operating conditions as well.

As a first approximation, some types of reactions were assumed to be either infinitely fast or not occurring. Surface diffusion can oftentimes greatly complicate the mathematics of the system and in these investigations was not considered. Examples of some proposed reaction pathways to be studied on the cathode side are shown below in Equation (4.1).

$$O_{2(g)} \underset{des}{\overset{ads}{\rightleftarrows}} \left\{ \begin{array}{l} 2O_{(ad)} \underset{-2\left(V_O^{\bullet\bullet}+2e'\right)}{\overset{+2\left(V_O^{\bullet\bullet}+2e'\right)}{\rightleftarrows}} 2O_O^X \\ 2O_{(ad)} \underset{-2e'}{\overset{+2e'}{\rightleftarrows}} 2O_{(ad)}^{1-} \underset{-2\left(V_O^{\bullet\bullet}+e'\right)}{\overset{+2\left(V_O^{\bullet\bullet}+e'\right)}{\rightleftarrows}} 2O_O^X \\ O_{2(ad)} \underset{-e'}{\overset{+e'}{\rightleftarrows}} O_{2(ad)}^{1-} \underset{-e'}{\overset{+e'}{\rightleftarrows}} 2O_{(ad)}^{1-} \underset{-2\left(V_O^{\bullet\bullet}+e'\right)}{\overset{+2\left(V_O^{\bullet\bullet}+e'\right)}{\rightleftarrows}} 2O_O^X \\ O_{2(ad)}^{-} \underset{-\left(V_O^{\bullet\bullet}+e'\right)}{\overset{+\left(V_O^{\bullet\bullet}+e'\right)}{\rightleftarrows}} O_O^X + O_{(ad)} \underset{-e'}{\overset{+e'}{\rightleftarrows}} O_{(ad)}^{1-} \underset{-\left(V_O^{\bullet\bullet}+e'\right)}{\overset{V_O^{\bullet\bullet}+e'}{\rightleftarrows}} O_O^X \\ O_{2(ad)} \underset{rec}{\overset{dis}{\rightleftarrows}} 2O_{(ad)} \underset{-2e'}{\overset{+2e'}{\rightleftarrows}} 2O_{(ad)}^{1-} \underset{-2e'}{\overset{+2e'}{\rightleftarrows}} 2O_{(ad)}^{2-} \underset{-2V_O^{\bullet\bullet}}{\overset{+2V_O^{\bullet\bullet}}{\rightleftarrows}} 2O_O^X \end{array} \right\} \quad (4.1)$$

Equation (4.1) uses Kröger – Vink notation where *ad* are surface adsorption sites, $V_O^{\bullet\bullet}$ are oxygen vacancies, e' are electrons and O_O^X is an oxygen atom occupying an

oxygen site in the electrolyte. As seen above, even for the relatively simple reduction of oxygen, wide arrays of possible reaction pathways are present (and this is by no means exhaustive). A systematic approach was taken in proposing possible reaction pathways, adding complexity to the mechanism with each sequence. The numbers of various species present in the mechanisms were gradually increased.

Model development

To illustrate the model development procedure the second reaction mechanism in Equation (4.1) will be used to formulate mass and charge balances. The reaction mechanism is as follows:

$$O_{2,(g)} + 2ad \underset{k_{des}}{\overset{k_{ads}}{\rightleftarrows}} 2O_{ad} \tag{4.2}$$

$$O_{ad} + e' \underset{k_{\bar{2}}}{\overset{k_2}{\rightleftarrows}} O'_{ad} \tag{4.3}$$

$$O'_{ad} + e' + V_O^{\cdot\cdot} \underset{k_{\bar{3}}}{\overset{k_3}{\rightleftarrows}} O_O^X + ad \tag{4.4}$$

The rate constants are displayed for the adsorption/desorption and the forward and reverse electrochemical steps. In this mechanism, oxygen dissociatively adsorbs on the surface and is sequentially reduced before being incorporated into the GDC electrolyte. Surface diffusion is assumed to occur sufficiently fast and is thus not included.

In addition to the assumptions laid out in the previous section, the following additional assumptions were also made: (1) the concentrations of $V_O^{\cdot\cdot}$ and O_O^X will remain constant throughout the experiment, (2) adsorption/desorption rate constants are potential independent, (3) electrochemical rate constants are potential dependent (4) all rate constants are temperature dependent through an Arrhenius relationship and (5) the total

number of surface adsorption sites is constant and independent of the species adsorbed on the sites.

Charge transfer step rate constants are assumed to have an exponential dependence in potential and an Arrhenius type dependence in temperature such that[63, 64]:

$$k_i\left(T,E\right)=k_i\left(T\right)\exp\left(-\frac{\beta_i n_i F}{RT}E\right) \tag{4.5}$$

$$k_{\bar{i}}\left(T,E\right)=k_{\bar{i}}\left(T\right)\exp\left(\frac{\left(1-\beta_i\right)n_i F}{RT}E\right) \tag{4.6}$$

$$k_i\left(T\right)=k_{i0}\exp\left(-\frac{E_{ia}}{RT}\right) \tag{4.7}$$

where β_i ($0 \leq \beta_i \leq 1$) is the symmetry coefficient or sometimes called the transfer coefficient of step i and n_i are the number of electrons transferred in step i. F, R, and T have their usual meanings and E is the electrode potential such that,

$$E=E_{eq}+\eta \tag{4.8}$$

where E_{eq} is the equilibrium potential and η is the applied overpotential. Additionally, to better condition the problem at hand, fractional surface coverages will be used in place of concentrations.

$$\theta_1=\frac{\left[O_{ad}\right]}{\left[O_{ad}\right]+\left[O'_{ad}\right]+\left[ad\right]} \tag{4.9}$$

$$\theta_2=\frac{\left[O'_{ad}\right]}{\left[O_{ad}\right]+\left[O'_{ad}\right]+\left[ad\right]} \tag{4.10}$$

$$\Gamma=\left[O_{ad}\right]+\left[O'_{ad}\right]+\left[ad\right] \tag{4.11}$$

$$\left[ad\right]=\Gamma\left(1-\theta_1-\theta_2\right) \tag{4.12}$$

where Γ is the total number of adsorption sites.

Using the above relations, the following mass balance equations can be written:

$$\frac{d\theta_1}{dt} = 2k_{ads}(T)\,p_{O_2}\Gamma(1-\theta_1-\theta_2)^2 - 2k_{des}(T)\Gamma\theta_1^2 - k_2(T,E)\theta_1 + k_{\bar{2}}(T,E)\theta_2 \tag{4.13}$$

$$\frac{d\theta_2}{dt} = k_2(T,E)\theta_1 - k_{\bar{2}}(T,E)\theta_2 - k_3(T,E)\left[V_O^{\cdot\cdot}\right]\theta_2 + k_{\bar{3}}(T,E)\left[O_O^X\right](1-\theta_1-\theta_2) \tag{4.14}$$

The faradaic current density is expressed as a function of every electron transfer step as

$$\begin{aligned} i_F(T,E,p_{O_2}) &= -nAFr \\ &= FA\left[k_{\bar{2}}(T,E)\theta_2 - k_2(T,E)\theta_1\right] - \\ &\quad FA\left[k_3(T,E)\left[V_O^{\cdot\cdot}\right]\theta_2 + k_{\bar{3}}(T,E)\left[O_O^X\right](1-\theta_1-\theta_2)\right] \end{aligned} \tag{4.15}$$

Many parameters appear in Equations (4.13) - (4.15), some of which are known from the literature or experiments and some of which must be estimated from experimental data.

Equilibrium state

Under state-state conditions ($\eta = 0$ thus, $E = E_{eq}$) Equations (4.13) – (4.15) are all equal to zero. Thus, with appropriate values for the unknown constants, the steady-state values of surface coverage can be calculated. What follows next is the development of the equilibrium potential stemming from the condition that Equation (4.15) is equal to zero. At equilibrium, the rates of reactions (4.2) through (4.4) for the forward and reverse directions are equal. This gives a relationship between the steady-state surface coverages and the adsorption/desorption rate constants such that:

$$K(T) = \frac{k_{ads}(T)}{k_{des}(T)} = \frac{\theta_{1,eq}^2}{\left(1-\theta_{1,eq}^2-\theta_{2,eq}^2\right)^2 p_{O_2}} \tag{4.16}$$

where the *eq* subscript denotes the equilibrium condition and *K(T)* is the equilibrium coefficient. Additionally, the relationship between the fractional coverages of the equilibrium surface species is given by:

$$\theta_{1,eq} = \frac{k_{\bar{2}}\left(T, E_{eq}\right)}{k_2\left(T, E_{eq}\right)}\theta_{2,eq} \tag{4.17}$$

Upon setting Equation (4.15) equal to zero, substituting in Equations (4.16) and (4.17), and rearranging, the following expression is produced:

$$\frac{k_{\bar{2}}\left(T, E_{eq}\right)k_{\bar{3}}\left(T, E_{eq}\right)}{k_2\left(T, E_{eq}\right)k_2\left(T, E_{eq}\right)} = \frac{\left[V_O^{\bullet\bullet}\right]}{\left[O_O^X\right]}\sqrt{K(T)\,p_{O_2}} \tag{4.18}$$

The electrochemical rate constants can be separated into their temperature dependent and potential dependent portions according to Equations (4.5) and (4.6). Simplification of the resulting exponential terms leads to

$$\exp\left(\frac{2F}{RT}E_{eq}\right) = \frac{\left[V_O^{\bullet\bullet}\right]}{\left[O_O^X\right]}\frac{k_2(T)k_3(T)}{k_{\bar{2}}(T)k_{\bar{3}}(T)}\sqrt{K(T)\,p_{O_2}} \tag{4.19}$$

Taking the logarithm of both sides and separating all temperature and potential terms, leads to an equation of the Nernst form[63] such that:

$$\begin{aligned} E_{eq}\left(T, p_{O_2}\right) &= E_{eq}(T) + E_{eq}\left(p_{O_2}\right) \\ &= \frac{RT}{2F}\ln\left[\frac{\left[V_O^{\bullet\bullet}\right]}{\left[O_O^X\right]}\frac{k_2(T)k_3(T)}{k_{\bar{2}}(T)k_{\bar{3}}(T)}\sqrt{K(T)}\right] + \frac{RT}{4F}\ln p_{O_2} \end{aligned} \tag{4.20}$$

At the reference temperature, T°, and pressure, $p_{O_2}^\circ$, which is arbitrarily set at T° = 750°C and $p_{O_2}^\circ$ = 1 atm, E_{eq} is equal to zero. More directly, $E_{eq}(T^\circ) = 0$ and $E_{eq}(p_{O_2}^\circ) = 0$.

The above values for the reference state were chosen to aid in calculations, but it should be noted that the reference state can be arbitrarily set at any value, but once set, it is fixed. In this manner, both the electrode potential and the electrochemical rate constants can be defined relative to this reference state. Thus, Equation (4.20) can be rearranged into:

$$k_{\bar{2}}\left(T^{\circ}\right)=\frac{\left[V_O^{\bullet\bullet}\right]k_2\left(T^{\circ}\right)k_3\left(T^{\circ}\right)\sqrt{K\left(T^{\circ}\right)}}{\left[O_O^X\right]k_{\bar{3}}\left(T^{\circ}\right)} \tag{4.21}$$

such that the reverse electrochemical rate constant for step 2 can be defined relative to other terms in the expression.

Exchange current density

At steady-state when local equilibrium is assumed for all steps but the rate limiting step, the current can be expressed in a Butler-Volmer type expression such that[64]:

$$i_F\left(T,p_{O_2},\eta\right)=i_{0i}\left(T,p_{O_2}\right)\left[\exp\left(\frac{\alpha_a F}{RT}\eta\right)-\exp\left(-\frac{\alpha_c F}{RT}\eta\right)\right] \tag{4.22}$$

where i_{i0} is the exchange current density based on step i being the rate limiting step, and α_a and α_c are the real anodic and cathodic charge transfer coefficients, respectively. The charge transfer coefficients are defined based on the step chosen to be rate limiting, the number of electrons transferred during the rate limiting step, r, the number of times the rate limiting step must be repeated for all n electrons for the overall reaction (for oxygen reduction $n = 4$) to be transferred, ν, and the total number of electrons transferred before

and after the rate limiting step, γ_b and γ_a, respectively. The above leads to the following relations regarding the charge transfer coefficients:

$$\alpha_a = \frac{\gamma_a}{\nu} + r(1-\beta) \tag{4.23}$$

$$\alpha_c = \frac{\gamma_b}{\nu} + r\beta \tag{4.24}$$

$$\alpha_a + \alpha_b = \frac{n}{\nu} \tag{4.25}$$

The next step is to develop an expression for the exchange current density. Again, this relationship will be dependent upon the choice made for the rate limiting step. Thus, for the reaction mechanism defined by Equations (4.2) – (4.4), three expressions for i_0 are possible. The incorporation reaction, Equation (4.4), was chosen as rate limiting to detail the development of i_0. We will also note at temperatures not far from $T = T^\circ$ that $i_0\left(T, p_{O_2}\right) \approx i_0\left(T^\circ, p_{O_2}\right)$ [26].

Through several substitutions from Equations (4.16), (4.17), and (4.21), the faradaic current defined by Equation (4.15) can be expressed as

$$i_F\left(T^\circ, p_{O_2}, \eta\right) = FA\Gamma k_3\left(T^\circ\right)\left[V_O^{\bullet\bullet}\right] \times \left\{ \begin{array}{l} \dfrac{k_2\left(T^\circ\right)}{k_{\bar{2}}\left(T^\circ\right)}\sqrt{K\left(T^\circ\right)}\exp\left[\dfrac{(1-\beta_3)F}{RT}\left(E_{eq}+\eta\right)\right]\left(1-\theta_1-\theta_2\right) \\ -\exp\left[-\dfrac{\beta_3 F}{RT}\left(E_{eq}+\eta\right)\right]\theta_2 \end{array} \right. \tag{4.26}$$

At equilibrium, the surface concentrations take on their steady-state values of corresponding operating point defined by the temperature and the partial pressure of oxygen. We can define the steady-state surface concentrations as

$$\theta_{1,eq} = \frac{k_{\bar{2}}\left(T^{\circ}, E_{eq}\right)\sqrt{K\left(T^{\circ}\right)}p_{O_2}^{\frac{1}{2}}}{k_{\bar{2}}\left(T^{\circ}, E_{eq}\right) + k_{\bar{2}}\left(T^{\circ}, E_{eq}\right)\sqrt{K\left(T^{\circ}\right)}p_{O_2}^{\frac{1}{2}} + k_2\left(T^{\circ}, E_{eq}\right)\sqrt{K\left(T^{\circ}\right)}p_{O_2}^{\frac{1}{2}}} \tag{4.27}$$

$$\theta_{2,eq} = \frac{k_2\left(T^{\circ}, E_{eq}\right)\sqrt{K\left(T^{\circ}\right)}p_{O_2}^{\frac{1}{2}}}{k_{\bar{2}}\left(T^{\circ}, E_{eq}\right) + k_{\bar{2}}\left(T^{\circ}, E_{eq}\right)\sqrt{K\left(T^{\circ}\right)}p_{O_2}^{\frac{1}{2}} + k_2\left(T^{\circ}, E_{eq}\right)\sqrt{K\left(T^{\circ}\right)}p_{O_2}^{\frac{1}{2}}} \tag{4.28}$$

Additionally, under equilibrium conditions, $\eta = 0$, the net current through the cell is zero such that

$$i_{F3} = i_{03} = i_{03anodic} - i_{03cathodic} \tag{4.29}$$

where $i_{03anodic}$ and $i_{03cathodic}$ are the anodic and cathodic currents, respectively. Comparing this with Equation (4.26), it follows that

$$i_{03anodic} = FA\Gamma k_3\left(T^{\circ}\right)\left[V_O^{\cdot\cdot}\right]\frac{k_2\left(T^{\circ}\right)}{k_{\bar{2}}\left(T^{\circ}\right)}\sqrt{K\left(T^{\circ}\right)}\exp\left[\frac{\left(1-\beta_3\right)F}{RT}E_{eq}\right]\left(1-\theta_{1,eq}-\theta_{2,eq}\right) \tag{4.30}$$

$$i_{03cathodic} = FA\Gamma k_3\left(T^{\circ}\right)\left[V_O^{\cdot\cdot}\right]\exp\left(-\frac{\beta_3 F}{RT}E_{eq}\right)\theta_{2,eq} \tag{4.31}$$

The exchange current density can be calculated from the square root of the product of those two expressions

$$i_{03}\left(T, p_{O_2}\right) = \sqrt{i_{03anodic}\cdot i_{03cathodic}} \tag{4.32}$$

Sequential substitutions of Equations (4.20), (4.30), (4.27), (4.28) and (4.31) into Equation (4.32) lead to the following expression for the exchange current density, based on the third step in the reaction mechanism being rate limiting:

$$i_{03}\left(T^{\circ}, p_{O_2}\right) = \frac{FA\Gamma k_2\left(T^{\circ}\right)k_3\left(T^{\circ}\right)\left[V_O^{\cdot\cdot}\right]\sqrt{K\left(T^{\circ}\right)}p_{O_2}^{\frac{(1-\beta_3)}{4}}}{k_{\bar{2}}\left(T^{\circ}\right) + k_{\bar{2}}\left(T^{\circ}\right)\sqrt{K\left(T^{\circ}\right)}p_{O_2}^{\frac{1}{2}} + k_2\left(T^{\circ}\right)\sqrt{K\left(T^{\circ}\right)}p_{O_2}^{\frac{1}{4}}} \tag{4.33}$$

Examining Equation (4.33), it shows that if β_3 is equal to 0.5, a $p_{O_2}^{\frac{1}{8}}$ dependence of i_0 is seen at low fractional coverages of adsorbed intermediates. Several authors have shown various p_{O_2} dependencies of i_0 ranging from ⅛ to 1 [26, 34, 76, 97, 98]. Applying the relations from Equations (4.23) – (4.25), we can now rewrite the faradaic current as

$$i_{F3}\left(T^{\circ}, p_{O_2}, \eta\right) = i_{03}\left(T^{\circ}, p_{O_2}\right)\left\{\exp\left[\frac{\left(1-\beta_3\right)F}{RT}\eta\right] - \exp\left[-\frac{\left(1+\beta_3\right)F}{RT}\eta\right]\right\} \qquad (4.34)$$

The subscript *3* is placed on the current terms to signify that the relation is based upon the third step in the mechanism being rate limiting. This process can be repeated considering each step to be rate limiting and determining the exchange current density for that condition. It should be noted that when considering non-charge-transfer steps as rate limiting that the real charge transfer coefficients, α_a and α_c, have only symbolic significance as they assume that the charge transfer processes must occur infinitely fast.

Certain conditions may arise such that no one step is completely rate limiting, leading to competition between various reaction steps. For this case, the exchange current densities and Butler-Volmer expressions for each potential rate limiting step must first be determined. For *n* possible rate limiting steps total faradaic current is expressed as

$$i_{F,mixed}\left(T^{\circ}, p_{O_2}, \eta\right) = i_{anodic,mixed} - i_{cathodic,mixed} \qquad (4.35)$$

where the mixed anodic and cathodic current terms are summations of each term from the isolated rate limiting steps. For these mixed rate limiting step cases, it is assumed that the overall resulting current will be a sort of superposition of the individual currents. These terms are summed analogously to the way that resistors sum in circuit elements leading to

$$\frac{1}{i_{i,mixed}} = \frac{1}{i_{i1}} + \frac{1}{i_{i2}} + \cdots + \frac{1}{i_{in}} \qquad (4.36)$$

The various elements in Equation (4.35) can now be expressed as

$$i_{anodic,mixed} = \frac{i_{01}\exp\left(\frac{\alpha_{a1}F}{RT}\eta\right) i_{02}\exp\left(\frac{\alpha_{a2}F}{RT}\eta\right)\cdots i_{0n}\exp\left(\frac{\alpha_{an}F}{RT}\eta\right)}{i_{01}\exp\left(\frac{\alpha_{a1}F}{RT}\eta\right)+i_{02}\exp\left(\frac{\alpha_{a2}F}{RT}\eta\right)+\cdots+i_{0n}\exp\left(\frac{\alpha_{an}F}{RT}\eta\right)} \quad (4.37)$$

$$i_{cathodic,mixed} = \frac{i_{01}\exp\left(-\frac{\alpha_{c1}F}{RT}\eta\right) i_{02}\exp\left(-\frac{\alpha_{c2}F}{RT}\eta\right)\cdots i_{0n}\exp\left(-\frac{\alpha_{cn}F}{RT}\eta\right)}{i_{01}\exp\left(-\frac{\alpha_{c1}F}{RT}\eta\right)+i_{02}\exp\left(-\frac{\alpha_{c2}F}{RT}\eta\right)+\cdots+i_{0n}\exp\left(-\frac{\alpha_{cn}F}{RT}\eta\right)} \quad (4.38)$$

The expressions and other pertinent information resulting from the above derivations for the first two reaction mechanisms listed in Equation (4.1) are summarized in the tables below. The remaining mechanism expressions are not shown but follow similarly using the same derivation technique.

A reaction model is considered to be structurally identifiable if a unique set of parameters can be determined for a given input. Determining whether or not proposed reactions models are structurally identifiable has been studied by several authors [16, 26, 27, 90, 91, 99]. These authors have proven several of their reaction models to be structurally identifiable using techniques ranging from qualitative comparison to computer implementations of testing algorithms. The above references and the references therein provide a comprehensive view on identifiability and the reader is directed to them for a rigorous course and it relates to the problem at hand.

Table 4-1. Current-overpotential relations resulting from derivations relating to Mechanism 1 (see Equation (4.1))

Term	Expression
Nernst Expression	$E_{eq} = \frac{1}{2f}\ln\left[\frac{k_2(T)}{k_{\bar{2}}(T)}\frac{\left[V_O^{\cdot\cdot}\right]}{\left[O_O^X\right]}\sqrt{K(T)}\right] + \frac{1}{4f}\ln p_{O_2}$
Notation	$\Gamma = \left[O_{ad}\right] + \left[ad\right], \quad \theta = \frac{\left[O_{ad}\right]}{\Gamma}$
Mass Balances	$\frac{d\theta}{dt} = 2k_{ads}(T)\,p_{O_2}\Gamma(1-\theta)^2 - 2k_{des}(T)\Gamma\theta - k_2(T,E)\left[V_O^{\cdot\cdot}\right]\theta + k_{\bar{2}}(T,E)\left[O_O^X\right](1-\theta)$
Current Expression	$i_F\left(T, p_{O_2}, E\right) = 2FA\Gamma\left[k_{\bar{2}}(T,E)\left[O_O^X\right](1-\theta) - k_2(T,E)\left[V_O^{\cdot\cdot}\right]\theta\right]$
i_{01}	$i_{01}\left(T^\circ, p_{O_2}\right) = \frac{FA\Gamma^2\left[V_O^{\cdot\cdot}\right]\left[O_O^X\right]\sqrt{k_{ads}\left(T^\circ\right)k_{des}\left(T^\circ\right)}k_2\left(T^\circ\right)k_{\bar{2}}\left(T^\circ\right)p_{O_2}^{\frac{1}{8}}}{\left\{k_2\left(T^\circ\right)\left[V_O^{\cdot\cdot}\right] + k_{\bar{2}}\left(T^\circ\right)\left[O_O^X\right]p_{O_2}^{\frac{1}{4}}\right\}^2}$
i_{02}	$i_{02}\left(T^\circ, p_{O_2}\right) = \frac{2FA\Gamma k_2\left(T^\circ\right)\left[V_O^{\cdot\cdot}\right]\sqrt{K\left(T^\circ\right)}p_{O_2}^{\left(\frac{1}{2}-\frac{1}{2}\beta\right)}}{1+\sqrt{K\left(T^0\right)}p_{O_2}^{\frac{1}{2}}}$
i_{F1}	$i_{F1}\left(T^\circ, p_{O_2}, \eta\right) = i_{01}\left(T^\circ, p_{O_2}\right)\left[\exp\left(\frac{4F}{RT}\eta\right) - 1\right]$
i_{F2}	$i_{F2}\left(T^\circ, p_{O_2}, \eta\right) = i_{02}\left(T^\circ, p_{O_2}\right)\left\{\exp\left[\frac{2(1-\beta)F}{RT}\eta\right] - \exp\left[\frac{-2\beta F}{RT}\eta\right]\right\}$

Table 4-2. Current-overpotential relations resulting from derivations relating to Mechanism 2 (see Equation (4.1))

Term	Expression
Nernst Expression	$E_{eq}\left(T,p_{O_2}\right)=\frac{RT}{2F}\ln\left[\frac{k_2(T)k_3(T)}{k_{\bar{2}}(T)k_{\bar{3}}(T)}\frac{\left[V_O^{\cdot\cdot}\right]}{\left[O_O^X\right]}\sqrt{K(T)}\right]+\frac{RT}{4F}\ln p_{O_2}$
Notation	$\Gamma=\left[O_{ad}\right]+\left[O'_{ad}\right]+\left[ad\right],\quad \theta_1=\frac{\left[O_{ad}\right]}{\Gamma},\quad \theta_2=\frac{\left[O'_{ad}\right]}{\Gamma}$
Mass Balances	$\frac{d\theta_1}{dt}=2k_{ads}(T)\,p_{O_2}\Gamma\left(1-\theta_1-\theta_2\right)^2-2k_{des}(T)\Gamma\theta_1-k_2(T,E)\theta_1+k_{\bar{2}}(T,E)\theta_2$ $\frac{d\theta_2}{dt}=k_2(T,E)\theta_1-k_{\bar{2}}(T,E)\theta_2-k_3(T,E)\left[V_O^{\cdot\cdot}\right]\theta_2+\ k_{\bar{3}}(T,E)\left[O_O^X\right]\left(1-\theta_1-\theta_2\right)$
Current Expression	$i_F\left(T,p_{O_2},E\right)=FA\Gamma\left[k_{\bar{2}}(T,E)\theta_2-k_2(T,E)\theta_1+k_{\bar{3}}(T,E)\left[O_O^X\right]\left(1-\theta_1-\theta_2\right)-k_3(T,E)\left[V_O^{\cdot\cdot}\right]\theta_2\right]$

Table 4-3. Continuation of Table 4-2

Term	Expression
i_{01}	$i_{01}\left(T^{\circ},p_{O_2}\right)=\dfrac{F\Gamma^2\left[V_O^{\cdot\cdot}\right]\left[O_O^X\right]\sqrt{k_{ads}\left(T^{\circ}\right)k_{des}\left(T^{\circ}\right)}k_2\left(T^{\circ}\right)k_{\bar{2}}\left(T^{\circ}\right)k_3\left(T^{\circ}\right)k_{\bar{3}}\left(T^{\circ}\right)p_{O_2}}{\left\{k_2\left(T^{\circ}\right)k_3\left(T^{\circ}\right)\left[V_O^{\cdot\cdot}\right]+k_2\left(T^{\circ}\right)k_{\bar{3}}\left(T^{\circ}\right)\left[O_O^X\right]p_{O_2}^{\frac{1}{4}}+k_{\bar{2}}\left(T^{\circ}\right)k_{\bar{3}}\left(T^{\circ}\right)\left[O_O^X\right]p_{O_2}^{\frac{1}{2}}\right\}^2}$
i_{02}	$i_{02}\left(T^{\circ},p_{O_2}\right)=\dfrac{F\Gamma k_2\left(T^{\circ}\right)\left[V_O^{\cdot\cdot}\right]\sqrt{K\left(T^{\circ}\right)}p_{O_2}^{\frac{2-\beta_2}{4}}}{k_3\left(T^{\circ}\right)\left[V_O^{\cdot\cdot}\right]\left[1+\sqrt{K\left(T^{\circ}\right)}p_{O_2}^{\frac{1}{2}}\right]+k_{\bar{3}}\left(T^{\circ}\right)\left[O_O^X\right]p_{O_2}^{\frac{1}{4}}}$
i_{03}	$i_{03}\left(T^{\circ},p_{O_2}\right)=\dfrac{F\Gamma k_2\left(T^{\circ}\right)k_3\left(T^{\circ}\right)\sqrt{K\left(T^{\circ}\right)}\left[V_O^{\cdot\cdot}\right]p_{O_2}^{\frac{1-\beta_3}{4}}}{k_{\bar{2}}\left(T^{\circ}\right)+k_{\bar{2}}\left(T^{\circ}\right)\sqrt{K\left(T^{\circ}\right)}p_{O_2}^{\frac{1}{2}}+k_2\left(T^{\circ}\right)\sqrt{K\left(T^{\circ}\right)}p_{O_2}^{\frac{1}{4}}}$
i_{F1}	$i_{F1}\left(T^{\circ},p_{O_2},\eta\right)=i_{01}\left(T^{\circ},p_{O_2}\right)\left[\exp\left(\dfrac{4F}{RT}\eta\right)-1\right]$
i_{F2}	$i_{F2}\left(T^{\circ},p_{O_2},\eta\right)=i_{02}\left(T^{\circ},p_{O_2}\right)\left[\exp\left(\dfrac{(2-\beta_2)F}{RT}\eta\right)-\exp\left(-\dfrac{\beta_2F}{RT}\eta\right)\right]$
i_{F3}	$i_{F3}\left(T^{\circ},p_{O_2},\eta\right)=i_{03}\left(T^{\circ},p_{O_2}\right)\left[\exp\left(\dfrac{(1-\beta_3)F}{RT}\eta\right)-\exp\left(-\dfrac{(1+\beta_3)F}{RT}\eta\right)\right]$

Computer Implementation

Simulation environment

Several previous implementations of the state-space modeling approach as applied to reaction mechanism modeling as well as other mechanistic formulations have been completed, and the reader is referred to those studies for contrast and comparison [16, 25-27]. The methods and techniques used here are an extension to those previously developed. Previous studies made use of limiting assumptions (e.g. assuming that the surface was either fully covered $\theta \rightarrow 1$ or nearly empty, $\theta \rightarrow 0$), only considered relatively simple reaction mechanisms, or only took into account a single surface species.

The proposed reaction mechanisms were evaluated via numerical simulation, including the more simplified models that were solved for analytically. This allowed for a system of checks-and-balances to catch any possible early errors in the numerical simulations. These mechanisms were implemented in Matlab R14 with Simulink software running in a Windows XP or SUSE Linux 10.3 computer environment. Matlab is a technical computer language and development environment that is widely used to solve technical computing problems, such as differential equations, with great speed and accuracy[100]. Simulink is a relatively newer component that works with Matlab and allows for model-based design of dynamic systems through an interactive graphical interface[101]. These software packages allowed for rapid modeling of the state-space systems developed from the proposed reaction mechanisms.

The differential algebraic equations were represented in Simulink with block diagrams and, along with their transfer functions implemented in Matlab, a dynamic view of the system was acquired. Matlab is also uniquely apt at displaying the impedance

response of these dynamic systems. Several functions, included as part of the Matlab package, were used to determine these responses: *sim*, *linmod, trim, ss2tf* and *nyquist*. The function *sim* is used to simulate the block models developed in Simulink. This was used to obtain the steady-state values for the concentrations of the adsorbed intermediates. The function *linmod* was used to obtain linear models from systems of ordinary differential equations. This function was used in conjunction with the models developed in Simulink to obtain the matrices **A**, **B**, **C**, and **D** described previously by Equation (2.4).

When an external stimulus was applied to the system, such as an applied DC bias, then the function *trim* was used to determine the new steady state values of the system. Once the state-space description of the model was found, the function *nyquist* was used to show the frequency response of the model. Because the function *nyquist* required the LTI model to be in transfer function form, the function *ss2tf* was used to determine the transfer function, *H(s)*, of the model from the calculated matrices. *H(s)* is related to the state-space model coefficients by:

$$H(s) = \frac{num(s)}{den(s)} = \mathbf{C}(s\mathbf{I} - \mathbf{A})^{-1}\mathbf{B} + \mathbf{D} \tag{4.39}$$

where *s* is the Laplace variable. The full description of the above functions is included in the Matlab help programs[100].

Comparing state-space description with electrochemical parameters

In Chapter 2 the state-space modeling approach was detailed. In the previous section, a method to obtain the state-space parameters in the Matlab environment was

shown. Presently, we will show how the state-space parameters correspond to the electrochemical parameters one would obtain from impedance measurements.

The state-space description of the particular system under study was given previously in Equation (2.4), but for readability it is reproduced again below:

$$\begin{aligned} \dot{\theta} &= \mathbf{A}\theta + \mathbf{B}\eta \\ I_F &= \mathbf{C}\theta + \mathbf{D}\eta \end{aligned} \tag{4.40}$$

Impedance measurements are conducted in the frequency domain. The system equations above are in the time domain, but can be converted to the frequency domain through the use of Laplace transforms. Taking the Laplace transform of Equations (4.40) gives:

$$\begin{aligned} s\theta(s) &= \mathbf{A}\theta(s) + \mathbf{B}\eta(s) \\ I_F(s) &= \mathbf{C}\theta(s) + \mathbf{D}\eta(s) \end{aligned} \tag{4.41}$$

where s is the Laplace variable and is equal to $j\omega$. If we take the first equation in (4.41) and solve for q in term of h, we obtain

$$\theta(s) = (s\mathbf{I} - \mathbf{A})^{-1}\mathbf{B}\eta(s) \tag{4.42}$$

Substitution of Equation (4.42) into the bottom equation of (4.41) leads to an equation of the faradaic current in terms of the applied overpotential which additionally, is an expression of the impedance (or admittance) of the system.

$$\begin{aligned} &I_F(s) = \left[\mathbf{C}(s\mathbf{I} - \mathbf{A})^{-1}\mathbf{B} + \mathbf{D}\right]\eta(s) \\ &\text{or} \\ &\frac{I_F(s)}{\eta(s)} = \frac{1}{Z_F(s)} = Y_F(s) = \left[\mathbf{C}(s\mathbf{I} - \mathbf{A})^{-1}\mathbf{B} + \mathbf{D}\right] \end{aligned} \tag{4.43}$$

Where again, Z_F is the faradaic impedance and Y_F is the faradaic admittance function. Comparing Equation (4.43) with Equation (4.39), it follows that the impedance function can be obtained directly using the Matlab functions.

The charge transfer resistance was presented previously as the resistance to charge flowing across a boundary. More directly, for a given surface concentration of adsorbed intermediates, the charge transfer resistance is defined as the change in potential with current or

$$R_{ct} = \left(\frac{\partial \eta}{\partial i_F} \right)_{\theta} \tag{4.44}$$

Comparing this with Equation (4.40), it is seen that the charge transfer resistance is directly related to the state space parameters and equal to the inverse of the feed through matrix, **D**. Further study of Equation (4.43) shows that as ω increases, s increases, and a relationship between the charge transfer resistance and the admittance function is evident.

$$\lim_{\omega \to \infty} Y_F(\omega) = \mathbf{D} = \frac{1}{R_{ct}} \tag{4.45}$$

This implies that in a complex admittance (or impedance) plot, R_{ct} can be found at the intercept of the plot with the real axis at high frequencies.

The cell's total polarization resistance gives a measure of its performance and is typically defined as the intercept of the impedance plot with the real axis as the applied sinusoidal voltage approaches that of a DC signal (i.e. when ω approaches zero). Again, comparing this situation with Equation (4.43), we see that the polarization resistance defined in terms of the state-space parameters is

$$\lim_{\omega \to 0} Y_F(\omega) = \mathbf{D} - \mathbf{C}\mathbf{A}^{-1}\mathbf{B} = \frac{1}{R_P} \tag{4.46}$$

At frequencies intermediate of those at the low and high intercepts in the complex plane, the concentration polarization gives rise to an impedance factor stemming from the change in concentration of adsorbed intermediates. This concentration impedance gives

the characteristic shape of the impedance curve and describes its frequency response. Thus, the total impedance can be written as a sum of the charge transfer resistance that is seen at high frequencies and the concentration impedance Z_c that is seen at intermediate frequencies.

From Equation (4.43) we have

$$Z_F(s) = \frac{1}{\left[\mathbf{C}\left(s\mathbf{I}-\mathbf{A}\right)^{-1}\mathbf{B}+\mathbf{D}\right]} = 1 + \frac{1-\left[\mathbf{C}\left(s\mathbf{I}-\mathbf{A}\right)^{-1}\mathbf{B}+\mathbf{D}\right]}{\mathbf{C}\left(s\mathbf{I}-\mathbf{A}\right)^{-1}\mathbf{B}+\mathbf{D}} = \frac{\mathbf{1}}{\mathbf{D}}\left[1 - \frac{\mathbf{C}\left(s\mathbf{I}-\mathbf{A}\right)^{-1}\mathbf{B}}{\mathbf{C}\left(s\mathbf{I}-\mathbf{A}\right)^{-1}\mathbf{B}+\mathbf{D}}\right] \quad (4.47)$$

which can be further reduced to

$$Z_F(s) = R_t - R_t \frac{Y_F(s) - \mathbf{D}}{Y_F(s)} \quad (4.48)$$

By comparing Equation (4.48) with the previous reasoning that the total faradaic impedance is the sum of the charge transfer resistance and the concentration impedance, we arrive at the following expression for the concentration impedance

$$Z_c(s) = -R_t \frac{Y_F(s) - \mathbf{D}}{Y_F(s)} \quad (4.49)$$

The above expression tells us that at high frequencies, the impedance due to concentration polarization goes to zero (as $Y_F(s) \rightarrow \mathbf{D}$) and that at low frequencies (as $Z_F(s) \rightarrow R_p$) $Z_c(s)$ goes to

$$\lim_{\omega \to 0} Z_c(s) = -R_t \frac{\frac{1}{R_P} - \frac{1}{R_t}}{\frac{1}{R_P}} = R_P - R_t \quad (4.50)$$

The above expressions are summarized in saying that the impedance due to concentration polarization approaches zero at high frequencies and the difference between the polarization resistance and the charge transfer resistance at low frequencies.

Parameter Estimation

Many of the electrochemical parameters needed to successfully implement any simulation of a proposed oxygen reduction mechanism are unknown. Much of the literature data has been completed on metal surfaces and few, if any, experimental data exist on MIEC electrodes. Several factors have contributed to this including the difficulty with which to maintain a clean surface and that the stoichiometry of MIEC can vary with the atmosphere. Some data are available in the surface science literature and, when available, will be used to estimate parameters. Parameters not previously investigated will be estimated from comparison of experimental data with the simulation results. If no other means of obtaining parameters is available, as an initial guess, experimental parameters for oxygen reduction on platinum will be used in the simulations. An optimization procedure will be used to estimate the final kinetic data. The parameter estimation will proceed as follows:

1. Experimental impedance spectra and steady-state data are obtained under a variety of environmental conditions (i.e. temperature, oxygen partial pressure, applied overpotential, etc).
2. When available, surface science data will be used as a starting point for initial guesses for the kinetic parameters.
3. The proposed mechanisms will be simulated using the initial kinetic data.

4. A least squares fit of the simulated mechanisms with the experimental data will be performed using the Nelder-Mead simplex (direct search) method to find the minimum of the function.
5. Parameter estimation will be considered complete when the simulated plots pass the following criteria:
    a. Simulated impedance plots are as similar to the experimental data as possible.
    b. The system is stable and the estimated parameters are reasonable (i.e. surface coverage fractions are all below 1 and sum to less than one; rate constants are all positive in value).
    c. Upon changing the experimental conditions (temperature, oxygen partial pressure, etc), the simulation behaves similarly to the experimental data.

Simulation Results

In this section we present some of the results from one of the above reaction mechanism description models. Diagrams of the Simulink models for the various reaction mechanisms used during the simulations are shown in APPENDIX B. A table of parameters common to all simulations is given in Table 4-4.

Mechanism 1

Figure 4-1 shows the steady-state behavior for proposed reaction mechanism 1. Deviations are seen at large anodic overpotentials and although a different optimization

scheme can better correct this behavior, this would result in a much poorer match in the frequency domain. Other researchers have run into similar limitations in their modeling schemes and chose to improve their simulations by adding additional steps to their proposed reactions mechanisms such as[3]:

$$O_{2,gas} + V_O^{\bullet\bullet} + 3e' \underset{k_o}{\overset{k_r}{\rightleftharpoons}} O_O^X + O'_{ad} \tag{4.51}$$

Table 4-4. Parameters common to all simulations

Parameter	Value	Units	Reference
R	8.314	$J \cdot mol^{-1} \cdot K^{-1}$	Constant
A	$3.63 \cdot 10^{-7}$	m^2	This work
p_{O2}	$10^{-3} - 10^{2}$	atm	This work
T	923 – 1023	K	This work
T°	1023	K	This work
$\left[O_o^x\right]$	$6.5 \cdot 10^{4}$	$mol \cdot m^{-3}$	[102-104]
$\left[V_o^{\bullet\bullet}\right]$	$3.2 \cdot 10^{3}$	$mol \cdot m^{-3}$	[102-104]
k_{ads}°	$1 \cdot 10^{9}$	mechanism dependent	[20, 105]
k_{des}°	$1 \cdot 10^{11}$	$m^2 \cdot mol^{-1} \cdot s^{-1}$	[20, 105]
E_{ads}	40	$kJ \cdot mol^{-1}$	[20, 105]
E_{des}	200	$kJ \cdot mol^{-1}$	[20, 105]
Γ	$8 \cdot 10^{-6}$	$mol \cdot m^2$	[3, 106, 107]
C_{dl}	$1.26 \cdot 10^{-4}$	$F \cdot m^2$	This work

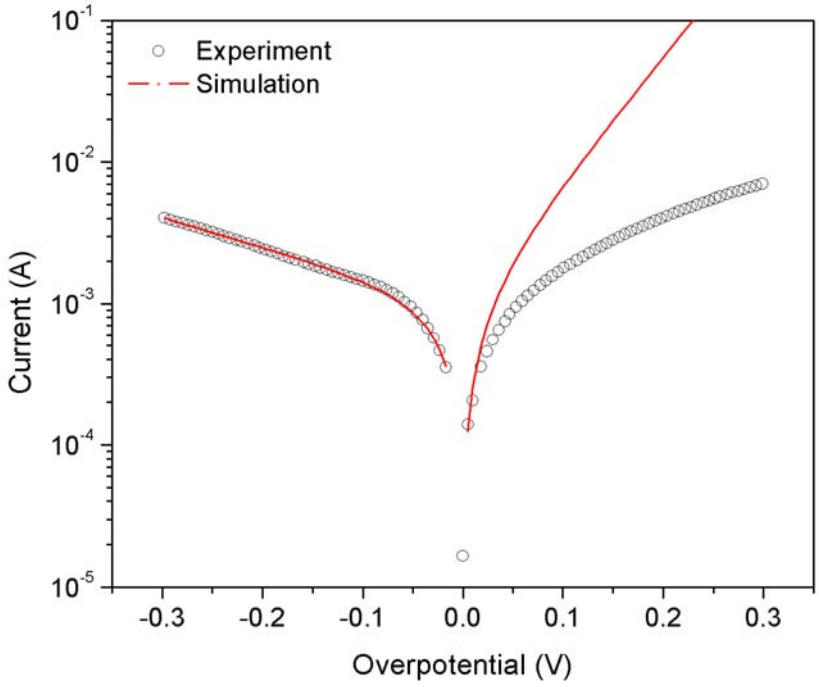

Figure 4-1. Comparison of experimental and simulated steady-state current-voltage data using proposed reaction mechanism 1. Data were simulated at 650°C and 1atm p_{O2}.

Although this improved the authors' simulations, the above reaction is highly unlikely to occur in reality as the simultaneous transfer of three electrons borders on a physical impossibility. Equation (4.51) should be looked at as an artifact of the simulation scheme and not as a viable step in the reaction mechanism.

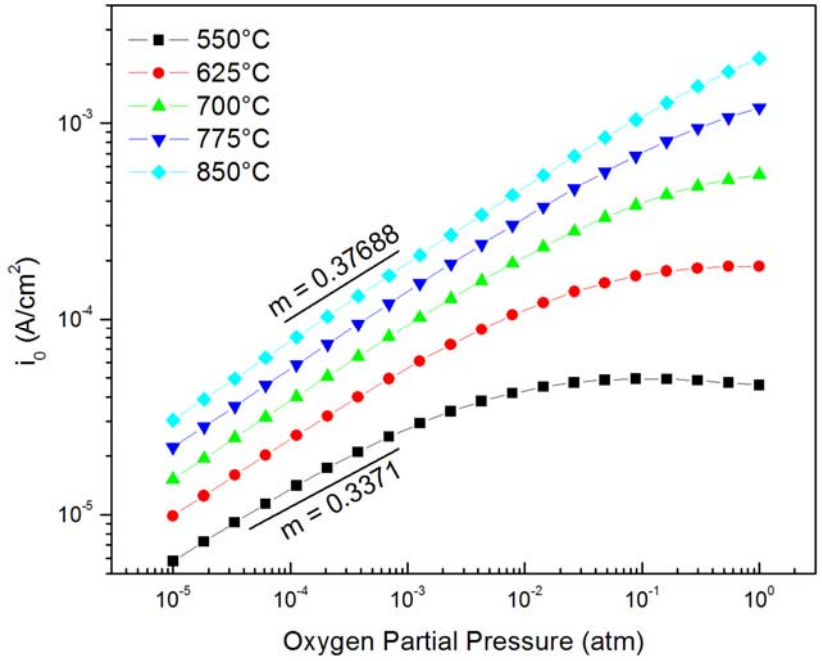

Figure 4-2. Isothermal plots showing the variation of the exchange current density with partial pressure of oxygen for mechanism 1

Figure 4-2 shows isothermal plots of the variation of the exchange current density with the partial pressure of oxygen. The model predicts an approximately $p_{O_2}^{\frac{3}{8}}$ dependence of the exchange current density with a maximum in i_0 being reached at lower temperatures and high pressures. Other authors studying similar systems have seen a partial pressure of oxygen dependence of about one-fourth[25, 92, 93]; however, many used several limiting conditions to arrive at their conclusions such as limiting their studies to either a nearly fully covered surface or a nearly empty surface.

In the previous chapter, experimental results showed a similar oxygen partial pressure dependence for the exchange current density ($\approx p_{O_2}^{0.35}$), though no maximum in i_0 was seen. The model predicts that this maximum is seen only at low temperatures

(around 550°C – 625°C), which were much lower than the ones used to gather the experimental data. Obtaining a full picture of the oxygen partial pressure dependence also required many simulated data points not completed in the experimental setup. Any curvature or maximum in the experimental data could easily have been mistaken for noise in the data. Additionally, no change in slope was seen in the model as was witnessed in the experimental data. Earlier, we attributed this change in slope to a change in the rate limiting step from dissociative adsorption to charge transfer. During the model formulation, it was assumed that the rate limiting step was the charge transfer step and thus remains so even at lower temperatures.

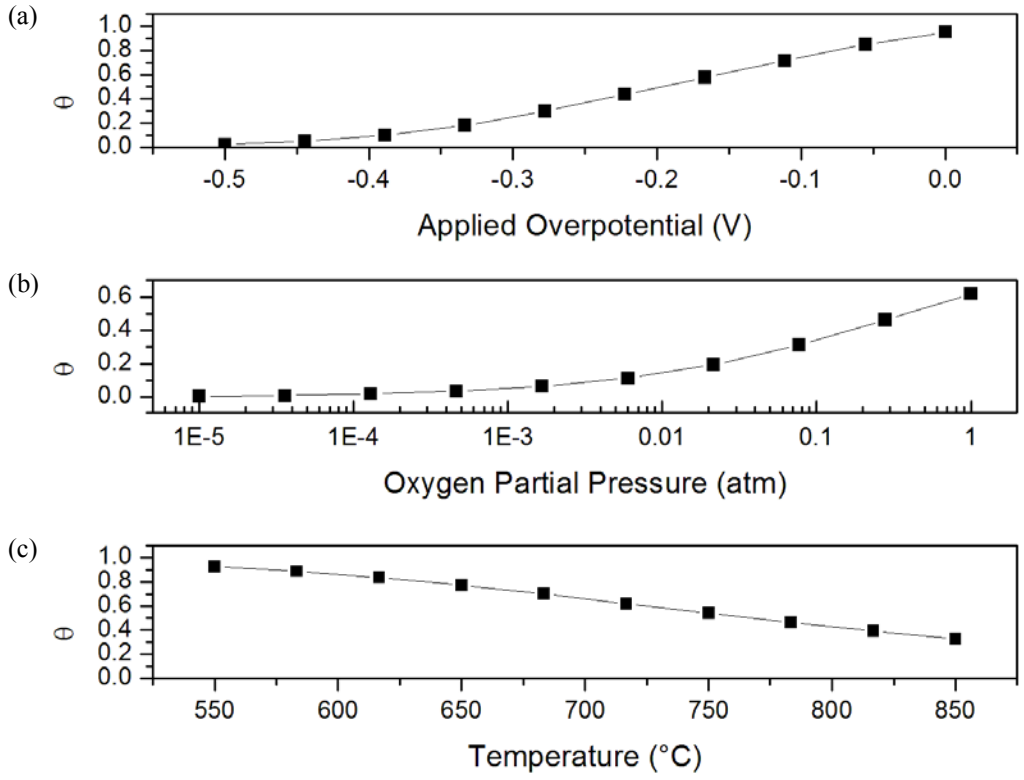

Figure 4-3. Changes in the equilibrium surface concentrations of the adsorbed intermediates for mechanism 1 as the (a) applied overpotential (700°C and in air), (b) oxygen partial pressure (716°C and 0 mV applied overpotential) and (c) temperature (air and 0 mV applied overpotential) are varied

Figure 4-3 shows variation in the equilibrium surface concentrations of the adsorbed intermediates for mechanism 1 as various parameters are changed. The simulation predicts that mass transport issues may arise, due to the surface coverage going to zero, as the temperature is decreased, the partial pressure of oxygen is decreased or a large cathodic bias is applied. These predictions all follow what we would expect in reality as the temperature is decreased, the likelihood of surface impingement is increased and the likelihood that the molecules have sufficient thermal energy to desorb decreases, thus the surface concentration should increase. Similarly, as the partial pressure of oxygen is decreased, the number of molecules available to adsorb to the surface decreases and thus, the surface concentration of adsorbed species should decrease. Applying a cathodic bias to the electrode helps to facilitate the TPB reaction, consuming more adsorbed species when the other operating variables are kept constant, thus, the surface coverage should decrease.

The impedance response of mechanism 1 is shown in Figure 4-4. Four parameters were estimated to simulate the impedance data, the apparent charge transfer coefficient for the charge transfer step, β, the activation energies for the forward and reverse charge transfer steps, and the temperature and potential independent forward rate constant for the charge transfer step, k_{20}. These values are summarized in Table 4-5.

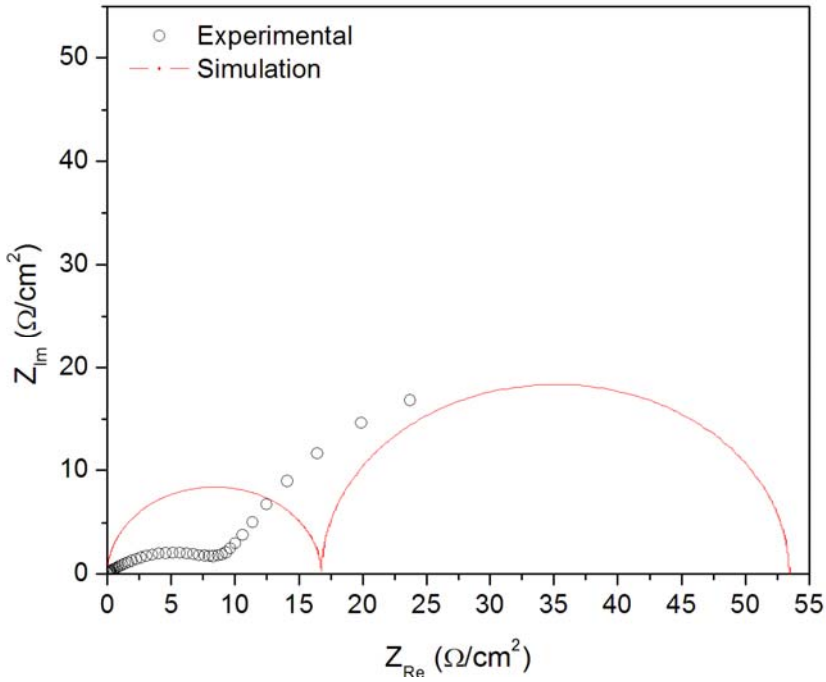

Figure 4-4. Comparison of experimental and simulated EIS spectra of mechanism 1 for 650°C and 1 atm p_{O2}

Table 4-5. Estimated parameters for mechanism 1

Parameter	Estimated Value	Units
β	0.1924	
E_2	121.3	kJ·mol^{-1}
$E_{\bar{2}}$	137.5	kJ·mol^{-1}
k_{20}	$1.5927 \cdot 10^6$	m^3·s^{-1}·mol^{-1}

Mechanism 1 simulated the main components of the impedance spectra fairly well (i.e. the number of impedance loops and the polarization resistance); however, the intermediate impedance was not simulated as well. The main reason for this inconsistency arises from the drastic departure from ideality that the experimental data takes. The high frequency loop in the experimental data is highly depressed and elongated. A possible cause of this is competition from surface diffusion that distorts the overall shape of the impedance spectrum. Diffusive effects were not taken into account in

mechanism 1 and thus, deviations occur in both the Tafel plots and the intermediate impedance region.

The system was found to be stable in that the initial guesses for the simulation parameters did not greatly affect the final estimated parameter values. This mechanism benefited in that a relatively small number of parameters had to be fit, minimizing the possibility of the falling into a local minimum. Comparison with the limited literature data for comparable systems shows that the estimated rate constants are of same order of magnitude.

Shown below are the temperature and oxygen partial pressure dependencies for the EIS spectra based on mechanism 1.

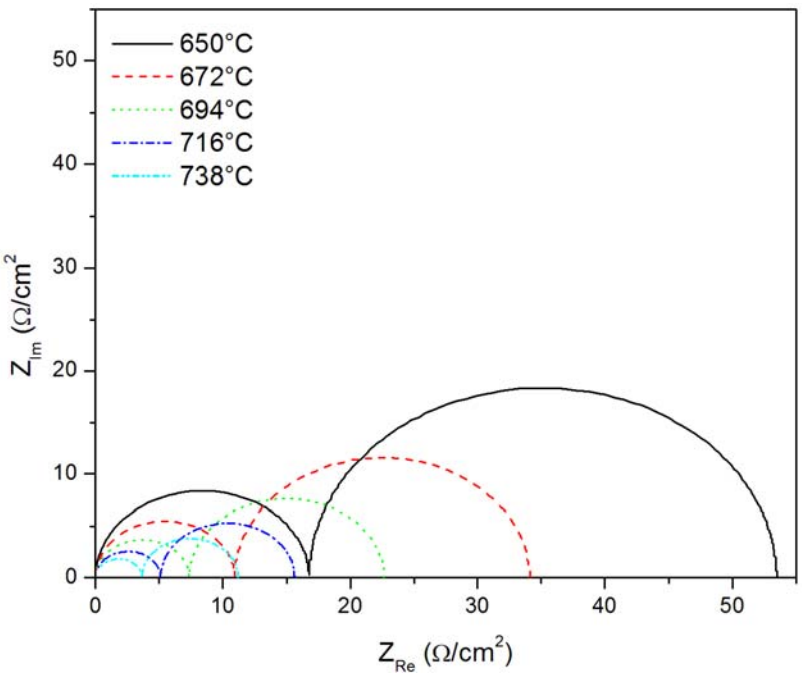

Figure 4-5. Temperature dependence of EIS spectra for mechanism 1. Data were simulated at 1 atm partial pressure of oxygen and 0 mV of applied DC bias.

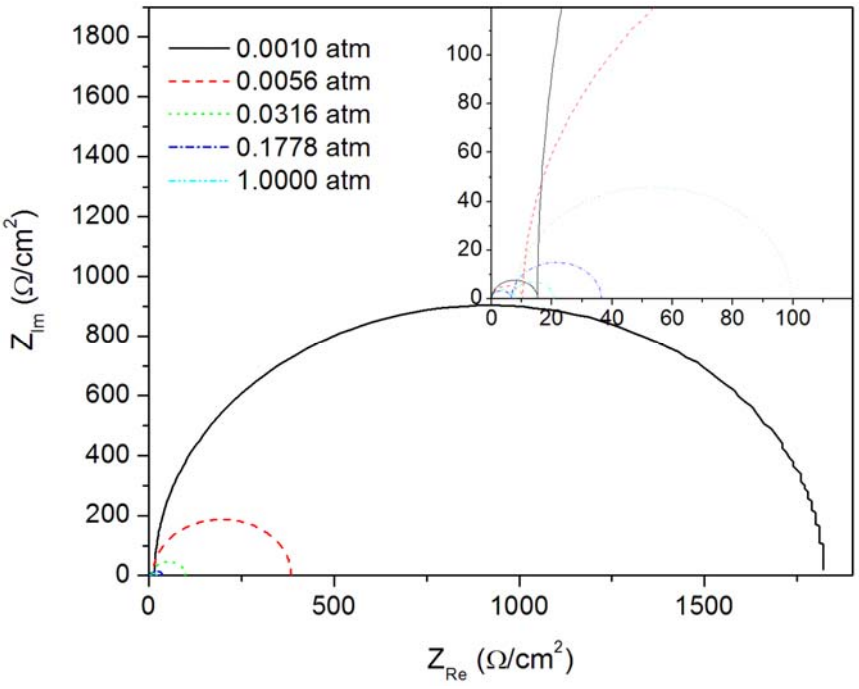

Figure 4-6. Pressure dependence of EIS spectra for mechanism 1. Data were simulated at a temperature of 700°C and 0 mV of applied DC bias.

The simulated data behave as expected. As temperature increases, the impedance for all processes decreases; thus, each of the two observed loops for each spectrum decrease in size similarly as the temperature increases. This arises from the assumed Arrhenius relationship of all rate constants in the simulation. Observing the change with partial pressure of oxygen, we see an asymmetric change in the two loops. Although both loops increase with decreasing oxygen partial pressure, the impedance of the low frequency loop increases at a much faster rate than that of the high frequency loop resulting in a change from approximately 1:2 (width of the high frequency loop to that of the low frequency loop) to approximately 1:100 as the oxygen partial pressure is varied from 1 atm to 0.001 atm. This asymmetric change leads us to assign the low frequency loop to the adsorption process (step 1) rather than the charge transfer process.

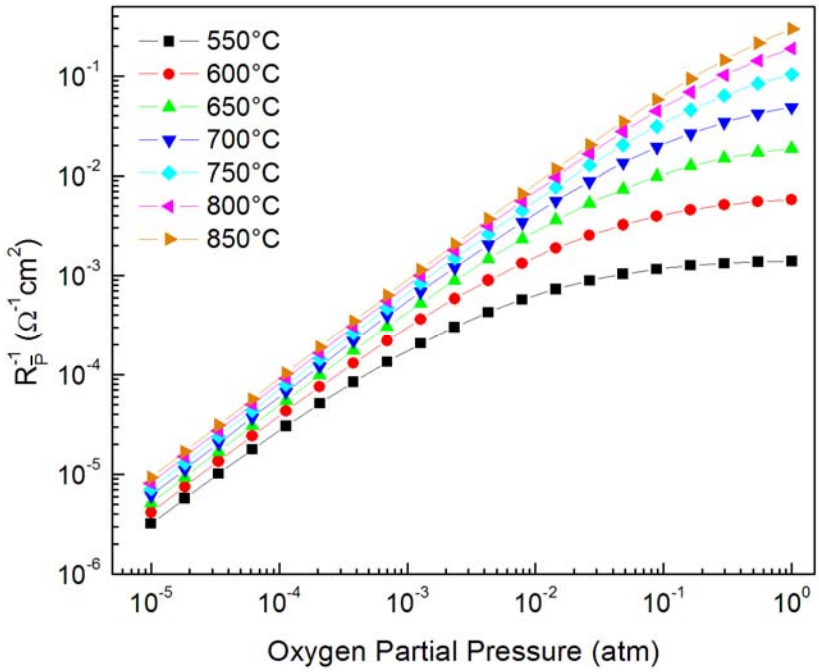

Figure 4-7. Isothermal curves of simulated performance data for mechanism 1 as a function of oxygen partial pressure

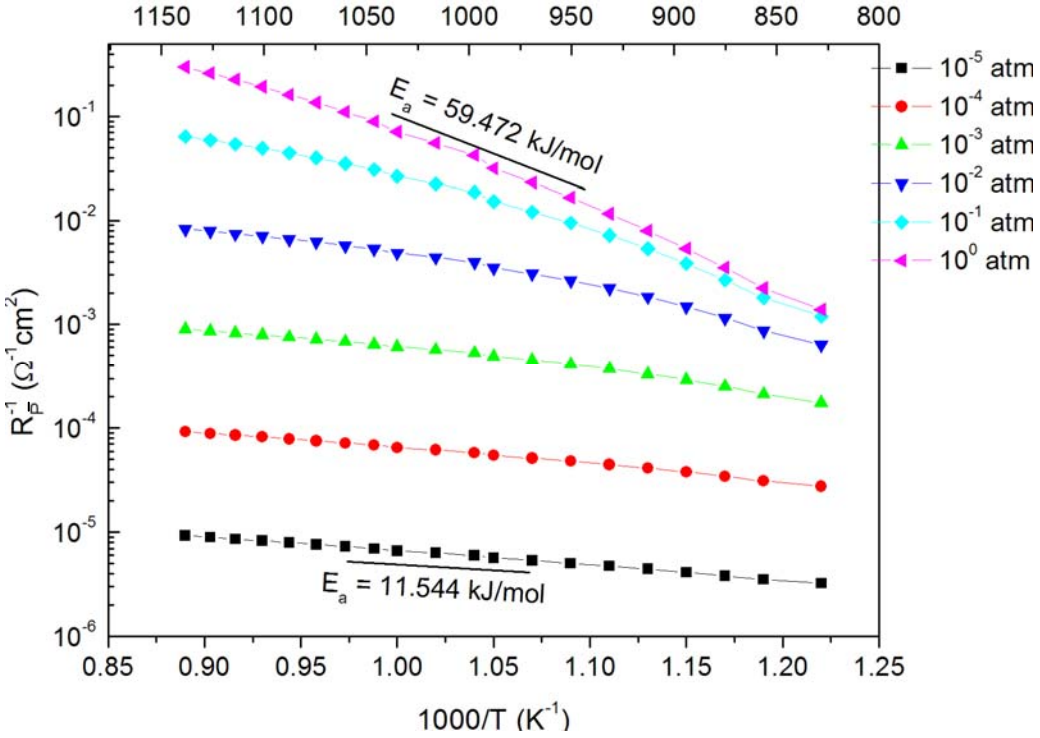

Figure 4-8. Isobaric Arrhenius plot of the simulated area specific polarization resistance for mechanism 1

The simulated area specific polarization resistance as a function of pressure and temperature for mechanism 1 are shown in Figure 4-7 and Figure 4-8, respectively. Similarly to the simulated exchange current density above, the simulated inverse polarization resistance exhibits trends that could not be seen in the experimental data due to the limited scope of available testing conditions. In the region of low temperatures and high oxygen partial pressures, one would not expect to see any mass transport limitations as the surface should be nearly covered with adsorbed intermediates. Thus, for a given temperature, further increases in the oxygen partial pressure should not affect the polarization resistance. The simulated data shows this well, as the plots in this region flatten out with further oxygen partial pressure increases.

The results from the simulated Arrhenius plots also agree well with the experimental data shown Figure 3-40. Figure 4-8 also shows a trend of decreasing activation energy with decreasing oxygen partial pressure. Additionally, the overall magnitude of the total activation energy favors well with the experiment value obtained under the same conditions.

Mechanism 2

Figure 4-9 shows a comparison of the experimental and the simulated steady-state current-voltage data for mechanism 2. A better overall fit to the experimental data was achieved with this mechanism than that for mechanism 1; however, deviations are still seen. The main source of these deviations seems to stem from the error in the experimental data. When determining the exchange current density from the Tafel analysis, one should obtain the same value whether using the linear sections of the anodic

or the cathodic side of the plot. That is, a linear fit of both sides should intersect the zero overpotential line at the same current value (this value determines the exchange current density). However, when this method is applied to the experimental data (see Figure 4-10), the lines do not intersect at zero overpotential. These deviations from ideality can arise from polarizing the electrode during testing, artifacts from diffusion processes or possible remnant charging of the electrode. While the slopes of the each segment of the simulated data are constrained to a mathematical relationship, this relationship is not seen experimentally causing deviations between the two to occur.

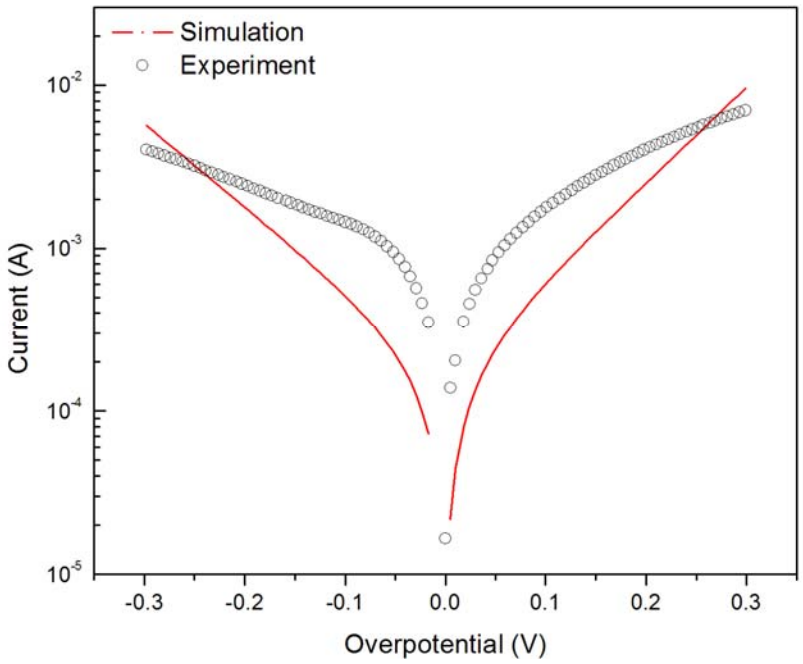

Figure 4-9. Comparison of experimental and simulated steady-state current-voltage data using proposed reaction mechanism 2. Data were simulated at 650°C and 1atm p_{O2}.

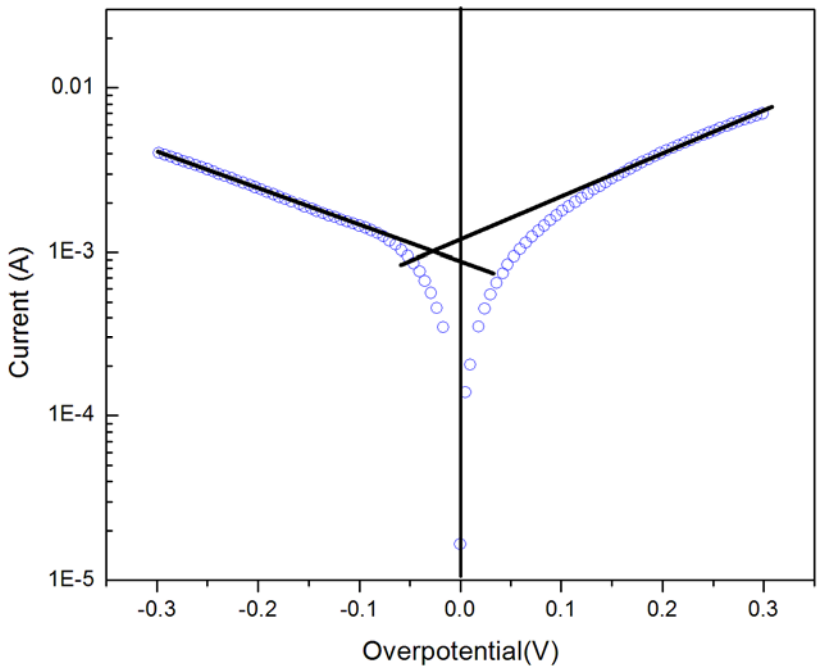

Figure 4-10. Tafel analysis of the experimental dataset shown previously. Analysis shows the deviation from ideal behavior as the linear sections do not intersect at zero overpotential.

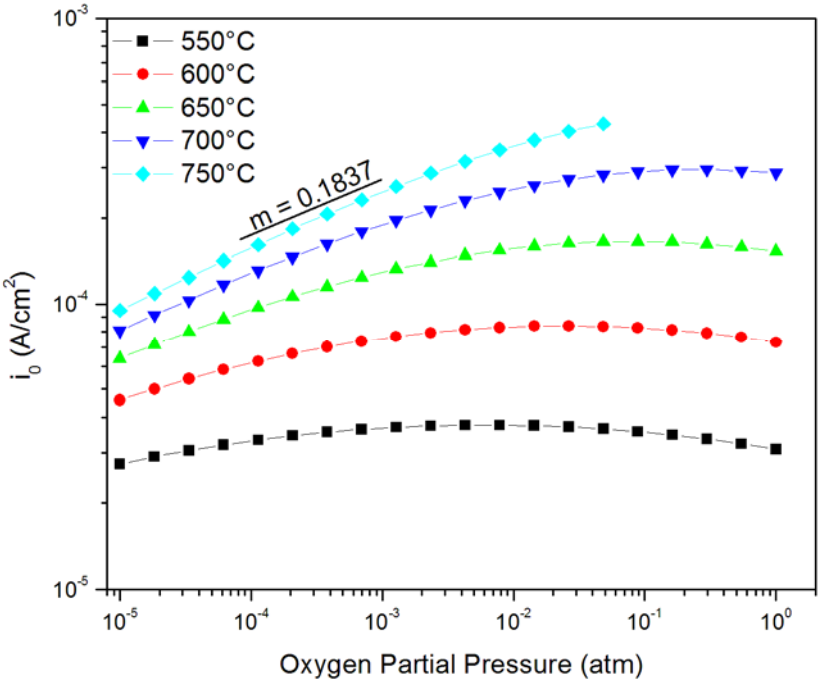

Figure 4-11. Isothermal plots showing the variation of the exchange current density with partial pressure of oxygen for mechanism 2

Figure 4-11 shows isothermal plots of the variation of the exchange current density with the partial pressure of oxygen. The model predicts an approximately $p_{O_2}^{0.18}$ dependence of the exchange current density with a maximum in i_0 being reached at lower temperatures and high pressures. In the previous chapter, experimental results showed a similar oxygen partial pressure dependence for the exchange current density ($\approx p_{O_2}^{0.19}$) at higher pressures, though no maximum in i_0 was seen. Correspondingly, this suggests that the estimated parameters for mechanism 2 would lead to adsorption or diffusion limited kinetics rather than the charge transfer limited kinetics seen in mechanism 1. For the experimental data it was concluded that a change in mechanism or rate limiting step occurred as the oxygen partial pressure was varied. From the insights gained during the steady-state simulations of mechanisms 1 and 2, it seems appropriate that each mechanism act over a particular oxygen partial pressure range. This is accomplished via the method described using Equation (4.36).

The impedance response of mechanism 2 is shown in Figure 4-12 (Nyquist plot) and Figure 4-13 (Bode plot). Several parameters were estimated to simulate the impedance data, and are summarized in Table 4-6.

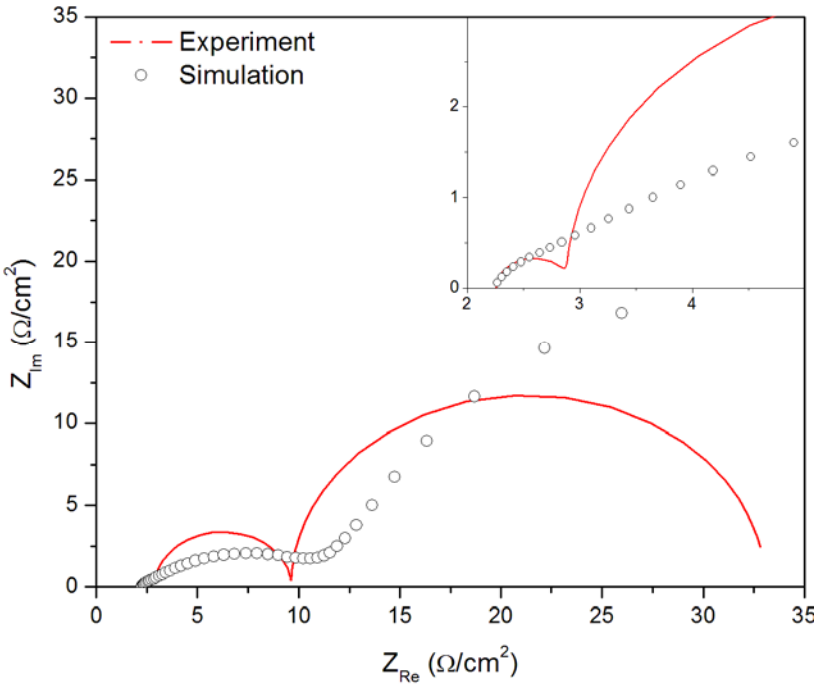

Figure 4-12. Comparison of experimental and simulated EIS spectra of mechanism 2 for 650°C and 1 atm p_{O2} shown in Nyquist plot format

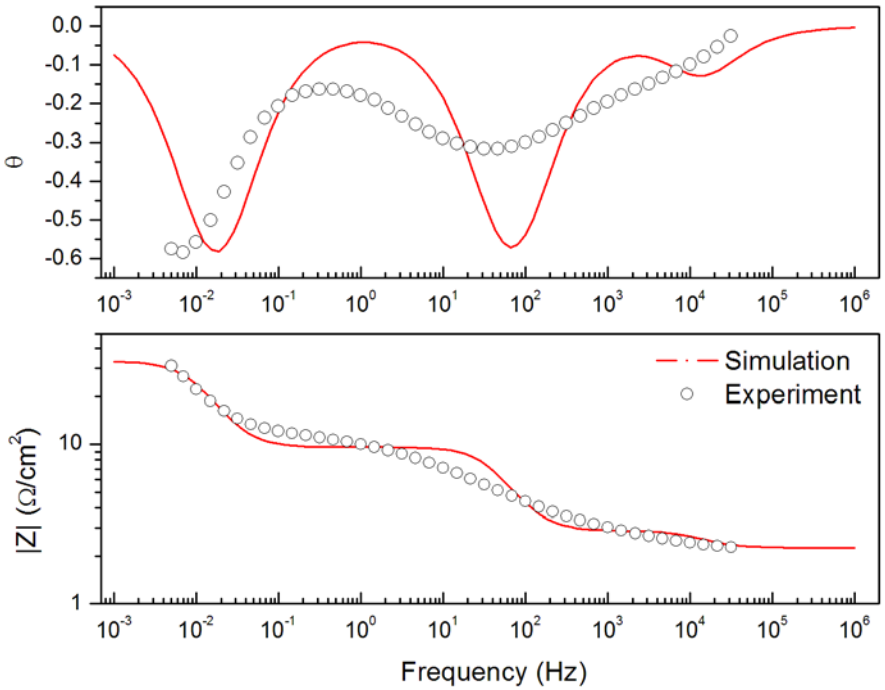

Figure 4-13. Comparison of experimental and simulated EIS spectra of mechanism 2 for 650°C and 1 atm p_{O2} shown in Bode plot format

Table 4-6. Estimated parameters for mechanism 2

Parameter	Estimated Value	Units
β_2	0.8501	
β_3	0.5932	
E_2	110.7	kJ·mol^{-1}
$E_{\bar{2}}$	135.3	kJ·mol^{-1}
E_3	125.5	kJ·mol^{-1}
$E_{\bar{3}}$	135.3	kJ·mol^{-1}
k_{20}	$4.8795 \cdot 10^{9}$	m^3·s^{-1}·mol^{-1}
$k_{\bar{2}0}$	$2.8265 \cdot 10^{6}$	m^3·s^{-1}·mol^{-1}
k_{30}	$5.0705 \cdot 10^{-3}$	m^3·s^{-1}·mol^{-1}

Mechanism 2 simulated the main components of the impedance spectra fairly well (i.e. the number of impedance loops and the polarization resistance). Additionally, the intermediate impedance was found to have a much better match with the experimental data than in mechanism 1. Looking at the frequency comparison, Figure 4-13, we note that the model reproduces all the main characteristics of the experimental data. We also note that the processes in the simulated data seem to be occurring at slightly higher frequencies than the experimental data, as shown by the shift in the phase angle versus frequency plot. Again, as with mechanism 1, diffusive effects were not taken into account and thus, deviations occur in both the Tafel plots and the intermediate impedance region. As with mechanism 1, this system was found to be stable in that the initial guesses for the simulation parameters did not greatly affect the final estimated parameter values.

Shown below are the temperature and oxygen partial pressure dependencies for the EIS spectra based on mechanism 2.

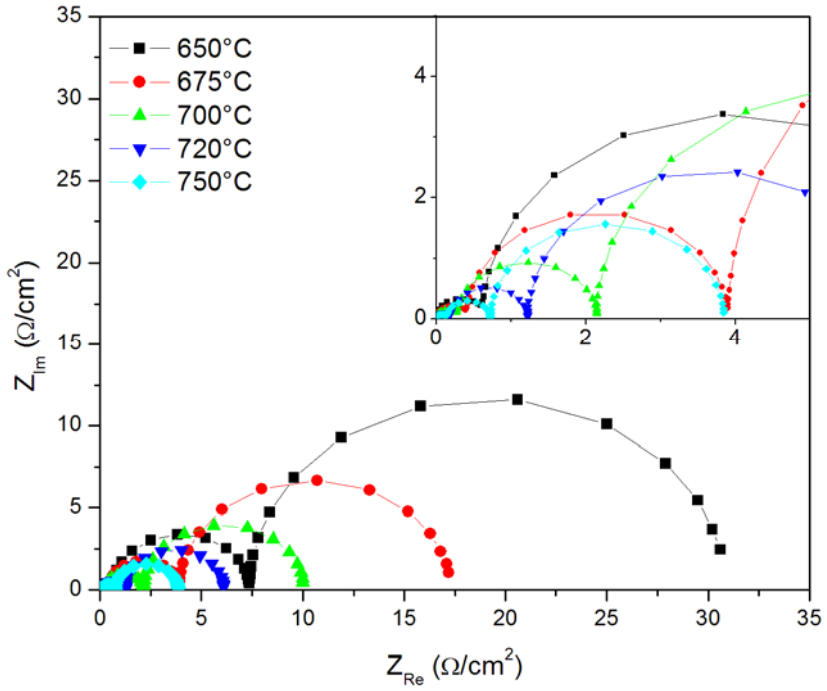

Figure 4-14. Temperature dependence of EIS spectra for mechanism 2. Data were simulated at 1 atm partial pressure of oxygen and 0 mV of applied DC bias.

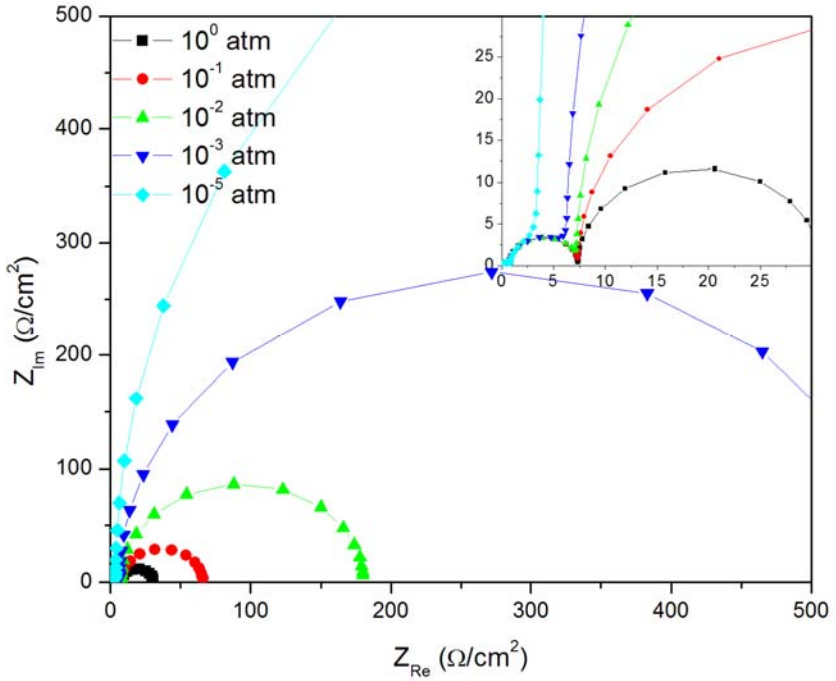

Figure 4-15. Pressure dependence of EIS spectra for mechanism 2. Data were simulated at a temperature of 700°C and 0 mV of applied DC bias.

The simulated data behave as expected. As temperature increases, the impedance for all processes decreases; thus, each of the observed loops for each spectrum decrease in size similarly as the temperature increases. This arises from the assumed Arrhenius relationship of all rate constants in the simulation. Observing the change with partial pressure of oxygen, we see an asymmetric change in the loops. While the magnitude of the high frequency loops remain fairly constant with increasing oxygen partial pressure, the impedance of the low frequency loop increases dramatically as the oxygen partial pressure is varied from 1 atm to 0.001 atm. This asymmetric change leads us to assign the low frequency loop to the adsorption process (step 1) rather than the charge transfer process.

The simulated area specific polarization resistance as a function of pressure and temperature for mechanism 1 are shown in Figure 4-16 and Figure 4-17, respectively. The results are similar to those obtained in mechanism 1. Figure 4-17 also shows a trend of decreasing activation energy with decreasing oxygen partial pressure, but less of a dependence as seen with mechanism 1. Additionally, the overall magnitude of the total activation energy appears to be slightly higher than the experiment value obtained under the same conditions.

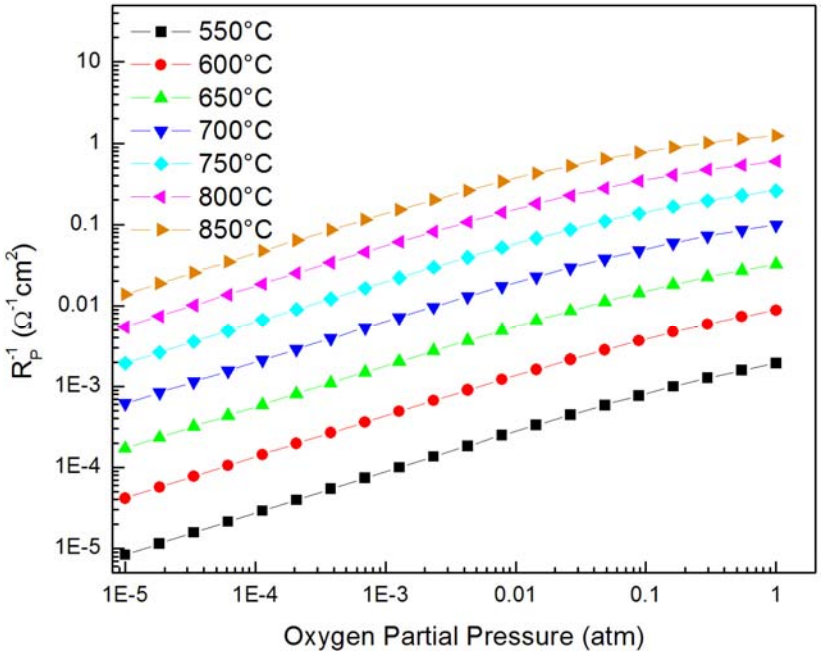

Figure 4-16. Isothermal curves of simulated performance data for mechanism 2 as a function of oxygen partial pressure

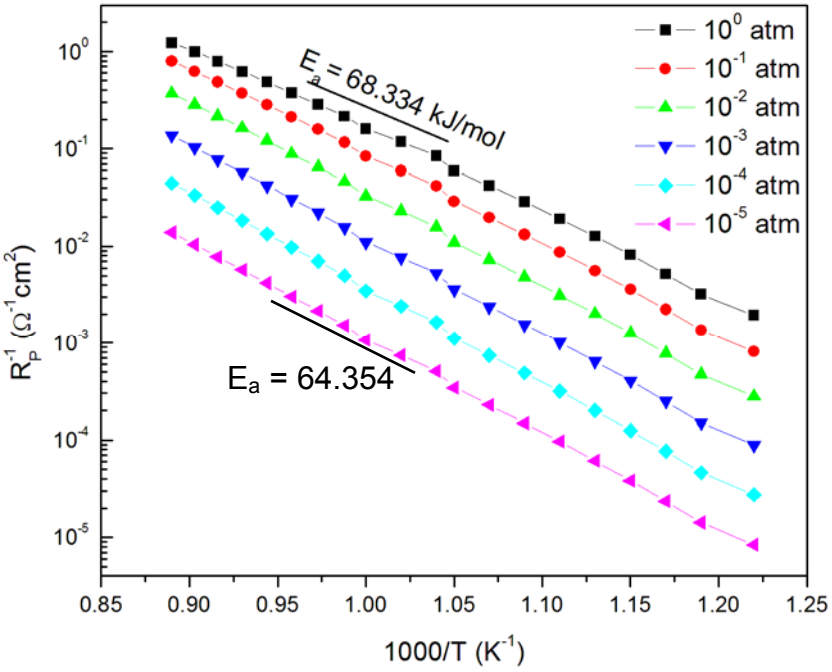

Figure 4-17. Isobaric Arrhenius plot of the simulated area specific polarization resistance for mechanism 2

Conclusions

A method for deriving the electrochemical properties from proposed reaction mechanisms was presented. State-space modeling is a robust approach to addressing these particular types of problems due to its relative ease of implementation and ability to efficiently handle large systems of differential algebraic equations. This method combines theoretical development with experimental results to predict the electrochemical performance data. The simulations agreed well the experimental data and allowed for testing of operating conditions not easily reproducible in the lab (e.g. precise control and differentiation of low oxygen partial pressures). Additionally, it was shown how the method could be used to estimate kinetic parameters not readily available.

Several limitations to the state-space formulations do exist, however. Simulations produced will only be as precise as the theoretical electrochemical development behind them. If some effects are poorly understood, they may not be included in the mechanism formulation; thus, many artifacts witnessed during experimental data collection (e.g. depression or distortion of the semicircles in the Nyquist plots) will not be seen in the simulation. Additionally, while there is great power in being able to estimate some kinetic parameters from this approach, simulations can become unstable when trying to estimate too many parameters at once. This leads to a greater chance of falling into local minima in the simulation space and having the optimization not converge. Because of this, the simulation will be much more dependent upon the initial values for those parameters. Lastly, due to the large number of possible reaction mechanisms, it is crucial to have some prior insight into the processes occurring at the surface under study. This

will eliminate the need to cover all possible reaction pathways and allow one to focus only on the feasible ones.

Like any simulation, the results obtained will be much more meaningful and applicable the more accurate the available experimental data. Combining this approach with experimental surface science and spectroscopic data will give the researcher a powerful tool for furthering their understanding of the electrode processes.

CHAPTER 5

CONCLUSIONS AND FUTURE WORK

Dense Composite Electrodes

In this study, we have developed a dense $La_{0.85}Sr_{0.15}MnO_{3-\delta}$ (LSM) – $Ce_{0.9}Gd_{0.1}O_{1.95}$ (GDC) composite electrode system for the study of surface modification of cathodes. The LSM and GDC grains in the composite were well defined and distinguished using EDX. This composite system provides some unique advantages to investigating cathodic reactions. First, all the triple phase boundaries are on the surface of the dense composite and are well defined through ceramic processing. Many of the problems associated with kinetic studies on porous SOFC electrodes are avoided. Second, all potential electrochemical reactions will occur on the open surface, making them more accessible to the application of various characterization techniques (such as SEM, Raman, micro-impedance spectroscopy). Third, it is possible to quantitatively correlate the cell performance and degradation with the specific triple phase boundary (TPB) length/area per unit surface area. LSM is selected here because it is a primarily electronic conductor whose ionic conductivity is typically negligible. In this case, it is rea sonable to assume that the electrochemical processes will only take place along the TPB area.

The specific three-phase boundary (TPB) length per unit electrode surface area was systematically controlled by adjusting the LSM to GDC volume ratio of the composite from 40% up to 70%. The TPB length for each tested sample was determined through stereological techniques and used to correlate the cell performance and degradation with the specific TPB length per unit surface area.

Overlapping Spheres Percolation Model

An overlapping spheres percolation model was developed to estimate the activity of the TPB lines on the surface of the dense composite electrodes developed. The model suggested that the majority of the TPB lines would be active and the length of those lines maximized if the volume percent of the electrolyte material was kept in the range of 47 – 57%. Additionally, other insights into the processing conditions to maximize the amount of active TPB length were garnered from the both the stereology calculations and the percolation simulations. These included (1) the particle size of the electrolyte phase should be as small as possible to maximize the amount of TPB length, (2) the particle size distribution should be as narrow as possible, and (3) grain growth of the electrolyte phase should be discouraged, but sintering of the second phase (LSM in this case) should be encouraged to improve overall densification (a requirement for the composite electrode) and to maximize the contact area (TPB) between the two phases.

Electrochemical Performance of the Dense Composites

Steady-state current voltage measurements as well as electrochemical impedance measurements on numerous samples under various environmental conditions were completed. The apparent activation energy for the reduction reaction was found to lie somewhere between 31 kJ/mol and 41 kJ/mol depending upon the experiment conditions. The exchange current density was found to vary with the partial pressure of oxygen differently over two separate regions. At low partial pressures, i_0 had an approximately $p_{O_2}^{0.17}$ dependence and at low partial pressures, i_0 had an approximately $p_{O_2}^{0.35}$ dependence.

This leads to the conclusion that a change in the rate limiting step occurs over this range. The experiments suggested that at high oxygen partial pressures, low temperatures and application of cathodic overpotentials leads to an adsorption or diffusion limited reaction. Conversely, low oxygen partial pressures, high temperatures and no applied bias leads to a charge transfer controlled reaction.

Electrochemical Model Development

A method for deriving the electrochemical properties from proposed reaction mechanisms was presented. This method combined theoretical development with experimental results to predict electrochemical performance data and was also used to estimate kinetic parameters not readily available. The trends exhibited during the simulations agreed well with those seen in the experimental data. Additionally, simulating conditions not readily reproducible in the lab (e.g. very low oxygen partial pressures or application of large overpotentials) led to further trends and insight into the intricacies of the reaction mechanisms.

Future Work

Future work using this composite system includes testing samples with modified surface characteristics (i.e. sputtered LSM, silver, or chromium). The unique features of the dense system allow for direct study using spectroscopic techniques following the surface modification. Poisoning of the cathode from chromium contamination or catalytic enhancement from a LSGM phase for example, can be readily studied with this system. Additionally, this system is not limited to the study of cathodic reactions. A similar

system of a nickel and YSZ cermet is readily applicable to the stereological definition and electrochemical simulations presented here. Further insight into the reaction mechanisms can be garnered and a much more complete picture of SOFC kinetics will lead to better design of the electrodes and, ultimately, better performing fuel cell systems.

APPENDIX A

C++ Program for TPB/Percolation Simulation

The following section outlines the C++ program used to estimate the length of TPB in the various volume percentages of GDC/LSM composite electrodes. The program uses the overlapping spheres model to simulate the GDC phase enclosed in an LSM matrix material. Several tunable parameters were used including: the estimated number of particles, the volume percentage, the median particle size and standard deviation (to construct a log-normal distribution of particle radii), and the hard shell percentage of the particles (to determine the amount of impenetrable core of the particle; 0.0 for fully overlapping spheres and 1.0 for hard spheres). In addition to calculating the total TPB length, the program also gave estimates of the percolation percentage of the GDC phase and thereby allowing calculation of the amount of active TPB length. The following are the function headers for the program and a description of the purpose.

```
double random_setup()
```

This function initializes a random number generator utilizing the Mersenne Twister random number generator MT19937. This function returns a simulation ID number that can be used to rerun a simulation using the same generated sequence of random numbers. According the URL http://www.math.keio.ac.jp/~matumoto/emt.html the Mersenne Twister is ``designed with consideration of the flaws of various existing generators," has a period of $2^{19937}$ - 1, gives a sequence that is 623-dimensionally equidistributed, and ``has passed many stringent tests, including the die-hard test of G. Marsaglia and the load test of P. Hellekalek and S. Wegenkittl." It is efficient in memory

usage (typically using 2506 to 5012 bytes of static data, depending on data type sizes, and the code is quite short as well). It generates random numbers in batches of 624 at a time, so the caching and pipelining of modern systems is exploited. It is also divide- and mod-free.

This library is free software; you can redistribute it and/or modify it under the terms of the GNU Library General Public License as published by the Free Software Foundation (either version 2 of the License or, at your option, any later version). This library is distributed in the hope that it will be useful, but WITHOUT ANY WARRANTY, without even the implied warranty of MERCHANTABILITY or FITNESS FOR A PARTICULAR PURPOSE. See the GNU Library General Public License for more details. You should have received a copy of the GNU Library General Public License along with this library; if not, write to the Free Software Foundation, Inc., 59 Temple Place, Suite 330, Boston, MA 02111-1307, USA

```
bool check_space(vector<Particle>& particle_array, Particle &p, double
core)
```

This function accepts as its input the vector of particles used in the simulation, the position and radius the next particle to be placed in the simulation space and hard core percentage of the particles. The function then tests the position of the next particle to be placed against all existing particles for a hard core overlap. If some amount of overlap between the hard cores of the particle being placed and any other particle already in the simulation space exists, then that particle position is rejected and new one is chosen. If no overlap exists, a value of TRUE is return and the particle is placed at that position in the simulation space.

```
double init_positions(vector<Particle>& particle_array, int
num_particles, double mu, double sig, double volume_percentage, double
core)
```

This function sets the positions and radii for the initial set of particles in the simulation. The inputs to this function are the vector of particle, the initial number of user chosen particles, the mean particle radius, the standard deviation of the particle radii, the desired volume percentage and the hard core percentage. The function returns a value of L_0, the simulation space (cubic) size parameter.

The particle radii are first calculated to fit a log-normal distribution using the Box-Muller Method. Once the radii are all determined, L_0, is calculated from the total particle volume and the desired volume percentage. The particles are then randomly placed into the simulation space, first checking for hard core overlap using the `check_space()` function.

```
double total_volume_percentage(double l0, vector<Particle>&
particle_array)
```

This function calculates the particle volume percentage of the entire simulation space. The inputs to this function are the simulation space size parameter and the vector of particles. The function returns simulation space particle volume percentage. Calculation of the volume percentage is accomplished through a Monte Carlo simulation over the entire simulation space.

```
double particle_volume_percentage(Particle &p_volume, vector<Particle>&
particle_array)
```

This function calculates the occupied volume percentage of a spherical volume of simulation space where the next particle is to be placed. The inputs to this function are the to be placed particle's position and radius and vector or system particles. The function returns the occupied volume percentage of that spherical space. Calculation of the volume percentage is performed through a Monte Carlo simulation inside the spherical volume space of the to be placed particle.

```
double add_particles(vector<Particle>& particle_array, double l0,
double volume, double target_percent, double mu, double sig, double
core)
```

This function continuously adds more particles to the simulation space until the desired volume fraction is met. The inputs to this function are the vector of system particles, the system space size parameter, the particle volume percentage calculated using the `total_volume_percentage()` function, the target volume percentage, the average particle size and its standard deviation, and the hard core percentage. This function returns the new particle volume percentage for the simulation space.

This function is required because of the allowable overlap between the particles. It is not possible to know *a priori* the level of overlap between all the particles, thus, given simply the number of particles and their random placement, the target volume percentage will not be met. This function uses the volume percentage obtained from the `total_volume_percentage()` function as a starting point and then adds to that the unique volume obtained from randomly adding an additional particle. The unique volume is obtained through use of the `particle_volume_percentage()` function to first determine the percentage of the new particle's space that is already occupied, v_p, and then

adding to the total system particles' volume the volume of the new particle multiplied by $(1 - v_p)$. This process is repeated until the target volume is met to within approximately 0.001 percent.

```
void cluster_label(vector<Particle> particle_array, double l0, int
labels[particle_array.size()][2])
```

This function labels all particles in the simulation as being either on a boundary or in the bulk, assigns the particles to particular clusters and finally, labels which clusters percolate through the sample. The inputs to this function are the vector of particles, the simulation space size parameter, and an array of labels for each particle in the simulation. This function does not return a value. Particles are considered part of a percolating cluster if particles in opposite ends of that cluster reside in boundaries opposite of each other (i.e. for percolation in the z-direction, the cluster must contain at least one particle in both the top layer and the bottom layer of the sample space).

```
double calculateActiveTPB (vector<Particle> particle_array, double l0,
double zlevel, int labels[][2],double& perc_p)
```

This function calculates the amount of active TPB length in the simulation. As previously, a length of TPB is considered active if it belongs to a cluster of particles that percolate through the sample. The inputs to this function are the vector of particles, the simulation space size parameter, the plane at which the TPB measurements are taken, the array of labels for each particle in the simulation and the percentage of percolating particles. This function returns the length of active TPB per area of plane surface.

TPB length is calculated according the method laid out in CHAPTER 3 dealing with stereological calculations. This function simulates a real-life grinding and polishing method in that successive plane slices are used for the lineal intercept method.

```
double calculateTotalTPB (vector<Particle> particle_array, double l0, double zlevel)
```

This function calculates the amount of total TPB length in the simulation. This function behaves similarly to the `calculateActiveTPB()` function from above, but does not take percolation into account. The inputs to this function are the vector of particles, the simulation space size parameter and the plane at which the TPB measurements are taken.

APPENDIX B

Simulink Reaction Mechanism Diagrams

The following figures detail some of the Simulink models used during the simulation of the reaction mechanisms. These models are block diagram expressions for the differential algebraic equations that developed during solution of the proposed reaction mechanisms detailed in Equation (4.1). State-space parameters were garnered from solutions of these models and used to obtain the EIS spectra. This method was detailed in the text above.

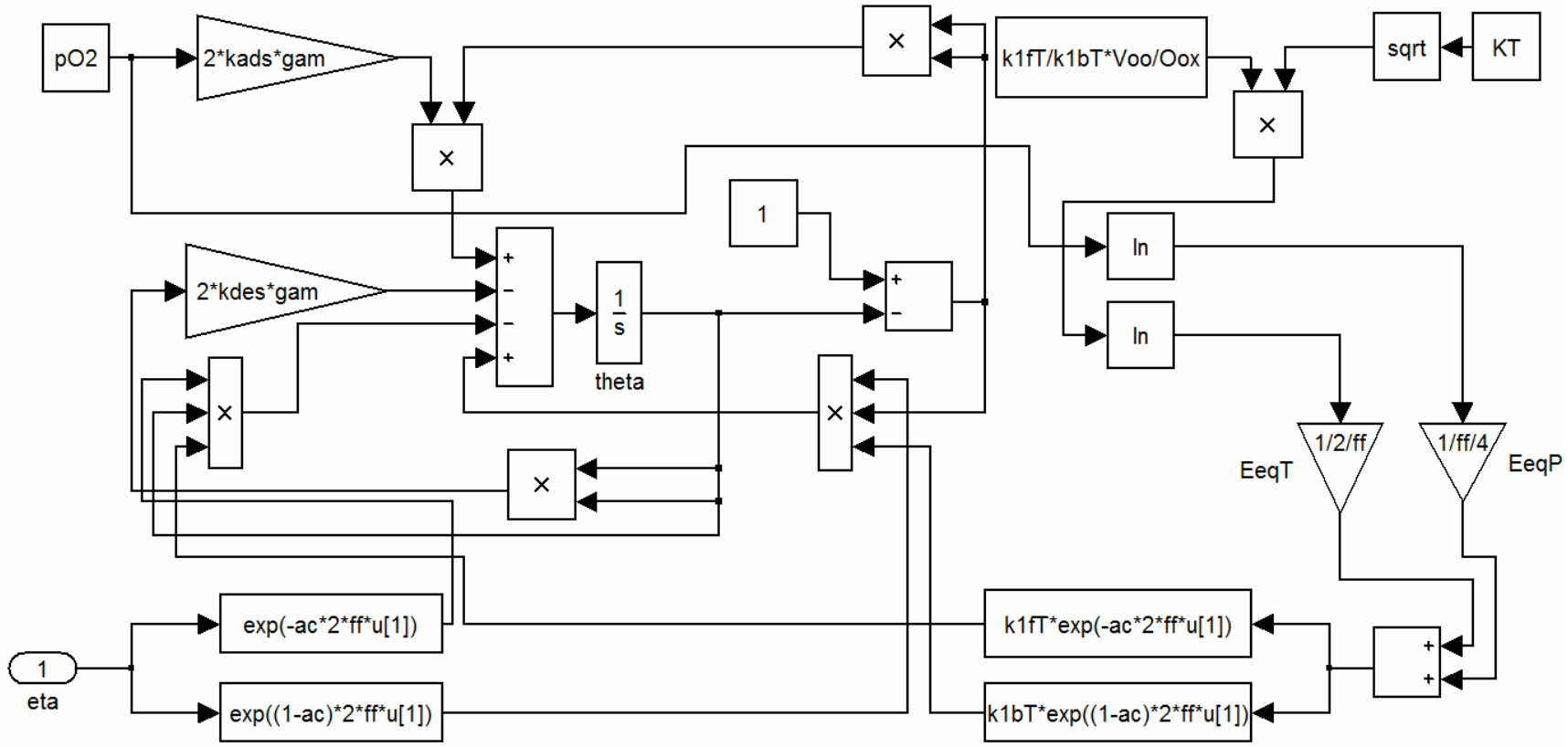

Figure B-1. Simulink block diagram for proposed oxygen reduction mechanism 1 (see Equation (4.1) for details)

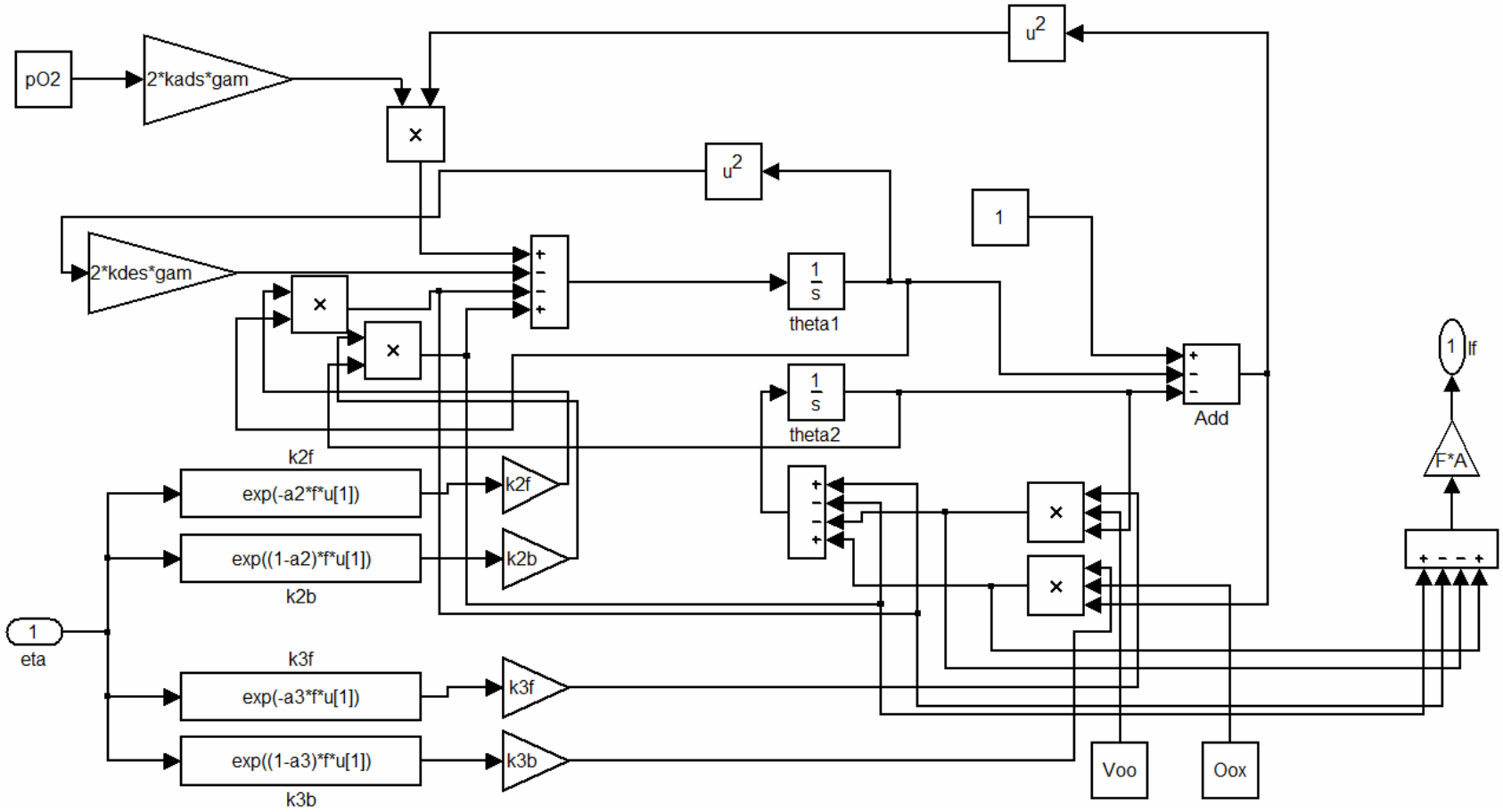

Figure B-2. Simulink block diagram for proposed oxygen reduction mechanism 2 (see Equation (4.1) for details)

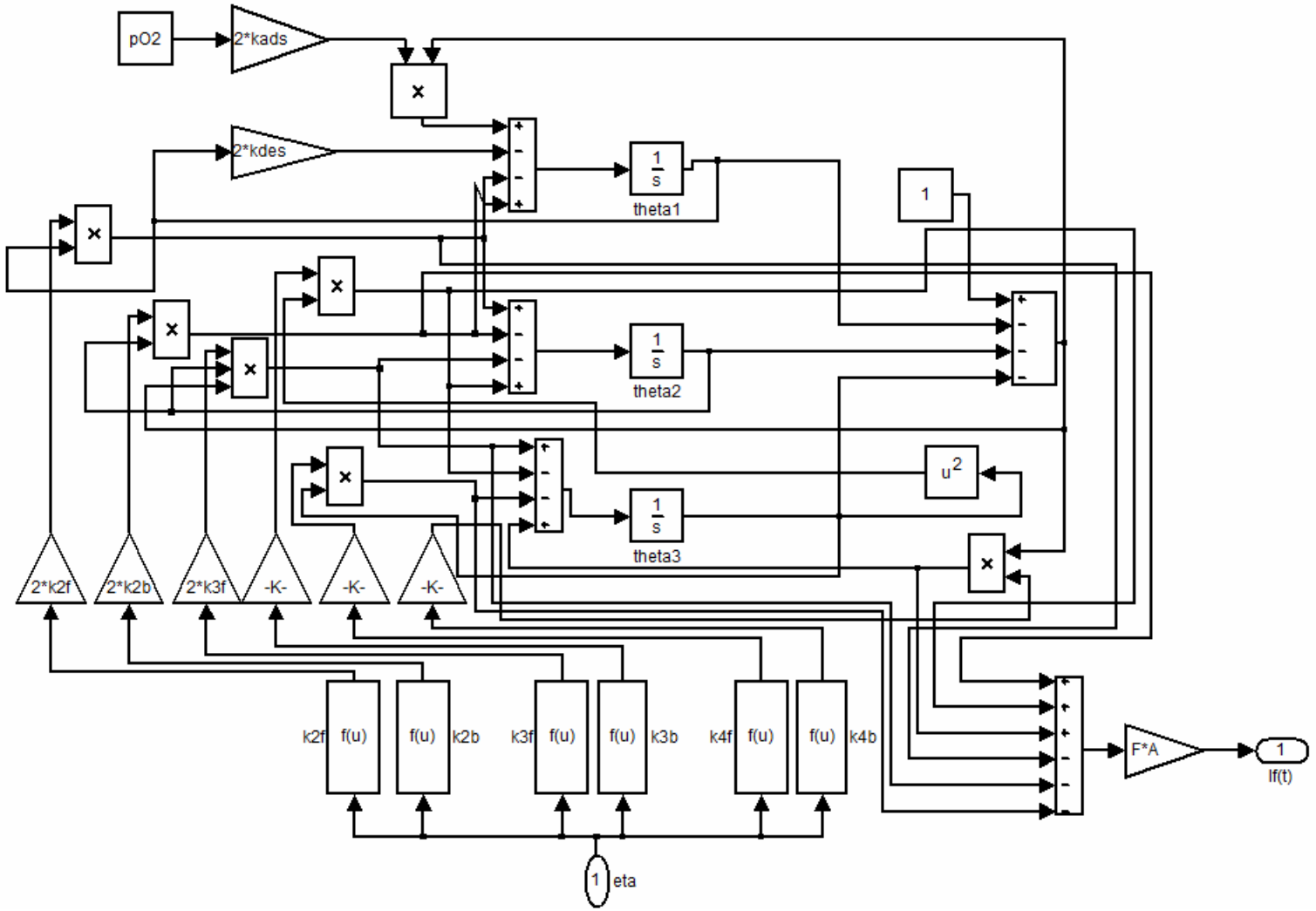

Figure B-3. Simulink block diagram for proposed oxygen reduction mechanism 3 (see Equation (4.1) for details)

REFERENCES

1. Eguchi, K., et al., *Electrical properties of ceria-based oxides and their application to solid oxide fuel cells.* Solid State Ionics, 1992. **52**(1-3): p. 165-172.

2. Endo, A., et al., *Cathodic reaction mechanism for dense Sr-doped lanthanum manganite electrodes.* Solid State Ionics, 1996. **86-88**: p. 1191-1195.

3. Hassel, B.A.v., B.A. Boukamp, and A.J. Burggraaf, *Electrode polarization at the Au, O_2(g)|yttria stabilized zirconia interface. Part I: Theoretical considerations of reaction model.* Solid State Ionics, 1991. **48**: p. 139 - 154.

4. Endo, A., et al., *Cathodic reaction mechanism for dense Sr-doped lanthanum manganite electrodes.* Solid State Ionics, 1996. **86-88**(Part 2): p. 1195.

5. Odgaard, M. and E. Skou, *SOFC cathode kinetics investigated by the use of cone shaped electrodes: The effect of polarization and mechanical load.* Solid State Ionics, 1996. **86-88**(Part 2): p. 1222.

6. Diard, J.P., B. Le Gorrec, and C. Montella, *Deviation of the polarization resistance due to non-linearity II. Application to electrochemical reactions.* Journal of Electroanalytical Chemistry, 1997. **432**(1-2): p. 41 - 52.

7. Manning, P.S., et al., *The kinetics of oxygen transport in 9.5 mol % single crystal yttria stabilised zirconia* Solid State Ionics, 1997. **100**(1-2): p. 10.

8. Adler, S.B., *Mechanism and kinetics of oxygen reduction on porous $La_{1-x}Sr_xCoO_{3-\delta}$ electrodes.* Solid State Ionics, 1998. **111**(1-2): p. 134.

9. Preis, W., E. Bucher, and W. Sitte, *Oxygen exchange kinetics of La0.4Sr0.6FeO3−δ by simultaneous application of conductivity relaxation and carrier gas coulometry.* Solid State Ionics, 2004. **175**(1-4): p. 397.

10. Bronin, D.I., et al., *Identification of the reaction mechanism of the Pt,O2/La(Sr)Ga(Mg)O3− electrode system.* Electrochimica Acta, 2004. **49**(15): p. 2435 - 2441.

11. Coffey, G.W., et al., *Electrochemical properties of lanthanum strontium aluminum ferrites for the oxygen reduction reaction.* Solid State Ionics, 2003. **158**(1-2): p. 1 - 9.

12. Chen, X.J., K.A. Khor, and S.H. Chan, *Identification of O_2 Reduction Processes at Yttria Stabilized Zirconia|doped Lanthanum Manganite Interface.* Journal of Power Sources, 2003. **123**: p. 17-25.

13. Lee, H.-K., *Electrochemical Characteristics of $La_{1-x}Sr_xMnO_3$ for Solid Oxide Fuel Cell.* Materials Chemistry and Physics, 2002. **77**: p. 639-646.

14. Jiang, S.P., *A Comparison of O_2 Reduction Reactions on Porous (La,Sr)MnO_3 and (La,Sr)(Co,Fe)O_3 Electrodes.* Solid State Ionics, 2002. **146**: p. 1-22.

15. Fleig, J., *On the width of the electrochemically active region in mixed conducting solid oxide fuel cell cathodes.* journal of Power Sources, 2002. **105**(2): p. 228 - 238.

16. Bieberle, A. and L.J. Gauckler, *State-space modeling of the anodic SOFC system Ni, H_2-H_2O|YSZ* Solid State Ionics, 2002. **146**(1-2): p. 41.

17. Ringuede, A. and J. Fouletier, *Oxygen reaction on strontium-doped lanthanum cobaltite dense electrodes at intermediate temperatures.* Solid State Ionics, 2001. **139**(3-4): p. 167 - 177.

18. Kek, D. and N. Bonanos, *Investigation of hydrogen oxidation reaction on a metal/perovskite proton conductor interface by impedance spectroscopy.* Vacuum, 2001. **61**(2-4): p. 457.

19. Steele, B.C.H., K.M. Hori, and S. Uchino, *Kinetic parameters influencing the performance of IT-SOFC composite electrodes* Solid State Ionics, 2000. **135**(1-4): p. 450.

20. Lane, J.A. and J.A. Kilner, *Oxygen surface exchange on gadolinia doped ceria.* Solid State Ionics, 2000. **136-137**: p. 932.

21. Horita, T., et al., *Oxygen reduction sites and diffusion paths at $La_{0.9}Sr_{0.1}MnO_{3-x}$/yttria-stabilized zirconia interface for different cathodic overvoltages by secondary-ion mass spectrometry.* Solid State Ionics, 2000. **127**(1-2): p. 55 - 65.

22. Hermann, V., et al., *Mechanistic studies of oxygen reduction at $La_{0.6}Ca_{0.4}CoO_3$-activated carbon electrodes in a channel flow cell* Electrochimica Acta, 2000. **46**(2-3): p. 372.

23. Athanasiou, C., et al., *Electrode polarization at the O2(g), Pd/YSZ interface.* Solid State Ionics, 2000. **136-137**: p. 873 - 877.

24. Mori, M., et al., *Reaction mechanism between lanthanum manganite and yttria doped cubic zirconia.* Solid State Ionics, 1999. **123**(1-4): p. 119.

25. Mitterdorfer, A. and L.J. Gauckler, *Identification of the reaction mechanism of the Pt, O2(g)|yttria-stabilized zirconia system: Part II: Model implementation, parameter estimation, and validation.* 1999. **117**(3-4): p. 203 - 217.

26. Mitterdorfer, A. and L.J. Gauckler, *Identification of the reaction mechanism of the Pt, O_2(g)|yttria-stabilized zirconia system Part I: General framework, modelling, and structural investigation.* Solid State Ionics, 1999. **117**: p. 187-202.

27. Mitterdorfer, A. and L.J. Gauckler, *Reaction kinetics of the Pt, O_2(g)|c-ZrO_2 system: precursor-mediated adsorption* Solid State Ionics, 1999. **120**(1-4): p. 225.

28. Jiang, Y., et al., *Electrochemical Reduction of Oxygen on a Strontium Doped Lanthanum Manganite Electrode.* Solid State Ionics, 1998. **110**: p. 111-119.

29. Xia, C. and M. Liu, *Low-temperature SOFCs based on $Gd_{0.1}Ce_{0.9}O_{1.95}$ fabricated by dry pressing.* Solid State Ionics, 2001. **144**(3-4): p. 249-255.

30. Adler, S.B., *Limitations of charge-transfer models for mixed-conducting oxygen electrodes.* Solid State Ionics, 2000. **135**(1-4): p. 603-612.

31. Brichzin, V., et al., *The Geometry Dependence of the Polarization Resistance of Sr-doped $LaMnO_3$ Microelectrodes on Yttria-stablized Zirconia.* Solid State Ionics, 2002. **152**: p. 499-507.

32. Deseure, J., et al., *Modelling of dc and ac responses of a planar mixed conducting oxygen electrode* Solid State Ionics, 2005. **176**(3-4): p. 244.

33. Deseure, J., et al., *Theoretical optimisation of a SOFC composite cathode.* Electrochimica Acta, 2005. **In Press, Corrected Proof**.

34. Heuveln, F.H.v. and H.J.M. Bouwmeester, *Electrode properties of Sr-doped $LaMnO_3$ on Yttria-stablized zirconia II. Electrode kinetics.* Journal of The Electrochemical Society, 1997. **144**(1): p. 134 - 140.

35. Scott, K. and P. Argyropoulos, *A current distribution model of a porous fuel cell electrode.* Journal of Electroanalytical Chemistry, 2004. **567**(1): p. 103-109.

36. Steele, B.C.H., *Interfacial reactions associated with ceramic ion transport membranes.* Solid State Ionics, 1995. **75**: p. 165.

37. Virkar, A.V., et al., *The role of electrode microstructure on activation and concentration polarizations in solid oxide fuel cells.* Solid State Ionics, 2000. **131**(1-2): p. 189-198.

38. Zeng, Y., C. Tian, and L. Bao, *A modeling investigation on the electrochemical behavior of porous mixed conducting cathodes for solid oxide fuel cells.* Journal of Power Sources, 2005. **139**(1-2): p. 43.

39. Chen, X.J., K.A. Khor, and S.H. Chan, *Electrochemical Behavior of La(Sr)MnO_3 Electrode Under Cathodic and Anodic Polarization.* Solid State Ionics, 2004. **167**: p. 379-387.

40. Diethelm, S., et al., *Study of oxygen exchange and transport in mixed conducting cobaltates by electrochemical impedance spectroscopy.* Solid State Ionics, 2000. **135**(1-4): p. 618.

41. Aaberg, R.J., R. Tunold, and R. Odegard, *On the electrochemistry of metal–YSZ single contact electrodes.* Solid State Ionics, 2000. **136-137**: p. 707 - 712.

42. Matsuzaki, Y. and I. Yasuda, *Relationship between the steady-state polarization of the SOFC air electrode, $La_{0.6}Sr_{0.4}MnO_{3+\delta}$/YSZ, and its complex impedance measured at the equilibrium potential.* Solid State Ionics, 1999. **126**(3-4): p. 307 - 313.

43. Liu, M. and J. Winnick, *Fundamental Issues in Modeling of Mixed Ionic-Electronic Conductors (MIECs).* Solid State Ionics, 1999. **118**: p. 11-21.

44. Jorgensen, M.J., S. Primdahl, and M. Mogensen, *Characterization of Composite SOFC Cathodes Using Electrochemical Impedance Spectroscopy.* Electrochimica Acta, 1999. **44**: p. 4195-4201.

45. Closset, A., et al., *Study of oxygen exchange and transport in mixed conducting electroceramics.* Journal of European Ceramic Society, 1999. **19**(6-7): p. 846.

46. Mitterdorfer, A. and L.J. Gauckler, *$La_2Zr_2O_7$ Formation and Oxygen Reduction Kinetics of the $La_{0.85}Sr_{0.15}Mn_yO_3$, $O_2(g)|$YSZ System.* Solid State Ionics, 1998. **111**: p. 185-218.

47. Liu, M. and Z. Wu, *Significance of Interfaces in Solid-State Cells With Porous Electrodes of Mixed Ionic-Electronic Conductors.* Solid State Ionics, 1998. **107**: p. 105-110.

48. Hsiao, Y.C. and J.R. Selman, *The degradation of SOFC electrodes.* Solid State Ionics, 1997. **98**: p. 33-38.

49. Mogensen, M. and S. Skaarup, *Kinetic and geometric aspects of solid oxide fuel cell electrodes.* Solid State Ionics, 1996. **86-88**(Part 2): p. 1160.

50. Herle, J.V., A.J. McEvoy, and K.R. Thampi, *A Study on the $La_{1-x}Sr_xMnO_3$ Oxygen Cathode.* Electrochimica Acta, 1996. **41**(9): p. 1447-1454.

51. Minh, N.Q. and T. Takahashi, *Science and Technology of Ceramic Fuel Cells*. 1995, Amsterdam, Netherlands: Elsevier Science B.V. 366.

52. Subbarao, E.C. and H.S. Maiti, *Solid electrolytes with oxygen ion conduction.* Solid State Ionics, 1984. **11**(4): p. 317-338.

53. Co, A.C., S.J. Xia, and V.I. Birss, *A kinetic study of the oxygen reduction reaction at LaSrMnO3-YSZ composite electrodes.* Journal of the Electrochemical Society, 2005. **152**(3): p. A570-A576.

54. Kudo, T. and H. Obayashi, *Oxygen Ion Conduction of the Fluorite-Type $Ce_{1-x}Ln_xO_{2-x/2}$ (Ln = Lanthanoid Element).* Journal of The Electrochemical Society, 1975. **122**(1): p. 142-147.

55. Yahiro, H., K. Eguchi, and H. Arai, *Electrical properties and reducibilities of ceria-rare earth oxide systems and their application to solid oxide fuel cell.* Solid State Ionics, 1989. **36**(1-2): p. 71-75.

56. Koep, E., et al., *Characteristic thickness for a dense $La_{0.8}Sr_{0.2}MnO_3$ electrode.* Electrochemical and Solid State Letters, 2005. **8**(11): p. A592-A595.

57. Mizusaki, J., et al., *Nonstoichiometry and thermochemical stability of the perovskite-type $La_{1-x}Sr_xMnO_{3-\delta}$.* Solid State Ionics, 1991. **49**: p. 111-118.

58. Compson, C. and M.L. Liu, *Fabrication and characterization of hermetic solid oxide fuel cells without sealant.* Solid State Ionics, 2006. **177**(3-4): p. 367-375.

59. Macdonald, J.R., *Impedance Spectroscopy: Emphasizing solid materials and systems*. 1987, New York: John Wiley & Sons. 346.

60. Anh, V.V., et al., *A reactive state-space model for prediction of urban air pollution.* Environmental Modelling and Software, 1998. **13**(3-4): p. 239 - 246.

61. Hinrichsen, D. and A.J. Pritchard, *Mathematical Systems Theory I: Modelling, State Space Analysis, Stability and Robustness*. 2005, New York: Springer.

62. Nise, N.S., *Control Systems Engineering*. 4th ed. 2004, Hoboken, NJ: John Wiley & Sons, Inc.

63. Bard, A.J. and L.R. Faulkner, *Electrochemical Methods: Fundamentals and Applictions*. 2000: John Wiley & Sons. 856.

64. Brockris, J.O. and A.K.N. Reddy, *Modern Electrochemistry*. Vol. 2. 1970, London: Plenum Press.

65. Chan, S.H., K.A. Khor, and Z.T. Xia, *A Complete Polarization Model of a Solid Oxide Fuel Cell and Its Sensitivity to the Change of Cell Component Thickness.* Journal of Power Sources, 2001. **93**: p. 130-140.

66. Tanner, C.W., K.Z. Fung, and A.V. Virkar, *The effect of porous composite electrode structure on solid oxide fuel cell performance .1. Theoretical analysis.* Journal of the Electrochemical Society, 1997. **144**(1): p. 21-30.

67. Kim, J.-W., et al., *Polarization Effects in Intermediate Temperature, Anode-Supported Solid Oxide Fuel Cells.* Journal of The Electrochemical Society, 1999. **146**(1): p. 69-78.

68. Newman, J.S. and C.W. Tobias, *THEORETICAL ANALYSIS OF CURRENT DISTRIBUTION IN POROUS ELECTRODES.* Journal of the Electrochemical Society, 1962. **109**(12): p. 1183-1191.

69. Geankoplis, C.J., *Mass Transport Phenomena*. 1972, New York: Holt, Reinhart and Winston.

70. Cussler, E.L., *Diffusion: Mass Transfer in Fluid Systems*. 1995, Cambridge: Cambridge University Press.

71. Hines, A. and R.N. Maddox, *Mass Transfer: Fundamentals and Applications*. 1985, New Jersey: Prentice Hall.

72. Mason, E.A. and A.P. Malinauskas, *Gas Transport in Porous Media: The Dusty Gas Model*. 1983, Amsterdam: Elsevier.

73. Chen, X.J., K.A. Khor, and S.H. Chan, *Electrochemical behavior of La(Sr)MnO3 electrode under cathodic and anodic polarization.* Solid State Ionics, 2004. **167**(3-4): p. 379-387.

74. Athanasiou, C., et al., *Electrode polarization at the O2(g), Pd/YSZ interface.* Solid State Ionics, 2000. **136-137**: p. 873-877.

75. Stojanovic, M., et al., *Reaction Kinetics of Methane Oxidation over $LaCr_{1-x}Ni_xO_3$ Perovskite Catalysts.* Journal of Catalysis, 1997. **166**(2): p. 332.

76. van Hassel, B.A., B.A. Boukamp, and A.J. Burggraaf, *Electrode polarization at the Au, O2(g)/yttria stabilized zirconia interface. Part I: Theoretical considerations of reaction model.* Solid State Ionics, 1991. **48**(1-2): p. 139-154.

77. Anh, V.V., et al., *A reactive state-space model for prediction of urban air pollution.* Environmental Modelling & Software, 1998. **13**(3-4): p. 239-246.

78. Koep, E., et al., *A photolithographic process for investigation of electrode reaction sites in solid oxide fuel cells.* Solid State Ionics, 2005. **176**(1-2): p. 1-8.

79. Martin, C.R. and I.A. Aksay, *Submicrometer-scale patterning of ceramic thin films.* Journal of Electroceramics, 2004. **12**(1-2): p. 53-68.

80. van Roosmalen, J.A.M. and E.H.P. Cordfunke, *Chemical reactivity and interdiffusion of (La, Sr)MnO3 and (Zr, Y)O2, solid oxide fuel cell cathode and electrolyte materials.* Solid State Ionics, 1992. **52**(4): p. 303-312.

81. Underwood, E.E., *Quantitative Stereology*. Metallurgy and Materials, ed. M. Cohen. 1981: Addison-Wesley Publishing Company, Inc. 274.

82. Box, G.E.P. and M.E. Muller, *A Note on the Generation of Random Normal Deviates.* Annals of Mathematical Statistics, 1958. **29**(2): p. 610-611.

83. Babalievski, F., *Cluster counting: The Hoshen-Kopelman algorithm versus spanning tree approaches.* International Journal of Modern Physics C, 1998. **9**(1): p. 43-60.

84. Stoll, E., *A fast cluster counting algorithm for percolation on and off lattices.* Computer Physics Communications, 1998. **109**(1): p. 1-5.

85. Hoshen, J. and R. Kopelman, *Percolation and cluster distribution. I. Cluster multiple labeling technique and critical concentration algorithm* Physical Review B, 1976. **14**(8): p. 3438-3445.

86. Pike, G.E. and C.H. Seager, *Percolation and conductivity: A computer study. I.* Physical Review B, 1974. **10**(4): p. 1421.

87. Seager, C.H. and G.E. Pike, *Percolation and conductivity: A computer study. II.* Physical Review B, 1974. **10**(4): p. 1435.

88. Divisek, J., et al., *The Kinetics of Electrochemical Reactions on High Temperature Fuel Cell Electrodes.* Journal of Power Sources, 1994. **49**: p. 257-270.

89. Jorgensen, M.J., S. Primdahl, and M. Mogensen, *Characterisation of composite SOFC cathodes using electrochemical impedance spectroscopy.* Electrochimica Acta, 1999. **44**(24): p. 4195-4201.

90. Berthier, F., J.P. Diard, and R. Michel, *Distinguishability of equivalent circuits containing CPEs: Part I. Theoretical part.* Journal of Electroanalytical Chemistry, 2001. **510**(1-2): p. 1-11.

91. Berthier, F., et al., *Method For Determining The Faradaic Impedance Of An Electrode-Reaction - Application To Metal Corrosion Rate Measurements.* Corrosion, 1995. **51**(2): p. 105-115.

92. Verkerk, M.J., M.W.J. Hammink, and A.J. Burggraaf, *Oxygen transfer on substituted ZrO_2, Bi_2O_3, and CeO_2 electrolytes with platinum electrodes: I. Electrode resistance by DC polarization.* Journal of the Electrochemical Society, 1983. **130**: p. 70 - 78.

93. Wang, D.Y. and A.S. Nowick, *Cathodic and anodic polarization phenomena at platinum electrodes with doped CeO_2 as electrolyte: I. Steady-state overpotential.* Journal of the Electrochemical Society, 1979. **126**: p. 1155 - 1165.

94. Kjaer, J., I.G. Krogh Andersen, and E. Skou, *Thermogravimetric studies of oxygen stoichiometry and oxygen transport kinetics in lanthanum strontium ferrite manganites.* Solid State Ionics, 1998. **113-115**: p. 392.

95. Yasuda, I., et al., *Oxygen tracer diffusion coefficient of (La, Sr)$MnO_{3\pm\delta}$.* Solid State Ionics, 1996. **86-88**(Part 2): p. 1201.

96. Lu, X., P.W. Faguy, and M. Liu, *In Situ Potential-Dependent FTIR Emission Spectroscopy. A Novel Probe for High Temperature Fuel Cell Interfaces.* Journal of The Electrochemical Society, 2002. **149**(10): p. 1293-1297.

97. Winnubst, A.J.A., A.H.A. Scharenborg, and A.J. Burggraaf, *The electrode resistance of ZrO2---Y2O3(-Bi2O3) solid electrolytes with Pt electrodes.* Solid State Ionics, 1984. **14**(4): p. 319-327.

98. Jiang, Y., et al., *Electrochemical reduction of oxygen on a strontium doped lanthanum manganite electrode.* Solid State Ionics, 1998. **110**(1-2): p. 111-119.

99. Berthier, F., et al., *Steady-State Investigation And Electrochemical Impedance Spectroscopy - Identifiability And Distinguishability Of Metal Dissolution And Passivation Mechanisms.* Journal of Electroanalytical Chemistry, 1993. **362**(1-2): p. 13-20.

100. Hanselman, D.C. and B. Littlefield, *Mastering MATLAB 6, A Comprehensive Tutorial and Reference*. 2000: Prentice-Hall. 832.

101. Dabney, J.B. and T.L. Harman, *Mastering Simulink*. 2004, Upper Saddle River, NJ: Pearson Prentice Hall. 376.

102. Heuveln, F.H.v. and H.J.M. Bouwmeester, *Electrode properties of Sr-doped $LaMnO_3$ on Yttria-stablized zirconia.* Journal of The Electrochemical Society, 1997. **144**(1): p. 134 - 140.

103. Huijsmans, J.P.P., *Ceramics in solid oxide fuel cells.* Current Opinion in Solid State & Materials Science, 2001. **5**(4): p. 317-323.

104. Katsuki, M., et al., *The oxygen transport in Gd-doped ceria.* Solid State Ionics, 2002. **154-155**: p. 595.

105. Gorte, R. and L.D. Schmidt, *Desorption kinetics with precursor intermediates.* Surface Science, 1978. **76**: p. 559-573.

106. Gland, J.L., *Molecular and atomic adsorption of oxygen on the Pt(111) and Pt(S)-12(111)x(111) surfaces.* Surface Science, 1980. **93**: p. 487-514.

107. Gland, J.L., B.A. Sexton, and G.B. Fisher, *Oxygen interactions with the Pt(111) surface.* Surface Science, 1980. **95**: p. 587-602.